Coherent Structures in Taylor-Couette Flow

-Experimental Investigation-

Proefschrift

ter verkrijging van de graad van doctor
aan de Technische Universiteit Delft,
op gezag van de Rector Magnificus prof. ir. K.C.A.M. Luyben,
voorzitter van het College voor Promoties,
in het openbaar te verdedigen op dinsdag 14 oktober 2014 om 12:30 uur

door

Sedat TOKGÖZ
ingenieur luchtvaart- en ruimtevaart techniek
Istanbul Technical University, Turkije
geboren te Tekirdağ, Turkije

Dit proefschrift is goedgekeurd door de promotor:
Prof. dr. ir. J. Westerweel
Copromotor: Dr. G. E. Elsinga

Samenstelling promotiecommissie:

Rector Magnificus,	voorzitter
Prof. dr. ir. J. Westerweel,	Technische Universiteit Delft, promotor
Dr. ir. G. E. Elsinga,	Technische Universiteit Delft, copromotor
Prof. dr. H. Alfredsson,	Royal Institute of Technology,
Prof. dr. ir. B. E. Eckhardt,	Technische Universiteit Delft,
Prof. dr. H. J. H. Clercx,	Technische Universiteit Eindhoven,
Prof. dr. F. Scarano,	Technische Universiteit Delft,
B. Wieneke, M.Sc.	LaVision, Göttingen

The work in this thesis was carried out at the Aero & Hydrodynamics Laboratory of the faculty of Mechanical, Maritime and Materials Engineering of the Delft University of Technology. It was partly financed within EU Marie Curie FP7 "Surface Physics for Advanced Manufacturing" (ITN 215723) project. The project was co-financed by LaVision GmbH, Germany and ASML, the Netherlands.

Cover design: Ümit Bal
Copyright © 2014 by S. Tokgöz
All rights reserved
ISBN 9789461087683

Printed by Gildeprint V.V., Enschede

Contents

Summary

Coherent Structures in Taylor-Couette Flow: Experimental Investigation –Sedat Tokgöz–

Taylor-Couette flow is defined as the flow confined between two coaxial cylinders which can rotate independently. Several different flow states can be observed in the gap between the cylinders by changing the rotation speeds and the rotating directions of the cylinders. As it is a closed environment, the input and the output of the system can be monitored easily, thus the Taylor-Couette flow becomes quite useful for turbulence studies.

The aim of this thesis is to investigate the previously reported change of torque values with the rotation speeds of the cylinders and to study its relation to coherent turbulent flow structures. The flow structures are investigated using tomographic PIV, which is a fully volumetric measurement method that resolves all three velocity components. Different flow states, and their contribution to the Reynolds stresses are revealed. Initially the validation of the implementation of tomographic PIV was done using the analytically well-defined laminar Taylor-Couette flow at a shear Reynolds number $Re_S = 615$. The results showed that the measured velocities deviate from the analytical solution by not more than 3.2%.

Measurements of turbulent flows should ideally have a resolution of the order of the Kolmogorov microscale to resolve the smallest scales in turbulence. However, as the number of reconstructed particle images is typically less than the number of velocity vectors, the actual spatial resolution of tomographic PIV is not well defined. Furthermore, the required resolution to resolve smallest scales in turbulence is not known exactly. Therefore, the Taylor-Couette setup was also used to investigate the spatial resolution of tomographic PIV, by exploiting the fact that the power input to the system, as determined from the torque measurements and the cylinder rotation speed, is balanced by the viscous dissipation rate,

which can be computed using the measured velocities. The comparison reveals that the dissipation rate was underestimated by tomographic PIV for all turbulent cases studied in this thesis ($3800 \leq Re_S \leq 47000$). Application of a large eddy turbulence model to the PIV data showed that the error in the direct estimation of the dissipation rate by tomographic PIV can be ascribed to unresolved scales. It was found that the actual spatial resolution of tomographic PIV is dependent on both the interrogation volume overlap, and the interrogation volume size (D_I). Increasing the interrogation overlap at a constant D_I decreases the error and results in better spatial resolution (although it might result in higher data density that possibly exceeds the tracer particle density). On the other hand it was found that the distance between two neighboring vectors (i.e. vector spacing δ_x, which depends on both overlap and D_I) is a more suitable parameter to quantify the actual spatial resolution of tomographic PIV (and PIV in general), rather than the interrogation volume size. This seems to apply at least up to 75% overlap. The minimum required vector spacing to resolve small-scale motions in the flow was found as $1.5-2.0$ times the Kolmogorov length scale (corresponding to interrogation volume size of $6.0-8.0$ times Kolmogorov length scale at 75% overlap). Therefore interrogation volumes that are bigger than the values suggested in the literature might be used instead, as these were based on 50% overlap.

Next, time-resolved tomographic PIV measurements were performed at fully turbulent flow to demonstrate the capability of the measurement system and the flow geometry to study dynamic events in turbulence. Turbulent flow with an approximately zero mean velocity was created by rotating the cylinders in opposite directions with the same wall velocities. Using this idea, the observation times of the flow structures could be increased by an order of magnitude as compared to similar studies in turbulent boundary layers. Examples of observed events, such as azimuthal velocity bursts, stretching and breaking-up of vortical structures, are presented.

In the literature it was reported that at a constant shear Reynolds number (Re_S), the measured torque values change depending on the rotation number (R_Ω). In Chapter 5 of this thesis, the connection between turbulent flow structures and the change of the torque was made by using tomographic PIV. It was shown that the large-scale turbulent flow structures change significantly with R_Ω in both the mean and

the instantaneous flows, which explains the change in the torque. In order to compute the contribution of the large and the smaller-scale structures to the torque, the instantaneous flow was decomposed into the large and the smaller-scale motions by filtering. It was shown that at a constant turbulent Reynolds number, the instantaneous large-scale structures change their orientation from the azimuthal direction (at only inner cylinder rotation), to blobs (at exact counter rotation), and finally to Taylor-column-like structures elongated in the axial direction (at only outer cylinder rotation). The Reynolds stresses associated with these structures indicate that this orientational change may be the mechanism responsible for the reported change of the torque scaling. Close to only inner cylinder rotation the mean flow contribute significantly to the angular momentum transport, and it is ineffective elsewhere. The large-scale turbulent structures are not effective on the angular momentum transport in cases close to only inner and only outer cylinder rotation. However, close to exact counter rotation, inclined large-scale structures induce azimuthal and radial velocities simultaneously, which results in higher Reynolds shear stress, hence torque. The smaller-scales were found only to be significant for the cases close to only outer cylinder rotation.

Samenvatting

Coherente structuren in Taylor-Couette stroming: Experimenteel Onderzoek –Sedat Tokgöz–

Taylor-Couette stroming kan omschreven worden als de stroming tussen twee coaxiale cylinders die onafhankelijk van elkaar kunnen roteren. Door de rotatiesnelheid en de draairichting van de cylinders te veranderen, worden verschillende stromingstoestanden waargenomen tussen de twee cylinders. Aangezien dit een gesloten systeem betreft, kunnen de input en output van het systeem gemakkelijk gemonitoord worden, waardoor de Taylor-Couette zeer bruikbaar wordt voor turbulentie studies.

Het doel van dit proefschrift is het onderzoeken en bestuderen van de relatie tussen eerder gerapporteerd verandering in koppel met de rotatiesnelheden van de cylinders ende coherente turbulente stromingsstructuren. De stromingsstructuren worden onderzocht door middel van tomografische PIV, wat een volledig volumetrische meetmethode is die de drie snelheidscomponenten geeft. De verschillende stromingstoestanden en hun bijdrage aan de Reynolds spanningen worden onthuld. De validatie van het gebruik van tomografische PIV is gedaan met een goed analytisch gedefinieerde laminaire stroming bij een afschuif Reynolds getal van $Re_S = 615$. De resultaten tonen aan dat de gemeten snelheden niet meer dan 3.2% afwijken van de analytische oplossing.

Metingen van turbulente stromingen moeten idealiter een resolutie hebben van de orde van de Kolmogorov microschaal, om de kleinste schaal van turbulentie te kunnen oplossen. Aangezien het aantal gereconstrueerde deeltjes typisch minder is dan het aantal snelheidsvectoren, is de ruimtelijke resolutie van tomografische PIV niet goed gedefinieerd. Bovendien is de gewenste resolutie om de kleinste schalen op te lossen niet exact bekend. De Taylor-Couette opstelling is daarom gebruikt om de ruimtelijke resolutie van tomografische PIV te onderzoeken door gebruik te maken van het feit dat het vermogen van het sys-

teem, dat is bepaald aan de hand van de koppel metingen en de rotatiesnelheden, in balans is met het viskeuze disspatievermogen dat berekend wordt uit de gemeten snelheden. Uit de vergelijking blijkt dat het dissipatievermogen werd onderschat door tomografische PIV voor alle turbulente gevallen bestudeerd in dit proefschrift ($3800 \leq Re_S \leq 47000$). Uit de toepassing van een LES model op de PIV data bleek dat de fout in de directe schatting van het dissipatievermogen door tomografische PIV, kan worden toegeschreven aan onopgeloste schalen. Gevonden werd dat de werkelijke ruimtelijke resolutie van tomografische PIV afhankelijk is van zowel de interrogatie volume overlap, als van de interrogatie volumegrootte (D_I). Het verhogen van interrogatie overlap met een constante D_I verkleint de fout en resulteert in een betere ruimtelijke resolutie (hoewel het zou kunnen leiden tot een hogere data dichtheid die mogelijk hoger is dan de tracer deeltje dichtheid). Daarentegen bleek de afstand tussen twee naburige vectoren (oftewel vector afstand δ_x, die afhangt van zowel overlap als D_I) beter geschikt is als ruimtelijke parameter om de werkelijke ruimtelijke resolutie van tomografische PIV te kwantificeren (en PIV in het algemeen), in plaats van de interrogatie volumegrootte. Dit geldt in eider geval tot 75% overlap. De minimaal vereiste vector afstand om de kleinschalige bewegingen in de stroming op te lossen is $1.5 - 2.0$ keer de Kolmogorov lengte schaal (overeenkomend met een volume grootte van $6.0 - 8.0$ keer de Kolmogorov lengte schaal bij 75% overlap). Daarom kunnen interrogatie volumes die groter zijn dan de waarden die worden aangegeven in literatuur worden gebruikt, aangezien die gebaseerd zijn op 50% overlap.

Vervolgens zijn tijd opgeloste tomografische PIV metingen uitgevoerd van volledig turbulente stromingen om de mogelijkheden van het meetsysteem en stromingsgeometrie te demonstreren voor de studie van dynamische gebeurtenissen in turbulentie. Turbulente stroming met een gemiddelde snelheid van nul zijn verkregen door de cylinders met een gelijke snelheid in tegengestelde richting te laten draaien. Met dit principe kan de waarnemingstijd van de stromingsstructuren verlengd worden met een orde van grootte, vergeleken met soortgelijke turbulente grenslaag studies. Voorbeelden van waargenomen gebeurtenissen, zoals azimutale snelheid uitbarstingen, oprekken en opbreken van vortex structuren worden beschreven.

In de literatuur wordt gemeld dat bij een constante afschuif Reynolds getal (Re_S) de gemeten koppel waarden veranderen, afhankelijk van het

rotatie getal (R_Ω). In hoofdstuk 5 van dit proefschrift wordt een verband tussen de turbulente stromingsstructuren en de verandering van het koppel gelegd met behulp van tomografische PIV. Er wordt bewezen dat de grootschalige turbulente stromingsstructuren aanzienlijk veranderen met R_Ω, zowel in de gemiddelde als in de momentane stromingen, wat de verandering in koppel verklaart. Om de bijdrage van de groot- en kleinschalige structuren op de koppel te berekenen, werd de momentane stroming ontbonden in groot- en kleinschalige bewegingen. Er wordt bij een constante turbulente Reynolds getal aangetoond dat de momentane grootschalige structuren hun richting veranderen van de azimutale richting (bij binnen cylinder rotatie) naar blobs (bij exacte tegen-rotatie), en Taylor-kolomvormige structuren in de axiale richting (bij buiten cylinder rotatie). De Reynolds spanningen die gekoppeld zijn aan deze structuren, tonen aan dat de oriëntatie wijziging het mechanisme kan zijn die verantwoordelijk is voor de gerapporteerde verandering van het koppel. Rond het punt van alleen binnen cylinder rotatie draagt de gemiddelde stroming significant bij aan het impulsmoment transport, en zij is elders niet effectief. De grootschalige turbulente structuren zijn niet effectief op het impulsmoment transport bij alleen binnen en alleen buiten cylinder rotatie. Echter, dichtbij exacte tegen-rotatie induceren de hellende grootschalige structuren tegelijkertijd de azimutale en radiale snelheden, wat resulteert in een hogere Reynolds schuifspanning, en dus koppel. De kleinschalige structuren bleken alleen significant te zijn voor de gevallen dichtbij alleen buiten cylinder rotatie.

1 Introduction

1.1 Taylor-Couette Flow as a Model for Rotating Flow

Rotating flows occur in many technical systems and in nature, such as bearings, turbo machinery, and atmospheric flows [19, 47]. Examples of idealized models of rotating flows are rotating disk flow and the flow around rotating cylinders and spheres. A sub-class of rotating flows is the flow between two infinitely long and independently rotating cylinders, named as Taylor-Couette flow. In practice, the cylinders have a finite length, and therefore Taylor-Couette facilities are approximations of ideal Taylor-Couette flow. Isaac Newton is believed to be one of the first scientists attracted to the flow between these rotating cylinders [34]. However, the detailed investigation of this flow has only increased after the pioneering study of Taylor [101]. This is mostly due to the advantage of the Taylor-Couette configuration, where it is possible to examine the flow stability in a small closed environment that can be manipulated simply by adjusting the rotation speeds of the cylinders. Nowadays studies involving the flow between two cylinders extend to different applications like filtration [113], sports applications [48] and to accretion disks around stars [77].

As it is known from turbulence theory, energy is initially transferred from the mean flow into large-scale eddies with a typical size comparable to the flow geometry, referred to as the integral length scale. Then, the energy is transferred to smaller and smaller scales [79,103], until the energy input is balanced by viscous dissipation [103]. The process of energy transfer and energy loss by dissipation is supported by the flow motions that make up the turbulent flow field. These fluid motions may be characterised in terms of coherent structures, which are defined by Robinson [83] as "a three-dimensional region of the flow over which at least one fundamental flow variable (velocity component, density, temperature, etc.) exhibits significant correlation with itself or with another variable over a range of space and/or time that is significantly larger

than the smallest local scales of the flow". Therefore, understanding the structure and the dynamics of these coherent motions gives more insight into the dynamics of turbulence [2,83]. In this thesis, the coherent motions in Taylor-Couette flow are studied.

Taylor-Couette flow facilities are typically closed environments, where the working fluid is confined radially between the cylinders, and axially by endplates. Therefore under stationary conditions it is relatively easy to monitor the energy balance. The input to the system is made via the differential rotation of the cylinders. This energy input is balanced by the viscous dissipation. Assuming that the temperature of the working fluid, cylinders and the surrounding environment is in equilibrium and constant, and if small losses such as mechanical friction of the bearings and other mechanical components are neglected, the net energy flux is zero. Therefore in Taylor-Couette flow, the energy loss due to the viscous dissipation is equal to the measured torque [80]. This makes the Taylor-Couette geometry almost ideal for controlled-turbulence studies. Additionally, when the Taylor-Couette facility has a transparent outer cylinder, it is possible to observe the elementary flow characteristics with different visualization techniques, in parallel to torque measurements [28].

1.2 Current Issues

An extensive characterization of flow regimes in Taylor-Couette flow, based on flow visualization analysis, was reported by Andereck et al. [7], which is regarded as a reference for defining the flow patterns in Taylor-Couette flows. Apart from the famous Taylor vortices, they observed many distinct regimes. Remarkably, recent studies [15, 16, 33, 36, 76, 77, 82, 109, 110] mostly focused on the part that Andereck et al. [7] initially labeled as "featureless turbulence". Actually, they named the fully turbulent flow regime as featureless turbulence, simply because they could not observe any large-scale organised motion due to limitations of the qualitative visualisation technique they used. Later studies showed the presence of coherent motions in this turbulent state, similar to those found in other wall-bounded turbulent flows [33, 111].

In recent years, the number of experimental studies on Taylor-Couette flow increased in parallel to the research groups owning Taylor-Couette

devices (Burin et al. [17], Ravelet et al. [82], Borrero-Echeverry and Schatz [14], Paoletti and Lathrop [76], van Gils et al. [108], Avila and Hof [9], Merbold et al. [69]) focusing on different aspects of the flow. Due to the direct relation between the torque and turbulence as mentioned above, the studies performing the torque measurements are mostly focused on the turbulent flow regime at relatively high Reynolds numbers ($Re = Ud/\nu \sim 10^5 - 10^6$, where U is the velocity of the inner or the outer cylinder that is rotating, d is the gap width between the cylinders, and ν is the kinematic viscosity) [76,77,108,109]. Studies revealed the torque-scaling as a function of Reynolds number [36]. Measurements at different Reynolds numbers and different relative rotation speeds of the cylinders revealed that, depending on the relative rotation speeds of the cylinders, the torque changes for constant Reynolds number. Especially in the case of counter rotation the change is most pronounced [76,82,109]. The results showed the presence of an optimum angular momentum transport at counter rotation of the cylinders (at $-\Omega_o/\Omega_i \approx 0.4$, where Ω_i and Ω_o represent the angular velocity of the inner and the outer cylinders, respectively) [109]. Ravelet et al. [82] speculated that the change of the torque values and the presence of the optimum transport could be explained by the coherent turbulent flow structures in the flow. However, this was not supported by the available measurement data.

Implementation of torque acquisition systems to Taylor-Couette devices are generally done during the manufacturing phase of Taylor-Couette apparatus, and require extensive engineering. On the contrary, compared to optical measurement techniques, torque measurements are relatively easier to perform. The implementation of optical measurement techniques to a Taylor-Couette geometry are relatively harder for several reasons. The curvature of the cylinder walls is one of the difficulties for the optical measurement techniques. The optical distortion as a result of refraction at the curved cylinder wall increases with the curvature of the cylinder. This problem can be solved by implementing a water filled optical box over the outer cylinder [114,115], although it limits the rotation of the outer cylinder. The addition of refractive index changes (caused by the use of water as a working fluid) in the optical path, illumination difficulties, reflection issues and moving outer cylinder wall increases the complexity of the optical arrangement. Hence, the application of optical measurement techniques to the Taylor-Couette flow is relatively limited. Initial optical experiments were mostly qualitative

visualisations and based on simple arrangements [7, 21, 22, 101]. Still, they were quite successful to identify different flow regimes, transitions and stability issues. However, when it comes to turbulent flow, due to the chaotic nature of the turbulence, the dynamics of the flow is generally very hard to understand with simple visualisations, and therefore quantitative techniques are required.

The development of particle image velocimetry (PIV) enabled measurements of the instantaneous velocity flow field in a planar domain. However, due to the optical problems mentioned before, it has not been widely used in Taylor-Couette flow when compared to other flows. A first time application was shown by Wereley and Lueptow [114, 115], who implemented 2D PIV to Taylor-Couette flow and measured axial and radial velocity components. Their work initiated the usage of PIV in Taylor-Couette flow to investigate different aspects of the flow [1, 6, 27, 52, 80, 96, 111, 112], as well as stereo PIV to measure all three velocity components in a plane [82]. But these implementations only provided measurements in a single plane, while for the analysis of the flow dynamics, volumetric measurements, for example with tomographic PIV [42], are required. On the other hand, especially for the investigation of turbulent flows, the spatial resolution of the tomographic PIV raises questions at this point about its ability to resolve small scales. Higher spatial resolution is required to capture small scale structures in the flow [5]. Although Worth et al. [122] compared tomographic PIV measurements with DNS to study the spatial resolution, the actual spatial resolution of tomographic PIV has not been studied in the literature using actual experiments.

On the other hand, with the improvement of computational capacities, Taylor-Couette flow has been studied numerically by several authors [10, 13, 15, 16, 32, 33, 74]. These DNS studies focused on the different aspects of the flow, such as torque, turbulence, boundary layers and stability. Mainly because of the current computational capacity, these studies are mostly limited to low Reynolds numbers ($Re \sim 10^3$), with the exception of the work by Brauckmann and Eckhardt [15, 16] and Ostilla-Mónico et al. [75] ($Re \sim 10^4 - 10^5$). Among these numerical studies, the work by Dong performed at conditions of only inner cylinder rotation [32] and exact counter rotation [33] of the cylinders, showed the coherent turbulent flow structures in the instantaneous and mean Taylor-Couette flow and their contribution to the Reynolds stress.

In addition to the specific studies on Taylor-Couette flow, the apparatus can also be used to investigate dynamics of wall-bounded turbulent flows. Dynamics of turbulent flows is an important part of our understanding of turbulence and it has been studied widely in the literature [2,83,97]. Introduction of time-resolved tomographic PIV enabled investigation of temporal evolution of the turbulent flow structures in a true volumetric domain [51, 71, 91, 92]. As the rotation speeds of the cylinders can be controlled independently, it is possible to have turbulent flow ($Re \sim 10^3 - 10^4$) with small convection velocity using Taylor-Couette apparatus. Applying time-resolved tomographic PIV to Taylor-Couette geometry, the coherent flow structures can be tracked over the spatial domain for relatively longer duration compared to boundary-layer flow. This fact can be used to improve our understanding on the dynamics of the wall bounded flows.

1.3 Aim of the Thesis

The studies in fully turbulent Taylor-Couette flow raised several questions: how are the three-dimensional topologies of coherent flow structures? How do the coherent flow structures change with the relative rotation speeds of the cylinders? Can we relate the change of the torque scaling with the coherent turbulent motions? How do the large-scale and small-scale turbulent motions contribute to the torque? From a measurement perspective, what is the actual resolution of tomographic PIV, and how effective is it to capture different scales of turbulent flow? Which variable (i.e. size of interrogation window or distance between two vectors) defines the actual spatial resolution for tomographic PIV? Is there an optimum spatial resolution to resolve small scale motions in turbulence? Furthermore, we can increase our knowledge on the dynamics of wall-bounded turbulence using time-resolved tomographic PIV in Taylor-Couette apparatus by answering questions like how do the coherent flow structures convect and evolve, and what are the mechanisms they experience during their lifetime?

In order to answer these questions, we need to slightly change our approach. As turbulence is a 3D phenomena, a volumetric measurement technique is preferred to properly reveal the details of the flow. For this purpose, it is decided in this study to implement tomographic parti-

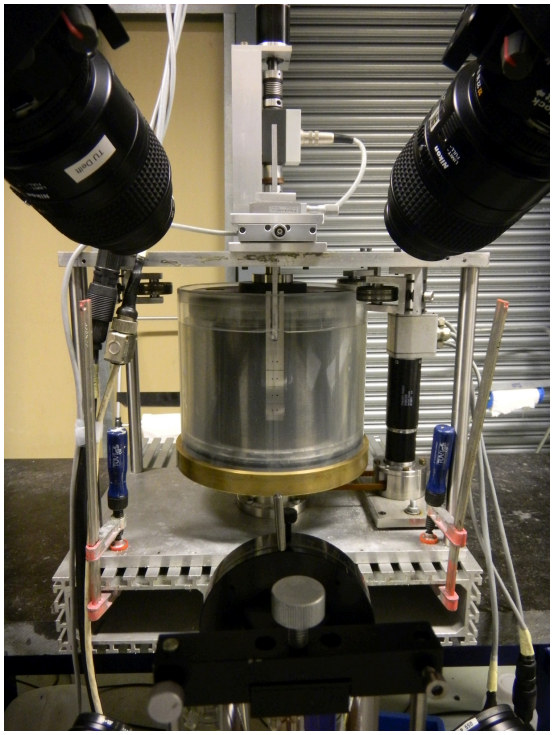

Figure 1.1: Picture of the Taylor-Couette setup, taken between the high-speed cameras. Please note the top plate was removed and the calibration target was placed in the setup as it is done during acquisition of calibration images.

cle image velocimetry (tomographic PIV) [42] to a Taylor-Couette flow facility (Figure 1.1). The questions stated above are aimed to be answered by investigating the fully turbulent Taylor-Couette flow, mostly focussing on the coherent turbulent flow structures in relation to the relative rotation speeds and directions of the cylinders and torque.

As mentioned above, optical distortions, such as the curvature of the cylinders, change of the refractive index, a moving medium between the cameras and the flow (i.e. a rotating outer cylinder), and reduced image quality due to reflections, are potential error sources for tomographic PIV. As this is the first implementation of tomographic PIV to a Taylor-Couette geometry, initially the method needs to be validated.

Therefore, the study starts by validating the implementation by comparing the velocity measurements to analytically well defined laminar Taylor-Couette flow (described in Chapter 2).

The spatial resolution of the measurement technique is crucial, especially for turbulent flows. The spatial resolution of the technique should be high enough to capture the small-scale structures. However, the actual spatial resolution of the tomographic PIV is limited by the number of the particles that can be recorded [5, 42]. Typically a high interrogation volume overlap is used for vector calculation. Therefore, frequently the number of the measured vectors is an order of magnitude higher than the number of particles in the flow. Hence the actual spatial resolution of tomographic PIV is poorly defined. Although similar studies were performed for 2D PIV, the actual spatial resolution of tomographic PIV has not been studied until recently. Worth et al. [122] performed spatial resolution analysis by using DNS data, which excludes the effect of several sources of error that appear in actual experiments. In this study Taylor-Couette flow is used to obtain experimentally validated estimates of the spatial resolution of tomographic PIV, by making use of the fact that the turbulent dissipation rate is directly related to the applied torque [80]. The actual dissipation rate can be determined from the measured torque on the cylinders, while it is also possible to estimate the dissipation rate from the full deformation rate tensor that is measured with tomographic PIV. Hence, it is possible to compute the dissipation rate by two independent methods, i.e. torque measurements and tomographic PIV. The comparison of the estimated dissipation rates can be used to assess the actual resolution of the tomographic PIV.

Additionally time-resolved tomographic PIV is applied to turbulent Taylor-Couette flow. This work aims at improving our understanding of the dynamics of turbulence. Although the pointwise and planar measurement techniques are well developed and quite useful for explaining the statistical aspects of the turbulence, the complexity of turbulent flow limits the results to approximations, such as Taylor's frozen turbulence hypothesis [102]. Therefore, time resolved volumetric measurements are required to understand the dynamics of turbulent flow [91, 92]. High-speed tomographic PIV provides fully volumetric time-resolved measurements of the flow. It enables one to track turbulent flow structures and to study their evolution. For this purpose, as a part this study, measurements are performed at exact counter-rotation of the cylinders. Under

this condition, the fully turbulent flow has approximately zero mean azimuthal velocity. This results in a longer observation duration compared to similar studies performed in other flows [40, 41, 51, 71, 91, 92].

Finally, the study focusses on the relation between the torque and coherent structures in turbulent Taylor-Couette flow. The aim is to study the large-scale structures at constant Reynolds number in fully turbulent Taylor-Couette flow, and to study how they change with different relative rotation speeds of the cylinders. The large-scale structures can be defined as the structures that are mostly influenced by the flow geometry (unlike the small scales, which should be universal), with their sizes comparable to the flow scale. They are primarily responsible for the transport and mixing in the flow [79]. The aim is to examine the topology of the structures in relation to the reported change of the torque scaling [76, 77, 82, 108, 109] (see Figure 5.1 for instance), and to try to explain the torque scaling through changes in the turbulent flow structures.

1.4 Outline of the Thesis

The outline of this thesis is as follows. Chapter 2 gives details of the Taylor-Couette geometry used for this study, and explains the implementation of the tomographic PIV to the Taylor-Couette setup. Validation of the measurement accuracy is achieved by comparing the experimental data to the analytical solution for laminar flow.

Chapter 3 discusses the actual spatial resolution of tomographic PIV for fully turbulent Taylor-Couette flow. The quantification of the spatial resolution is performed by comparing the dissipation rate computed from the tomographic PIV measurements with the directly measured dissipation rate through the applied torque. A parametric study is performed to see how the spatial resolution is affected by the change of the Reynolds number, interrogation domain size, and interrogation domain overlap.

In Chapter 4, using time-resolved tomographic PIV, examples of dynamic events in turbulence are given to show the capacity and demonstrate its potential for turbulence research. Examples of tracking of the coherent turbulent motions to investigate their evolution are provided. The measurements in Chapter 4 are performed at exact counter-rotation

of the cylinders, where the mean azimuthal velocity is approximately zero. This advantage is used to track the structures for a considerably longer time compared to similar studies at the boundary layer and channel flows.

Changes in the coherent turbulent flow structures and their contribution to torque values are discussed in Chapter 5. The dependency of the large-scale structures on rotation number at constant Reynolds number are shown. Vertically aligned Taylor column-like structures are observed close to only outer cylinder rotation. The contributions of the large- and smaller-scales to torque are separately investigated by decomposing the instantaneous flow into large- and smaller-scale motions. Finally, in Chapter 6 the conclusions of this study are provided and a brief outlook for further studies is given.

2 Implementation of Tomographic PIV to a Taylor-Couette Flow Geometry

2.1 Introduction

This chapter focuses on the implementation of tomographic PIV in current Taylor-Couette setup. Since tomographic PIV relies on the precise volumetric reconstruction of the scattering sites in the measurement volume, optical aberrations that are not accounted for in the calibration can deteriorate the quality of the reconstruction. A challenge that is addressed here lies in the fact that tomographic PIV is applied to a flow domain with a curved and moving outer wall, which complicates the measurement. The reconstruction and a volumetric self-calibration can be applied to correct for small optical distortions and aberrations.

In this chapter, tomographic PIV is used to measure different flow states following the same categorization as Andereck et al. [7], and three Taylor-Couette flow regimes are considered, namely laminar flow, flow with Taylor vortices, and fully turbulent (i.e. "featureless" turbulent) flow. These regimes have increasing dissipation rates, i.e. decreasing micro length scales. For the laminar flow case there is only one dominant velocity gradient determined by the differential angular speed of the cylinders and the gap width between the cylinders. In this case the flow can be fully resolved due to the absence of any small-scale variations of the velocity. In the case of the Taylor-vortices flow regime, large-scale vortical structures are present in the flow. Also here, by absence of small-scale motions, the measurement should be able to fully resolve the flow. The fully turbulent flow regime contains small scale flow structures.

Based on S. Tokgoz et al. *Spatial resolution and dissipation rate estimation in Taylor-Couette flow for tomographic PIV.* Exp. Fluids, 53(**3**):561-583, 2012. doi:10.1007/s00348-012-1311-7

The flow is fully three-dimensional and the turbulent kinetic energy is dissipated in small-scale vortices. The scale of these vortices depends on the Reynolds number.

An outline of this chapter is as follows. Initially a brief literature review is given in Section 2.2. Then the current Taylor-Couette geometry is explained (Section 2.3). The parameters used in this thesis are defined in Section 2.4. The implementation of tomographic PIV for a Taylor-Couette flow system is discussed in Section 2.5, where several problems that were encountered during the implementation are briefly explained, as well. The validation of implementation of the experimental method is done for the analytically well-defined laminar flow case, which is basically a stable circular Couette flow, in Section 2.6. The effect of a curved and rotating outer cylinder between the flow domain and the cameras on the measurement results is tested in the same section. Then, in Section 2.7, the characteristics of Taylor-vortex flow and the fully turbulent flow regimes are analyzed. The experimental observation of the formation of Taylor vortices is also given in the same section. The results are concluded in Section 2.8.

2.2 Background

So far, field based experimental studies on Taylor-Couette flow mainly focused on 2D structures of the flow, because of the limited capabilities of available experimental methods. Wereley and Lueptow [114,115] performed the initial 2D PIV measurements in Taylor-Couette flow. However, they could only measure the axial and radial components of the flow velocity. They applied a glass box, filled with a liquid that matches the refractive index of the working fluid, that encloses the Taylor-Couette flow system in order to avoid effects due to refraction from the working fluid and the curved outer cylinder wall. Since then, 2D PIV has been used to examine different flow characteristics of Taylor-Couette flows [1, 6, 27, 80, 96, 112]. Akonur and Lueptow [6] performed planar PIV in radial-azimuthal planes in a setup very similar to the one of Wereley and Lueptow [114]. In order to obtain the third component of the velocity, they combined their results with those of Wereley and Lueptow [114], which were in the axial-radial direction. With the help of phase averaging, they obtained time-resolved, three-dimensional and

three-component PIV results. So far, their work has been the only experimental attempt to analyze volumetric flow structures in a Taylor-Couette system by means of PIV. Recently Ravelet et al. [82] applied stereo PIV to Taylor-Couette flow for the first time. They performed measurements in the axial-radial plane, where the azimuthal velocity is in the out-of-plane direction. They also performed torque measurements on the inner cylinder. The combination of stereo PIV and torque measurements was used to explore the torque scaling in relation to the flow field structure.

Despite several papers on the application of PIV to Taylor-Couette flows, the reliability of PIV measurements in Taylor-Couette flow has not been studied widely. Akonur and Lueptow [6] report an error for PIV measurements of laminar flow to be 1% for azimuthal and 4% for radial velocities, relative to the inner cylinder velocity. On the other hand, Ravelet et al. [82] showed the error level does not exceed 1% for the same components, using stereoscopic PIV measurements. However, they report a significant velocity difference in regions close to the outer cylinder walls. They attributed this to refraction effects due to the curved cylinder walls.

2.3 Taylor-Couette Geometry

The measurements were performed in the Taylor-Couette setup at the Laboratory for Aero & Hydrodynamics of the Delft University of Technology, which was used previously by Ravelet et al. [82] and Delfos et al. [25]. It consists of two coaxial cylinders that can rotate independently. Additionally, the system allows performing torque measurement on the inner cylinder shaft. The radii of inner and outer cylinders are $r_i = 110.0 \pm 0.05$ mm and $r_o = 120.0 \pm 0.05$ mm, respectively (Figure 2.1). This results in a gap of $d = r_o - r_i = 10.0$ mm, and a corresponding gap ratio of $\eta = r_i/r_o = 0.917$. The length of the outer cylinder is $L = 220.0$ mm, which gives an axial aspect ratio of $\Gamma = L/d = 22.0$. The geometric details of the Taylor-Couette setup are summarized in Table 2.1. The working fluid is water. The system is closed by top and bottom covers, which are rotating with the outer cylinder. Both cylinders are made from transparent polymethylmethacrylate (PMMA/Plexiglas), allowing optical access. However, structural metal bars, which are placed

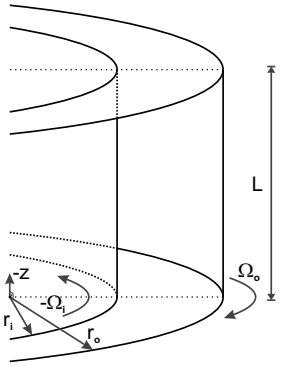

Figure 2.1: Sketch of the experimental setup given in the used cylindrical coordinate system. The dimensions are not to scale.

Table 2.1: Geometric parameters of the Taylor-Couette setup.

Symbol	Value	Unit	Meaning
r_i	110.0	mm	Inner cylinder radius
r_o	120.0	mm	Outer cylinder radius
$d = r_i - r_o$	10.0	mm	Gap width
$\eta = r_i/r_o$	0.917	-	Gap ratio
L	220.0	mm	Cylinder height
$\Gamma = L/d$	22.0	-	Aspect ratio
$R_C = d/\tilde{r}$	0.087	-	Curvature number

inside of the inner cylinder, were found to cause strong reflections, and noise on the recorded images in the case of volume illumination required for tomographic PIV (see Section 2.5.3). Therefore, another cylinder, which was painted black, was placed on the inside of the inner cylinder, to cover the structural bars. This improves the quality of the images considerably. More details of different aspects of the experimental setup is given in subsequent sections.

2.3.1 Influence of the cylinder covers

In most Taylor-Couette studies the cylinders are considered as effectively infinite. However for some situations the influence of the end plates can-

not be neglected, especially when the aspect ratio is small [21]. Therefore it is worth to mention how the top and bottom covers of the system and their influence the flow.

The top and bottom covers of our system are attached to and co-rotating with the outer cylinder. Similarly, the covers of the inner cylinder are attached to the inner cylinder. There is a 2 mm gap between the covers of the inner and the outer cylinder on both top and bottom sides, forming a so-called von Karman gap [82]. In this gap, von Karman flow appears due to the rotation of the top and bottom covers, which are acting like rotating disks. The rotation causes an outward radial motion, and an accordingly axial motion towards the disk [12,81]. Consequently this phenomenon induces a secondary flow in the vertical Taylor-Couette gap between the cylinders, with a magnitude that depends on the rotation speeds [9, 10, 17, 26, 35, 55, 77, 78]. Although the details of the secondary flow depend on the Reynolds number, Poncet et al. [78] explained the basic mechanism simply as: the fluid is pumped radially outward along the rotating disks, then the flow reaches to the Taylor-Couette gap, and moves axially to mid-height, with the flow coming from the top and the bottom meeting around the center and the fluid going back to the top and bottom endplates. The effect of the secondary flow is significant especially for small aspect ratios [21, 55, 119].

Different solutions were proposed to reduce the secondary flow, such as dividing the end covers in to multiple segments, implementing rings on the covers, as well as active control of the endplates [9,10,17,55,107]. Another relatively simple solution is to replace the cylinders with longer ones (while keeping the cylinder diameters constant) in order to achieve a higher aspect ratio [35]. However, these solutions have not been implemented to current setup because of the complexity of the modifications, so all measurements presented in this thesis were performed by using cylinders with a length of $L = 220.0$ mm, corresponding to $\Gamma = 22.0$.

Instead, the effect of the secondary flow to the measurements in this thesis were minimized by taking a few precautions. The measurements were performed at the center of the cylinder height in the axial direction ($0.4L \leq z \leq 0.6L$), where the effect of the secondary flow is minimal [110]. Secondly, most of the experiments were performed in fully turbulent flow conditions. It is known that the effect of the secondary flow is surpassed by the intense turbulent fluctuations [77, 110]. In the case of laminar flow, the measurements were performed in relatively low

Reynolds numbers, where the intensity of the secondary flow is expected to be low. In order to test the effect, the measurements were compared to analytical solutions for the laminar cases (see Section 2.6). The comparison did not show any significant deviation from the analytical results in the investigated range of shear Reynolds numbers.

2.3.2 Rotation control and torque measurements

The cylinders can rotate independently by means of two Maxon DC motors that are connected to the cylinder shafts. A custom-made regulation device is connected to the motors in order to control the rotation speed [82]. The maximum rotation frequency is 10 Hz with a precision of ± 0.02 Hz [82]. The motors can either be controlled manually or using a software (LABVIEW).

A torque meter (HBM T20WN, 2 Nm) is attached to the shaft of the inner cylinder. The acquisition rate of the torque signal is 2 kHz and the absolute precision of the torque meter is ± 0.01 Nm [82]. Measuring the torque values from the inner cylinder shaft (where the driving motor is also connected) is relatively straightforward. However, this torque measurement configuration has some disadvantages compared to other designs. In the current design, the torque meter also records other moments of forces acting on the shaft, such as mechanical friction in the bearings and the contribution of the von Karman flow [49, 82]. The contribution of the bearings was found to be negligible for the current setup [82]. The effect of the von Karman flow to the measured torque values was discussed in several studies [17, 49, 63, 82, 119]. A proper solution to minimize the contribution of the von Karman gap to torque measurements is to build the inner cylinder in multiple sections and to perform the measurements from the middle section by means of load cells [60, 108]. This enables to measure only the torque acting on the inner cylinder. However, due to the complicity of such a system, it was not implemented to the current setup. Furthermore, it is expected that the effect is minimal for geometries with high aspect ratios, as it is for the current geometry [17, 49]. On the other hand, Greidanus et al. [49] separated the contribution of the Taylor-Couette gap and the von Karman gap to the torque at high Reynolds numbers on the same Taylor-Couette setup that was used in this study. Hence, the torque values were used according to that correction in this thesis.

2.3.3 Temperature control

In the case of closed systems such as a Taylor-Couette flow, small changes in the water temperature might lead to significant effects since viscosity is temperature dependent. The friction due to the rotation of the cylinders, as well as the dissipation, produce heat, which is mostly absorbed by the fluid inside the setup. This results in an increase of the temperature of the working fluid. Especially at high Reynolds numbers, the temperature can increase quite rapidly. If it is not handled carefully, this might result in a difference between the viscosity at the beginning and the end of the measurements. Therefore the Reynolds number can change during the recording of each case.

Different solutions on the temperature control for Taylor-Couette can be found in the literature. One of the relatively simpler (and most common) solution is to place the Taylor-Couette system in a fluid bath, where the temperature of the fluid in the bath is controlled [1, 9, 96, 114]. However, this has disadvantages like limited outer cylinder rotation capacity and limited optical access. Most of the experiments in this kind of Taylor-Couette setups were performed with a stationary outer cylinder. Another solution is to cool the system by the help of a cooling fluid circulated inside of the top and bottom covers [63, 108]. However, this solution is relatively more complicated to implement, and can cause significant temperature gradients in the axial direction, especially for tall geometries.

In the current Taylor-Couette system, it is not possible to directly control the temperature of the working fluid. However, similar to previous studies [6, 17, 80, 115], the fluid and the ambient temperature were measured carefully between the recordings of each data set, and the angular velocities of the cylinders were adjusted to compensate for the temperature dependent fluid viscosity, so that a constant flow Reynolds number could be maintained. When the temperature difference between the beginning and the end of each set of recordings exceeds 0.5 °C, the data were considered invalid and were not used. Thus, variations of the operating temperature of the working fluid were less than ±0.5 °C for the results presented in this thesis. The ±0.5 °C change in the operating temperature results in a maximum of 1.2% uncertainty in the kinematic viscosity of the fluid, which is water for the current study. Since each set of experiments takes around 20 minutes (except the measurements

in Chapter 4, which are even shorter; of the order of few minutes), including the period to achieve stationary flow conditions, and given that the measurements were performed at relatively low angular velocities, this approach is assumed reliable.

2.4 Parameters

Taylor-Couette flow can be described by different sets of parameters. The preferred set has changed over the years. In this thesis the parameters defined by Dubrulle et al. [35] were adopted to characterize the Taylor-Couette flow. The Reynolds numbers for inner cylinder and outer cylinder, based on the gap between the cylinders (d), are traditionally defined as

$$Re_i = \frac{r_i \Omega_i d}{\nu}, \tag{2.1}$$

and

$$Re_o = \frac{r_o \Omega_o d}{\nu}, \tag{2.2}$$

respectively. These Ω_i and Ω_o represent the angular velocities of the inner and the outer cylinders, and ν represents the kinematic viscosity of the fluid. It should be noted that although a "negative" Reynolds number is physically meaningless, it is commonly used in Taylor-Couette studies [7, 33]. The sign of the Reynolds number defines the rotation direction of the cylinders in this case.

Dubrulle et al. [35] introduced new parameters, based on flow dynamics, to define the flow and make it comparable to other rotating and shear flow types. Shear Reynolds number (Re_S) is a measure of the shear rate between the cylinders, and it will be used throughout this study. The shear Reynolds number is defined as:

$$Re_S = \frac{2\,|\eta Re_o - Re_i|}{1+\eta}, \tag{2.3}$$

where η ($= r_i/r_o$) is the gap ratio.

Another parameter called rotation number (R_Ω) was introduced in the same study [35]. The rotation number gives information about the relative speeds and the directions of the cylinders. It depends on the

gap ratio, η, and the Reynolds numbers of the cylinders, and is defined as:

$$R_\Omega = (1-\eta)\frac{Re_i + Re_o}{\eta Re_o - Re_i}. \tag{2.4}$$

In case of exact counter rotation (i.e. cylinders are rotating with the exact same wall velocity, but they are rotating in opposite direction; $r_i\Omega_i = -r_o\Omega_o$), the rotation number is $R_{\Omega,c} = 0$, regardless of the gap ratio. For the current setup the case with only inner cylinder rotation (i.e. the outer cylinder is at rest) is given by $R_{\Omega,i} = -(1-\eta) = -0.083$. Any negative number in between ($-0.083 < R_\Omega < 0$) represents the counterrotating cases where the inner cylinder is rotating faster than the outer one. Corresponding rotation number for the opposite situation of only the outer cylinder rotation (i.e. the inner cylinder is at rest) is $R_{\Omega,o} = (1-\eta)/\eta = 0.091$. Similarly any positive rotation number in the $0 < R_\Omega < 0.091$ range stands for the counter-rotation, where the outer cylinder rotates faster than the inner cylinder.

It is known that the curvature of the cylinders affect the flow characteristics as well as the angular momentum transport [17, 35]. However, the subject has not been studied parametrically, maybe due to the fact of "being more difficult to isolate" as Dubrulle et al. [35] mentioned. In the same work, they defined the curvature number as:

$$R_C = \frac{d}{\tilde{r}} = \frac{1-\eta}{\sqrt{\eta}}. \tag{2.5}$$

The $\tilde{r}$ is defined as "typical radius" and given as $\tilde{r} = \sqrt{r_i r_o} = 0.115$ m. The curvature of the current setup is $R_C = 0.087$, which can be considered as a small curvature (i.e. close to plane Couette flow, where $R_C \to 0$) compared to the literature [35]. The experimental parameters and flow conditions used in this chapter and Chapter 3 are summarised in Table 2.2.

Table 2.2: Flow conditions of the laminar (LF), Taylor vortex flow (TVF), and fully turbulent flow (FT), that were used in this chapter and Chapter 3. Parameters of the tomographic PIV measurements for the flow conditions are given on the right hand side. Δt is the exposure time delay. The number of vectors are given in the x, y and z directions, respectively (see Figure 2.2 and 2.3); δ_x stands for the distance between the vectors. The number of vectors and δ_x values are given for evaluations with $40 \times 40 \times 40$ voxel^3 final interrogation windows with a 75% overlap.

Flow Type	Re_i [-]	Re_o [-]	Re_S [-]	R_Ω [-]	Ω_i [rad/s]	Ω_o [rad/s]	Δt [ms]	Rec. Rate [Hz]	Number of vectors [-]	δ_x [mm]
LF	-	643	615	0.091	-	0.48	10.0	4.70	$107 \times 61 \times 28$	0.370
TVF	1000	500	565	-0.231	0.88	0.38	12.5	4.70	$92 \times 61 \times 28$	0.370
FT4700	1850	-2900	4700	0.019	1.57	-2.26	2.5	4.70	$92 \times 61 \times 28$	0.370
FT3800	1900	-1900	3800	0	1.63	-1.51	5.0	7.55	$107 \times 55 \times 26$	0.391
FT6200	3100	-3100	6200	0	2.70	-2.45	5.0	7.55	$107 \times 55 \times 26$	0.391
FT11000	5500	-5500	11000	0	4.78	-4.39	3.0	7.55	$107 \times 55 \times 26$	0.391
FT14000	7000	-7000	14000	0	6.09	-5.59	2.0	7.55	$107 \times 55 \times 26$	0.391
FT17000	8500	-8500	17000	0	7.41	-6.79	1.5	7.55	$107 \times 55 \times 26$	0.391
FT29000	14500	-14500	29000	0	12.63	-11.56	1.0	7.55	$107 \times 55 \times 26$	0.391
FT36000	18000	-18000	36000	0	15.65	-14.33	0.5	7.55	$107 \times 55 \times 26$	0.391
FT47000	23500	-23500	47000	0	20.42	-18.72	0.25	7.55	$107 \times 55 \times 26$	0.391

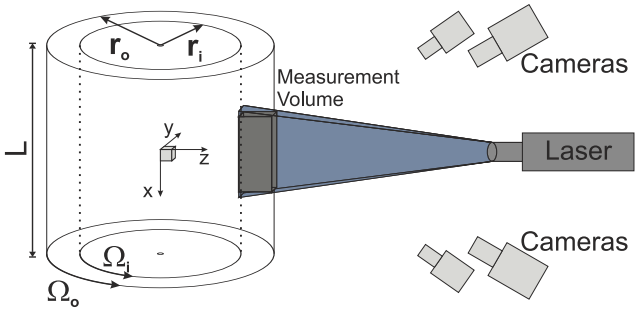

Figure 2.2: Sketch of the tomographic PIV setup and definition of the Cartesian coordinate system in the measurement volume; x axial, y azimuthal, and z radial direction. The positive angular velocities (Ω_i and Ω_o) are in the direction of the positive y in the azimuthal direction.

2.5 Tomographic PIV Setup

Velocity measurements in this thesis were done using the tomographic PIV (Figure 2.2) method [42]. Tomographic PIV is a fully volumetric method, which allows us to measure all three velocity components in the instantaneous flow field. Similar to other PIV methods, the flow is seeded with tracer particles and illuminated by a light source. In the case of tomographic PIV a flow volume is illuminated, rather than a thin light sheet. Using the displacement of the particles over a known time difference (between two frames), the velocity vectors in the measurement volume can be computed. The work flow of the tomographic PIV can be summarized in the following steps: image acquisition with multiple cameras, volume reconstruction, vector calculation via correlation, and validation of the vectors. These steps are explained in the following sections. More detailed reviews of the developments and applications of the tomographic PIV can be found in publications by Elsinga et al. [37, 39, 42], Scarano [87], and Westerweel et al. [116].

2.5.1 Image acquisition

In case of tomographic PIV the images of the particles following the flow are simultaneously recorded with multiple cameras from different viewing angles. Due to the cost restrictions and practical issues, the optimal

number of the cameras is given as four [42], but several studies using more cameras can be found in the literature [45, 65]. One important issue related to the image recording for tomographic PIV is the depth-of-field. In principle, independent of their position in the measurement domain, all of the particles should be in focus to achieve a good image quality. Since the particles recorded in a volume instead of a plane, the focal depth of the cameras should be large enough to cover all images in the illuminated volume [37,42,87]. This can be adjusted by using the aperture of the objectives (typically $f/8 - f/11$) as the depth of focus increases with the f-number. However, the amount of light captured by the camera is inversely proportional to the square of the f-number. Thus, an optimum condition should be found in order to have all the particles in focus while maintaining a reasonable intensity. The f-numbers used in this thesis are indicated in each chapter.

Another problem related to the focusing occurs due to the off-axis viewing of the cameras. If the sensor plane of the camera, the lens-plane of the objective, and the image plane are not parallel to each other, the image can only be focused sharply by tilting the camera and the objective with respect to each other, so that the Scheimpflug condition is satisfied [42, 87, 116]. For this purpose, an adapter with adjustable tilt angle can be placed between the camera and the objective, as it is mostly used in stereo PIV.

For the data described in this chapter, the recording and the image analysis were done using commercial software (DAVIS by LaVision GmbH). Four cameras (Imager Pro LX 16M) were used in double frame mode for recording particle images with a resolution of 4800×3200 pixels for laminar, Taylor vortex, and a fully turbulent flow case with $Re_S = 4700$ and $R_\Omega = 0.019$. Only about 1000×600 pixels were used for all cases in order to achieve a higher image recording rate (up to 7.55 Hz) and to remove the unused part of the images. Recording rate and laser pulse separation differ for each flow condition (see Table 2.2). Objectives with a $f = 105$ mm focal length and $f/8$ aperture were used during the image acquisition, which were mounted on Scheimpflug adapters. In order to minimise the effect of the end gaps of the Taylor-Couette facility on the measurements (see Section 2.3.1), the images were recorded at the mid-height of the rotational axis of the Taylor-Couette setup (Figure 2.2). The dimensions of the volume recorded by all cameras is roughly $40 \times 20 \times 10$ mm^3 in axial, azimuthal and radial directions, respectively.

One pixel in the recorded image corresponds to 37 μm in the flow field. The reconstructed volume size changes slightly between individual experiments.

It is convenient to interrogate the tomographic PIV data in a rectangular volume, although a cylindrical coordinate system is more appropriate for the Taylor-Couette geometry. In order to avoid interpolation errors in the conversion between coordinate systems the Cartesian representation is followed throughout this thesis, except for Chapter 5. The correspondence between the Cartesian and the cylindrical coordinate systems for the measurement volume is given in Figure 2.3. Since the axial direction, x, is completely collinear in both coordinate systems, it is not shown in the figure. As shown, the z and r directions are collinear only in one axial-radial plane, where $\theta = 0$. On the other hand, the y and θ directions are collinear on the same plane, as well. Hence, x, y and z components of the measured velocity data corresponds to axial, azimuthal and radial components of the velocities at the cylindrical coordinate system on the collinear plane. Thus, the z-coordinate and r-coordinate are interchangeable, whereas the y-coordinate and θ-coordinate also coincide in this selected plane. Please note that all 2D plots in Chapter 2, 3 and 4 are plotted on this collinear plane.

2.5.2 Flow seeding

All PIV methods require the flow to be seeded with particles that are small so they can follow the flow, and yet large enough so they scatter sufficient light to be captured with the cameras [5]. The density of each particle must be similar to the density of the working fluid in order to avoid a significant influence of buoyancy.

At the beginning of our experiments, the image quality was tested with non-fluorescent particles (Figure 2.4(a)). It was found that reflections from the cylinders, especially the small scratches on the outer cylinder surface, reduced the image quality significantly below an acceptable level. Although it can be improved via image preprocessing, fluorescent (Fluostar) particles, which contain Rhodamine B, with a mean diameter of 15 μm [56] were applied instead (Figure 2.4(b)). These particles have a density of 1.1 g/cm^3. Even though these particles are not neutrally buoyant, the settling velocity [5] of the particles is 13.7 $\mu m/s$. In this thesis, the experiments are performed at the azimuthal velocities that

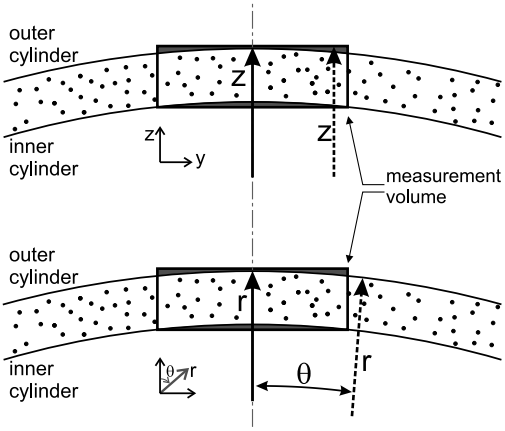

Figure 2.3: Representation of the Cartesian (top) and cylindrical (bottom) coordinates for the experimental setup. Grey areas represent the zones which are included to reconstructed volume, but are outside of the cylinders. Thus, they do not contain actual particles. Ghost particles appear in the gap between the cylinders as well as in the outside of the cylinders (grey areas).

are at least three orders of magnitude higher than the settling velocity of the particles. Therefore the error caused by the buoyancy of the particles is negligible.

The fluorescent particles absorb green light of the laser and emit fluorescent light at higher wavelengths (580 nm for current case). Optical 570 nm lowpass filters were applied for rejecting the non-fluorescent illumination during the image acquisition. In order to have a homogeneous seeding distribution, the water containing the seeding particles was mixed at high speeds of the inner and outer cylinders prior to each experiment. Then, the system was stopped and the fluid motion was allowed to settle down. After that, the cylinders were taken to the desired rotational speeds, and PIV images were recorded after the flow reached a stationary state. The whole procedure (including mixing, settling down and reaching the stationary state) takes approximately 15 minutes.

The seeding density is kept low in order to achieve a high quality in the tomographic reconstruction [42]. The quality of the tomographic reconstruction decreases with the increasing number of, so-called, ghost particles. Ghost particles can be considered as reconstruction noise [44].

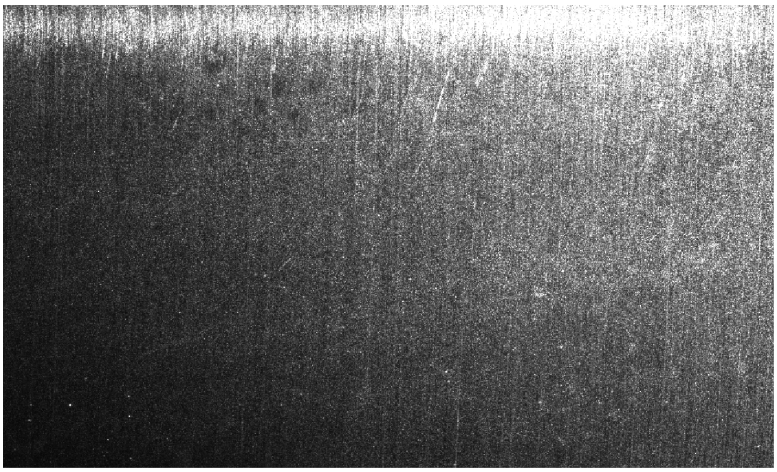

(a)

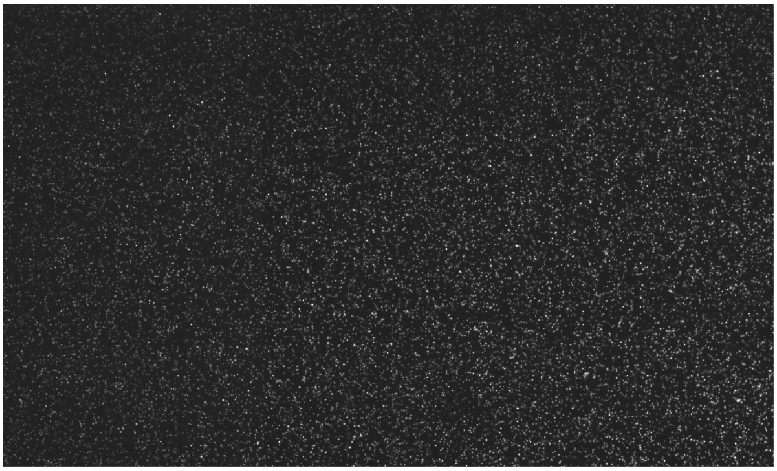

(b)

Figure 2.4: Instantaneous example images with non-fluorescent particles (a) and fluorescent particles (b) in Taylor-Couette geometry.

They are unreal particles that appear alongside the actual ones. Their position depends on the camera viewing angles and the location of the actual particles [73]. Their presence can cause a significant bias error on the velocity, and especially on the gradients [44]. Simulations and experiments show that the number of ghost particles increases with seeding density [42,44]. Therefore, one should be careful on deciding the seeding density for tomographic PIV, which should be relatively lower than 2D or stereo PIV. A detailed discussion on ghost particles, their formation and their effects on the results were presented by Elsinga et al. [42, 44]. The reconstruction quality is proportional to the signal-to-noise ratio (SNR) between the number of actual (N_p) and the ghost particles (N_g), which is given by

$$SNR = \frac{N_p}{N_g} = \frac{pppl_x l_y}{(pppA_p)^N l_x l_y l_z} = \frac{1}{ppp^{N-1} A_p^N l_z}, \tag{2.6}$$

where ppp is the number of particles per pixel area, A_p is the effective particle image area in pixels, N is the number of cameras and l_x, l_y, l_z are the dimensions of the reconstructed volume in voxel units [44, 122]. A voxel is a volumetric element, which is a three-dimensional equivalent of a pixel [116]. In this thesis, the relative size of a voxel to a pixel is 1.

On the other hand, a high seeding density is desired to achieve better spatial resolution [5]. Thus, a compromise should be found between reaching a higher spatial resolution and reducing the number of ghost particles. Based on these considerations and given the additional complexity of curved and moving walls, the seeding density was kept around the lower value of 0.025 'particles per pixel' (ppp) for the measurements presented here. Since four cameras were used during the experiments $N = 4$. The depth of the measurement volume is $l_z = 270$ pixels and $A_p = 2.5$ pixel. This results in a SNR of 6.1, which is significantly above the minimum level of 2 that indicates a high quality tomographic PIV measurement [44]. The corresponding source density is $N_S = 0.18$, which is sufficiently low to exclude speckle effects in the recorded images [5]. The high quality of the tomographic reconstruction is also observable in the radial profile of the intensity distribution in the reconstructed volume (Figure 2.5), which reveals the sharp contrast between the intensity inside and outside the liquid-filled gap.

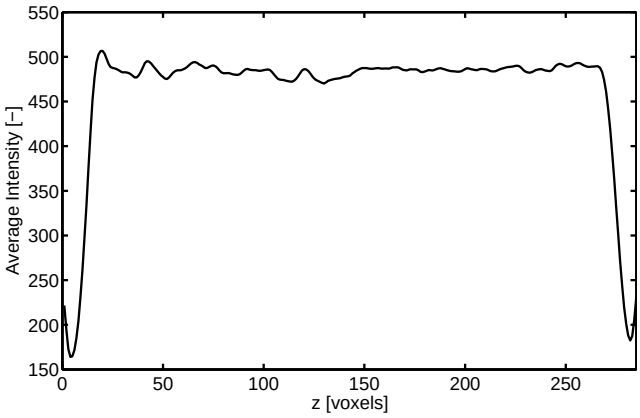

Figure 2.5: Mean intensity profile along the z-direction (see Figure 2.2 and 2.3) in the reconstructed measurement volume (over 150 instantaneous volumes). A width of 10 mm corresponds to 270 voxel units.

2.5.3 Illumination

Generally lasers are the most commonly used light sources for all PIV applications. The most significant difference between 2D/stereo PIV and tomographic PIV is the fact that the illumination for the tomographic PIV is done in a 3D volume and planar illumination is required for the 2D or stereo PIV techniques. This is generally achieved by increasing the thickness of the light sheet with lenses up to typically a few centimetres. Therefore the quantity of the required light source is relatively higher compared to 2D and stereo PIV methods [87].

The light source for illumination in Chapter 2, 3 and 5 was a double-pulsed Nd:YAG laser (New Wave Solo-III) with 50 mJ/pulse energy at a wavelength of 532 nm. The used optics with an anti-reflection coating consisting of two spherical lenses ($f = -50$ mm, $f = -40$ mm) and one cylindrical lens ($f = +200$ mm), which were placed between the laser and the test section to achieve the necessary dimensions of the laser beam for the illumination of the measurement volume.

2.5.4 Calibration

PIV requires calibration to map object planes onto image planes. The tomographic reconstruction algorithms rely on accurate mapping of the

camera images with respect to each other [42, 87, 116, 118]. Therefore, the procedure for the calibration of the tomographic PIV system consists of two main steps. The first step is to determine the mapping of the calibration planes to all cameras, as it is usually done in stereo PIV. The second step is the volumetric self-calibration method [118] for refining the calibration.

Initially a known marked target is imaged simultaneously by all cameras. The distance between the marks, as well as the size of the marks for some cases, provide the information about the scaling and the positioning of the cameras with respect to each other. However, due to the thickness of the measurement volume, generally it is needed to traverse the calibration target in the depth direction (radial direction for current case) and record images at multiple locations in the 3D volume [42]. This is needed in order to perform a calibration along the depth of the volume.

In this thesis, the calibration of the camera system was done using a 1 mm thick, flat plate made from stainless steel (Figure 2.6(a)). The dimensions of the plate are 150×20 mm^2, where the short edge is placed tangential to the azimuthal flow direction (Figure 2.6(b)). Circular holes with diameter of 0.4 mm were drilled. The distance between subsequent holes is 2.5 mm in both vertical and horizontal directions. At least 8 holes in all directions were present in each of the calibration image recordings. The calibration target was placed on a translating and rotating traversing mechanism, capable of positioning the target with micrometer precision (Figure 2.6(c)). Due to the thickness of the target and the curvature of the cylinder, the calibration target can be translated only over 50% of the gap width. Thus, calibration images were recorded in three selected planes. The calibration for the remaining 50% of the gap was computed by extrapolating the calibration function. During the calibration the gap between the cylinders was also filled with water to match with the experimental conditions. The curved outer walls of the cylinders introduce some optical distortion. However, these distortions are small enough so that they can be compensated for in the calibration.

Since the tomographic reconstruction requires an error level better than 0.4 pixel [42] and the extrapolation of the mapping function can introduce further uncertainties, the volumetric self-calibration [118] was applied for further refinement of the calibration. Using triangulation of the actual particle images recorded by all cameras, the volume self

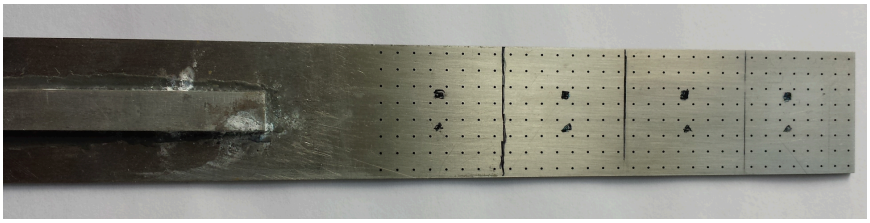

(a)

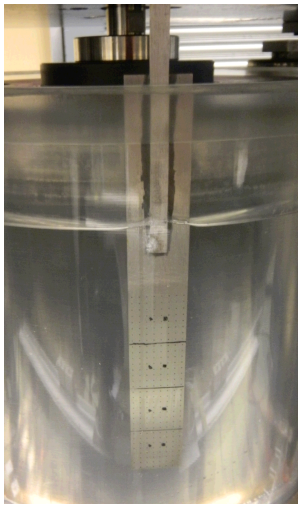

(b)

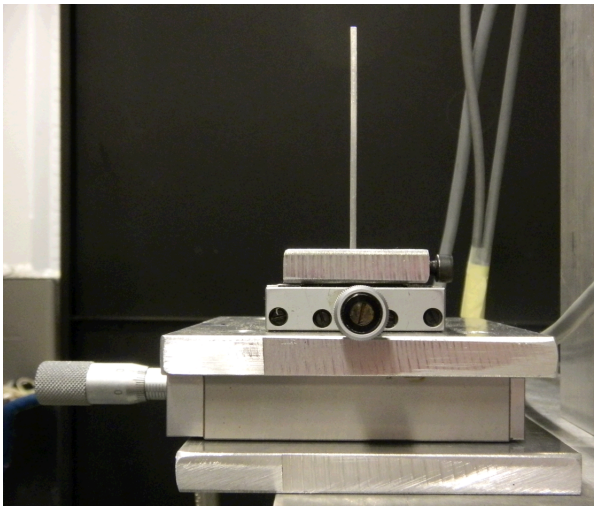

(c)

Figure 2.6: Calibration target (a), placed in the gap filled with water between the cylinders (b) and the side view of the double-axis traversing mechanism connected to the calibration target (c). The lines and marks on the target are drawn for orientation.

calibration computes the disparity (or triangulation error) [118]. The disparity is used to improve the calibration map. Iteratively repeating the volume self calibration increases the accuracy of the calibration and therefore the results. After several refinement steps with volumetric self-calibration, the maximum calibration error could be reduced from 0.329 pixel to 0.019 pixel for the current application.

2.5.5 Image processing, reconstruction and vector validation

The most significant difference of tomographic PIV with respect to the other PIV techniques might be the volume reconstruction step. Basically in this step the intensity values (of the seeding particles) recorded from different viewing angles are used to accurately reconstruct the position of the particle in the 3D volume. In practice, using the "multiplicative algebraic reconstruction technique" (MART) algorithm, recorded intensities in the 2D images are converted into the 3D particles in a 3D measurement volume [37,42]. The reconstruction is an iterative method and requires lots of computational power. However, typically 5 iterations are enough for an acceptable accuracy [87]. Several new approaches to the reconstruction are developed recently [8,30,31,70,73,121]. However, it is not intended to go into details of different reconstruction methods in this study. All volume reconstructions presented in this thesis are performed using MART algorithm, which is accepted as the standard method.

Due to its nature, the reconstruction step is sensitive to the intensity at the background [42, 87]. The quality of the reconstruction improves when the intensity of the background is removed by a simple additional pre-processing step before the reconstruction [5, 42, 87]. Thus, image processing was performed to reduce the effect of background noise and to increase the image quality of the recorded images. First, a sliding minimum intensity of 25×25 pixels was subtracted from all images to increase the signal to noise ratio. Then a smoothing with a 3×3-pixel Gaussian kernel was applied to reduce noise level and improve particle reconstruction quality for small particles [37, 120].

The intensity distribution averaged over 150 reconstructed volumes along the z direction is given in Figure 2.5. The distribution shows that the illuminated volume occurs for voxels located at $19 \leq z \leq 266$. Outside that region, the intensity values decrease approximately to one-third

of that inside. The steep drop of the intensity indicates the presence of the cylinder walls. The comparison of intensities inside and outside of the cylinder walls reveals the contribution of ghost particles to the reconstructed volume [42], which appears to be 35% of the total intensity. The reconstructed volume size was around $40 \times 20 \times 10$ mm^3. This corresponds to a resolution of approximately 27 voxel/mm.

The displacement of the particles between two reconstructed volumes are computed by 3D cross-correlation. The 3D cross-correlation is the three-dimensional version of the widely used 2D correlation and therefore relatively straightforward [87, 116]. For the experiments of all flow types represented in this thesis, the adaptive multi-pass approach was used for correlation. Unless stated otherwise, in this thesis the interrogation window size was 60×60×60 voxels with a 50% overlap in the first pass and 40×40×40 voxels with a 75% overlap in the final two passes. Spurious vectors were detected and removed by the universal outlier detection method [117]. Linear interpolation was used to fill the gaps where the vectors were removed.

2.6 Validation Using the Laminar Flow

The laminar flow case with only the outer cylinder rotating provides a steady flow that can be used to assess the accuracy of the tomographic PIV method. Therefore in this section, the accuracy of the tomographic PIV is discussed using the laminar velocity profile, RMS and number of outliers in the vector fields.

2.6.1 Velocity profiles

Laminar Taylor-Couette flow is analytically well defined, with zero axial and radial velocities, and with an axisymmetric azimuthal velocity, v, given by [35]:

$$v(r) = Ar + \frac{B}{r}, \tag{2.7}$$

where, r is the radial distance with respect to the common axis of rotation, and A and B are constants, defined as [35]:

$$A = \frac{1}{1-\eta^2}\left(\Omega_o - \eta^2\Omega_i\right), \quad B = \frac{r_i^2}{1-\eta^2}\left(\Omega_i - \Omega_o\right), \tag{2.8}$$

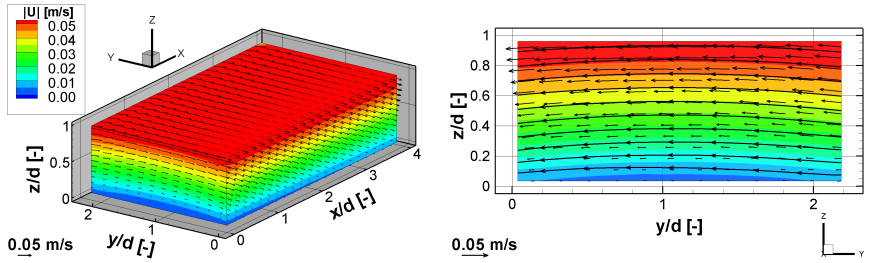

Figure 2.7: 3D plot (left), and 2D cross-section (right) of the laminar Taylor-Couette flow, obtained from 150 time-averaged instantaneous vector fields. Only every 5^{th} vector in the x and y directions and every 2^{nd} vector in the z direction are shown. Color coding represents the absolute velocity ($|U| = \sqrt{u^2 + v^2 + w^2}$). The data are represented in a Cartesian coordinate system (see Figure 2.2 and 2.3), where $z = 0$ corresponds to the inner cylinder surface, and $z = 1$ corresponds to the outer cylinder surface. Both images are non-dimensionalised with the gap width d between the cylinders.

where, Ω_i and Ω_o are the angular velocities of the inner and outer cylinders, respectively.

Laminar flow measurements were performed with only the outer cylinder rotating (i.e., $\Omega_i = 0$). Corresponding Reynolds and rotation numbers are summarised in Table 2.2. If $\Omega_i = 0$ in equations 2.7–2.8 there we have for the estimated velocity:

$$v(r) = \frac{\Omega_0}{1 - \eta^2} \left(r - \frac{r_i^2}{r} \right). \tag{2.9}$$

The measured 3D velocity fields are shown in Figure 2.7. The curved streamlines are in correspondence with the curvature of the cylinders.

Quantitative comparison between the analytical result and the measurements is necessary to assess the reliability of the method. The results are plotted in Figure 2.8, where the velocity profile of $v(r)$ appears as linear for $\eta = 0.917$. Flow profiles presented here were obtained from an average over 150 instantaneous 3D vector fields. The profile of the azimuthal velocity (v) is in good overall agreement with the analytical solution. The difference between the analytical solution and the

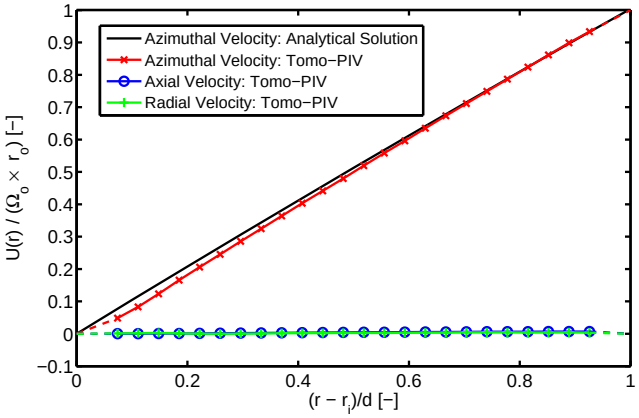

Figure 2.8: Mean velocity of the laminar flow with only the outer cylinder rotating ($\Omega_o = 0.48$ rad/sec, $\Omega_i = 0$, $Re_o = 643$, $R_\Omega = 0.091$, $Re_S = 615$), as a function of the radial distance. Time-averaging was performed over 150 instantaneous vector fields. All velocities are normalised with the azimuthal velocity of the outer cylinder ($\Omega_o \times r_o$). The dashed lines connect the measured data points and the theoretical values at the walls.

tomographic PIV results does not exceed 3.2% of the outer cylinder velocity anywhere between the cylinders. Especially, in the region of $0.20d \leq r - r_i \leq 0.50d$ the deviation is below 2.5%, and in the region $0.50d \leq r - r_i \leq 0.95d$ it is below 1%. Additionally, the maximum absolute values for the axial (u) and the radial (w) velocity components, which should be identical to zero, are within 0.7% and 0.5% of the outer cylinder velocity, respectively. Presence of non-zero axial and radial velocities can be explained as the result of the finite height of the experimental setup, which results in large-scale Ekman-like circulation [35] (see Section 2.3.1). Since the velocity deviation is always below 3.2%, the effect of a moving and curved wall between the test section and the cameras appears not to significantly deteriorate the measurement quality.

Coles and Van Atta [23] performed laminar flow measurements in Taylor-Couette facility with hot-wire anemometry, when only the outer cylinder is rotating at a constant speed with Reynolds numbers between $Re_o = 2000$ and 12000. They reported a strong disturbance of the

laminar flow in the mid-plane of axial direction, which is increasing with the Reynolds number. This distortion effect was not observed during current experiments, which is possibly due to the relatively low Reynolds number in current experiments. Ravelet et al. [82] found that the error level between analytical calculations and measurements was higher close to the outer cylinder ($0.7d \leq r - r_i \leq d$). They concluded that the reason behind this is the refraction close to curved wall. However, for the results presented here, the disagreement is found to be of the same order for both regions close to the inner and outer cylinder walls, with a slightly higher value near the inner cylinder. In the current case, the camera viewing directions were much closer to the normal of the cylinder wall, which may have helped to eliminate the errors due to refraction.

2.6.2 RMS of the velocities

In order to check the accuracy of the method, the RMS of the measured fluctuating velocity deviations from the mean velocity profile were also calculated (Figure 2.9). For the azimuthal velocity v, the RMS reaches its maximum value of 4.8% of the outer cylinder velocity. The maximum occurs at the outer cylinder wall. However, for $0 \leq r - r_i \leq 0.85d$, it is always below 1.5%. On the other hand, RMS values of axial and radial velocities are below 0.64% and 2.0%, respectively, of the outer cylinder velocity. High RMS values for $0.85d \leq r - r_i \leq d$ might be caused by the low SNR close to walls. This is probably due to the effect of the boundaries of the measurement volume and ghost particles, which is explained in detail below. High RMS values might also be related with slight unroundness of the cylinder.

PIV measurements in the vicinity of the edges of the measurement domain are generally problematic. One of the reasons is the lower probability to find sufficient particle images in the interrogation window. A lower number of particles reduces the height of the correlation peak, which defines the measurement quality. This applies in particular to tomographic PIV, where the reconstruction is done in a volume that is slightly larger than the illuminated volume. Ghost particles are formed randomly throughout the reconstructed volume, whereas actual particles only exist in the illuminated volume between the cylinders. Although the number of the ghost particles remains constant, the ratio of the ghost particles to the actual particles in the interrogation windows becomes

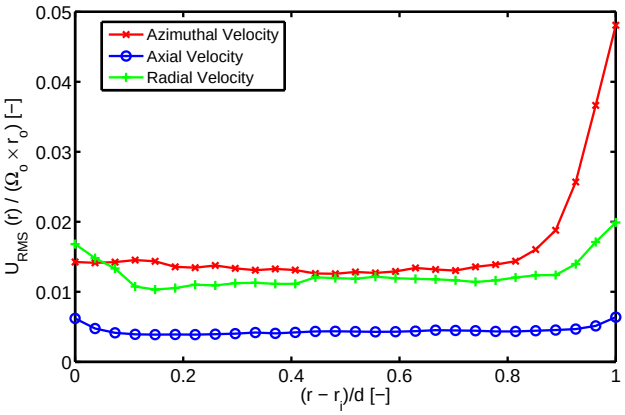

Figure 2.9: RMS of velocities, based on the time-average of 150 instantaneous vector fields of laminar flow with only the outer cylinder rotating ($\Omega_o = 0.48$ rad/sec, $\Omega_i = 0$, $Re_o = 643$, $R_\Omega = 0.091$, $Re_S = 615$), as a function of the radial distance. All RMS values are normalised with the azimuthal velocity of the outer cylinder ($\Omega_o \times r_o$).

larger in the vicinity of the cylinder walls, where the interrogation windows partially overlap with the walls. The measured velocity component is affected by the presence of the ghost particles. Consequently, the signal strength, i.e. the height of the correlation peak, is reduced in the vicinity of the inner and outer cylinder walls. This explains the higher error levels and the increase of the number of outliers near the cylinder walls.

The Taylor-Couette setup has one more disadvantage. The tomographic reconstruction implementation that was used here allows a reconstruction in a rectangular geometry only. In order to reconstruct the full measurement depth at positions where $\theta \neq 0$, one should include the external part of the cylinders of the Taylor-Couette setup (represented by the grey regions in Figure 2.3).

2.6.3 Number of outliers

Another criterion that defines the quality of PIV measurements is the number of the invalid vectors per velocity field. The percentage of the invalid vectors to the total number of vectors for an instantaneous ve-

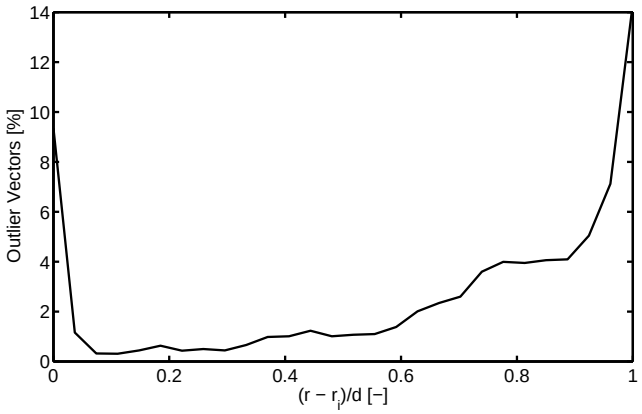

Figure 2.10: The percentage of outlier vectors to the total number of vectors in the same radial-axial cross-section, as a function of the radial distance. Calculated by 40×40×40 voxels final interrogation window, with a 75% window overlap.

locity field is given in Figure 2.10. Except for the regions close to the cylinder walls ($0 \leq r - r_i \leq 0.04d$ and $0.85d \leq r - r_i \leq d$) the number of invalid vectors is below 4.1% of the total vectors. The value increases from 5% to 14% in the region $0.85d \leq r - r_i \leq d$. Since the percentage of the outliers are below 4% for most of the measurement volume, one can use slightly smaller interrogation windows for vector calculations in order to achieve a higher spatial resolution, which was not performed for current study.

2.7 Results

In this section, the aim is to show the advantage of implementing tomographic PIV to Taylor-Couette setup by showing few examples on different flow conditions. Starting with the famous Taylor vortex flow, observations on Taylor vortex formation and fully turbulent flow will be discussed.

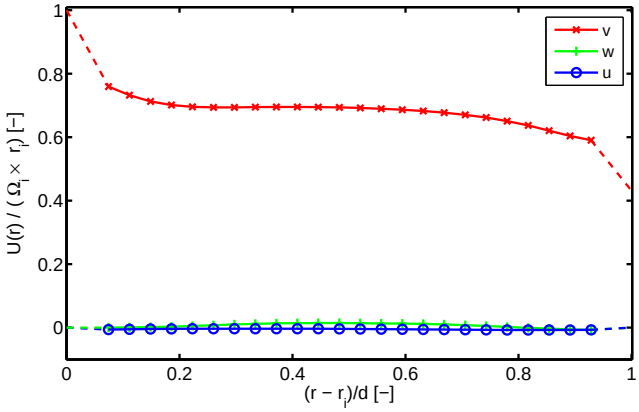

Figure 2.11: Mean velocity of the Taylor vortex flow with co-rotation of cylinders ($\Omega_o = 0.38$ rad/sec, $\Omega_i = 0.88$ rad/sec, $Re_o = 500$, $Re_i = 1000$, $R_\Omega = -0.231$, $Re_S = 565$), as a function of the radial position. Time-averaging was performed over 300 instantaneous vector fields. All velocities are normalised with the azimuthal velocity of the inner cylinder ($\Omega_i \times r_i$). The dashed lines simply connect the measured data points to the theoretical values at the walls.

2.7.1 Taylor vortex flow

The measurements for Taylor vortex flow were performed at angular velocities of the outer and inner cylinders of $\Omega_o = 0.38$ rad/sec and $\Omega_i = 0.88$ rad/sec, respectively. Corresponding Reynolds and rotation numbers are $Re_S = 565$ and $R_\Omega = -0.231$ (Table 2.2). The measured flow profile based on an average over 300 instantaneous velocity fields is given in Figure 2.11. In addition to vorticity calculations (Figure 2.12), the vortical motion of the flow can be represented by means of the Q-criterion [53], of which isosurfaces are shown in Figure 2.13.

Two significant properties can be concluded from the plots. The first one is the inclined elliptical shape of the Taylor vortices. The inclination axes have an angle of $\pm 25°$ with the azimuthal direction of the cylinders. The high-velocity radial flow in between adjacent vortices might be responsible for the inclination of the vortex shapes. For instance, at $x/d \approx 1$ in Figure 2.12, both vortices with positive and negative vorticity are tilted outwards. This can be associated with the strong

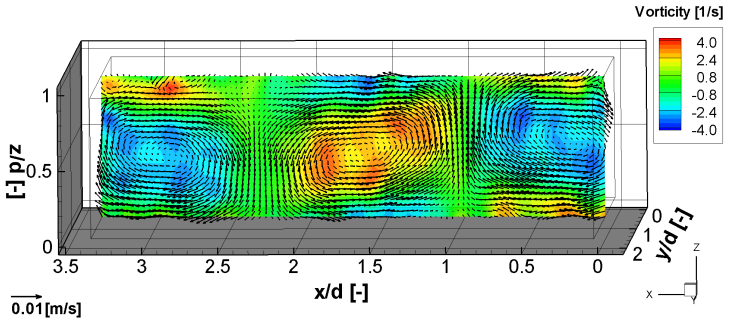

Figure 2.12: Instantaneous representation of vorticity and velocity vectors for Taylor vortex flow ($Re_o = 500$, $Re_i = 1000$, $R_\Omega = -0.231$, $Re_S = 565$), given at a cross-section at the center of the measurement volume in the azimuthal direction (y). Vorticity in the azimuthal direction is color coded. The vectors represent the velocity components that are tangential to the cross-sectional plane.

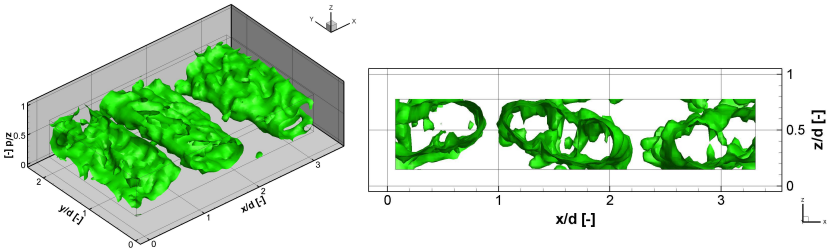

Figure 2.13: The isosurfaces for constant values of the Q-criterion [53] ($Q = 0.25$ s^{-2}) determined from the measured instantaneous flow fields of Taylor vortex flow ($Re_o = 500$, $Re_i = 1000$, $R_\Omega = -0.231$, $Re_S = 565$). 3D view (left), and side view in axial-radial plane (right).

outward flow in the radial direction between two vortices. Similarly, at $x/d \approx 2.3$ both vortices with positive and negative vorticity are inclined towards the inner cylinder, because of the strong radial inflow coming through this region. The strong inflow and outflow cause the tilting of the elliptical shape of the Taylor vortices. This is in agreement with the observations of Ravelet et al. [82], where they reported a similar deformation for $R_\Omega \leq -0.04$. Smieszek and Egbers [96] discussed similar, but less significant deformation for $Re_i = 259$ at $R_\Omega = -0.5$, with a shorter cylinder height of $\Gamma = 4.64$.

On the other hand, the inclined characteristics of the vortices resembles wavy-vortex flow. Wang et al. [112] reported inclination angles of $\pm 45^\circ$ for wavy vortex flow with a gap ratio of $\eta = 0.733$. However, there is no evidence for a significant transfer of fluid between adjacent vortices in our measurements, which is a typical property of wavy vortex flow [1, 6, 112, 114]. On the contrary, the boundaries of each individual coherent structure are well defined for the measurements presented here. Unlike wavy vortex flow [112], the boundaries between neighboring Taylor vortices are fairly stationary in current measurements.

The second property is the presence of two concentrated regions with a high vorticity level inside each individual Taylor vortex structure. If we consider the Taylor vortex in the middle of the Q-plots in Figure 2.13, the core of the vortical structure can be seen as divided into two vortices inside. This can be explained with the existence of two separate, highly concentrated, vortical regions inside each individual Taylor vortex. The high-concentration regions become more obvious if the value of Q-criterion isosurface is increased for visualisation or perform time-averaging. Any possible relation between the high concentration zones and the inclined shape of Taylor vortices will need to be confirmed in further studies.

2.7.2 Taylor vortex formation

In addition to the observations above, the formation of new Taylor vortices was observed in the present set of measurements as well. Although the measurements in the current chapter are not time resolved, the repetition rate was high enough to capture the formation. An example of the formation cycle is shown in Figure 2.14. Initially, the leading edges of a pair of counter-rotating vortical structures appear in the outflow region

between two counter-rotating Taylor vortices (Figure 2.14 (a)). They are similar both in shape, size and vorticity strength. They emerge in the region close to the inner cylinder wall and then move in the streamwise (azimuthal) flow direction. As they move forward, their size and diameter tend to expand, and they move to the center of the radial gap between cylinders (Figure 2.14 (b-g)). Their presence imposes the bigger vortices to move away from each other in axial direction. This progress continues until the diameter of the newly appeared vortical structures becomes equal to the diameter of the original structures (Figure 2.14 (h-i)). New counter-rotating vortical structures replace the previous ones at the end of the cycle (Figure 2.14 (h-i)). The opposite behaviour was observed as well. Disappearance of pairs of vortical structures follows the same cycle, but in reverse order.

In current measurements, the formation of new vortices always starts at the (radial) outflow region, while the disappearance always ends at the inflow region. Similarly, the leading edges of the new vortices appear in the vicinity of the inner cylinder, where the trailing edges of the disappearing vortices are close to the outer cylinder. It should be noted that these cycles were observed randomly both in time and space. However, it is not possible to make a guess of the appearance frequency. Thus, one should be careful when performing time-averaging over instantaneous Taylor vortex flow fields. The averaging can only be performed when the cores of the vortical structures remain at the same positions. Similar phenomena were reported by Coles [22] as well. He briefly discussed single vortex filaments that first doubled themselves, then merged again into a single vortex filament. However, for current measurements, the phenomenon was not observed as a "doubling". It is more like an appearance or disappearance of new vortex pairs in between two counter-rotating vortices. Further investigation should be done to find out any possible relation between these two incidents. On the other hand, based on visualisation experiments in a Boger fluid, Smieszek and Egbers [96] reported the continuous formation of new vortices in the middle of the axial position of the cylinders. They related the formation to the instability of the Taylor vortices. However, their observations on periodic movement of the vortex cores in the axial direction has not been observed in the measurements presented in this chapter.

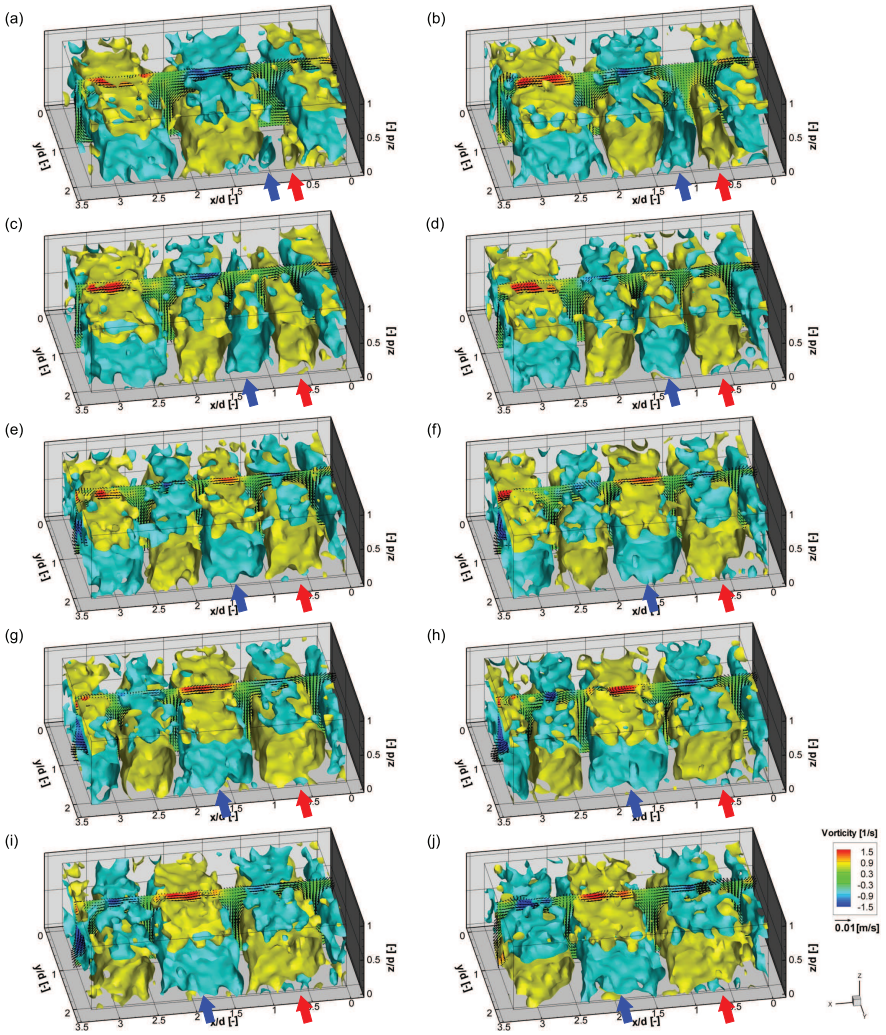

Figure 2.14: 3D representation of one cycle of the new vortex formation for Taylor vortex flow. Isosurfaces of constant vorticity values in the azimuthal direction y (yellow: 0.75 s^{-1}, blue: -0.75 s^{-1}). Blue and red arrows indicate the approximate centres of the new-forming vortical structures in the axial direction. The time differences between consequent images are $\Delta t = 0.21$ sec.

2.7.3 Fully turbulent flow

In this section, results for the characteristics of fully turbulent flow at a slightly positive R_Ω (= 0.019) are discussed. In their paper, Andereck et al. [7] defined fully turbulent flow as a region of turbulent flow without any apparent large-scale structure, and characterized the dominant length scale as smaller than the gap d for high cylinder speeds. Since they could not identify obvious structures, they identified it as "featureless turbulent flow".

The measurements presented in this section were performed when the outer and inner cylinders are rotating with angular velocities of $\Omega_o = -2.26$ rad/sec and $\Omega_i = 1.57$ rad/sec, respectively. The shear Reynolds number is $Re_S = 4700$ and the rotation number is $R_\Omega = 0.019$. Corresponding Reynolds and rotation numbers, as well as the tomographic PIV measurement parameters are labelled as "FT4700" in Table 2.2.

The measured velocity profile is given in Figure 2.15. The characteristic of the azimuthal profile is similar to results reported in the literature [33,82,106]. Since $R_\Omega > 0$, the azimuthal flow profile is not symmetric, and the plateau in the middle section is shifted in positive direction towards the velocity of the outer cylinder. The velocity near the outer cylinder wall is found to be underestimated by 11%, and near the inner wall by 47% compared to their theoretical values ($\Omega_o \times r_o = -0.27$ m/s for the outer and $\Omega_i \times r_i = 0.17$ m/s for the inner cylinder walls). This is because of the thin near-wall layer that is not resolved and gradients are underestimated due to low resolution.

A total of 300 vector fields were measured to make a further analysis of the characteristics of the time-averaged velocity field for fully turbulent flow. In contrast to findings by Dong [33] at $R_{\Omega,o} = 0$, the time-averaged vector fields do not contain any apparent large structures like Taylor vortices. Dong [33] explains the Taylor vortex-like structures in time-averaged field as the cumulative effect of instantaneous small-scale vortex organization, which results in average structures similar to Taylor vortices. If the instantaneous vector fields are considered, obvious structures similar to Taylor vortices were not observed in current measurements (Figure 2.16). However, the flow fields contain disorganised small-scale and large-scale structures, as typical for a regular turbulent shear flow.

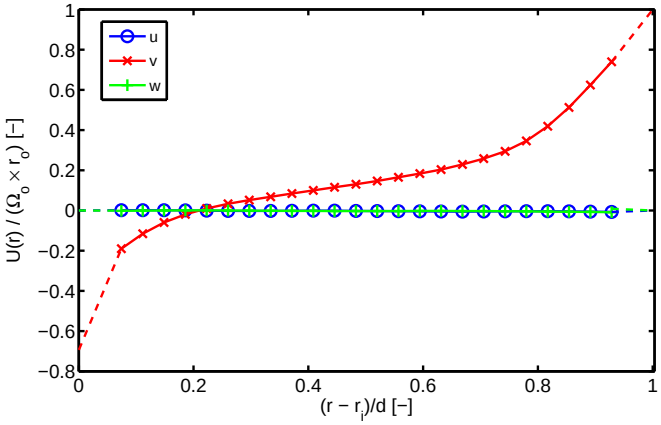

Figure 2.15: Mean velocity profile of the fully turbulent flow with counter-rotation of cylinders ($Re_o = -2900$, $Re_i = 1850$, $R_\Omega = 0.019$, $Re_S = 4700$), as a function of the radial position. Time-averaging was performed over 150 instantaneous vector fields. Spatial averaging was performed in the axial direction of the cylinders. All velocities are normalised with the azimuthal velocity of the outer cylinder ($\Omega_o \times r_o$). The dashed lines simply connect the measured data points and the theoretical values at the walls.

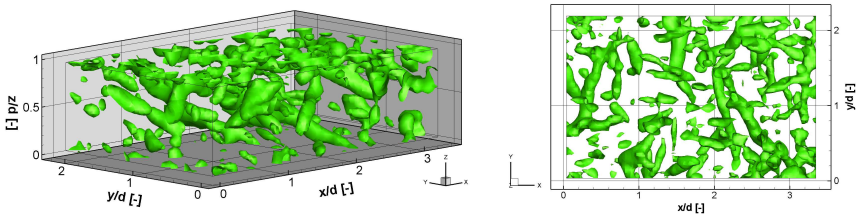

Figure 2.16: The isosurfaces for constant values of Q-criterion [53] ($Q = 400\ \mathrm{s}^{-2}$) determined from the measured instantaneous flow fields of fully turbulent flow ($Re_o = -2900$, $Re_i = 1850$, $R_\Omega = 0.019$, $Re_S = 4700$); 3D view (left), side view in the axial-azimuthal plane (right).

2.8 Conclusion

In this chapter the implementation of tomographic PIV for a Taylor-Couette flow was described. This was achieved through a rotating and curved transparent outer wall, i.e. without the usage of an enclosure to reduce the effects of refraction. Fluorescent tracer particles, appropriate optical filters and black paint on the inside of the inner cylinder were used to reduce the effects of surface reflection of the incident laser light. The accuracy of the measurement in this situation was shown from the comparison of the measured velocity in the laminar flow state with the exact analytical solution. The results showed that the measured vector fields deviates from the analytical solution by 3.2% of the outer cylinder velocity at maximum. The discrepancy is below 2.5% over 75% of the radial gap.

Measurement results for Taylor-vortex and featureless turbulence flow were also described. The inclined orientations of the Taylor vortices were shown and the absence of the large-scale vortical flow structures in the fully turbulent flow was reported. The formation of a counter-rotating Taylor vortice pair was also captured and described.

3 Spatial Resolution of Tomographic PIV

3.1 Introduction

The development of modern multi-camera methods, such as tomographic particle image velocimetry (tomographic PIV; [42]), makes it possible to measure all three components and their spatial derivatives of the instantaneous velocity field in a volumetric domain. Such data enable the investigation of the instantaneous structure of turbulent flows, and they provide quantitative experimental data on the full deformation tensor and derived quantities, such as the energy dissipation rate and vortex stretching.

For turbulence measurements it is necessary to resolve the spatial velocity gradients, which requires a high spatial resolution. However, the spatial resolution in tomographic PIV is limited by the maximum density of particle images that can be recorded [5, 42]. As a consequence, there exists an upper limit to the number of tracers within the volume. This is further augmented by the common practice to use overlapping interrogation domains, which may result in a final data density (determined by the total number of interrogation locations) that exceeds the estimated tracer particle density in the measurement volume. Hence, the question arises what the actual spatial resolution is of a tomographic PIV measurement. Recently, Worth et al. [122] used DNS of homogeneous isotropic turbulence to simulate a tomographic PIV measurement and compared them with the actual experiments, in order to discuss the resolution of 2D and of tomographic PIV. They used the discrepancies between the simulations and the measurements as indicator of the effect of the measurement noise and the spatial resolution over the velocity

Based on S. Tokgoz et al. *Spatial resolution and dissipation rate estimation in Taylor-Couette flow for tomographic PIV.* Exp. Fluids, 53(**3**):561-583, 2012. doi:10.1007/s00348-012-1311-7

and the dissipation rates. Here the effect of the resolution is considered using actual experiments instead of simulations. To validate the spatial resolution of tomographic PIV the (turbulent) dissipation rate in Taylor-Couette flow is considered. For this flow, the dissipation rate is proportional to the torque applied to the rotating cylinders [80]. Hence, there is an independent measurement for the dissipation rate, and this can be compared against the dissipation rate estimated from the velocity data. A discrepancy between these values is a measure of the accuracy and the spatial resolution of the measurement, as the dissipation rate is determined by the smallest scales that appear in the flow.

According to the energy-cascade model, the turbulent energy is dissipated on the smallest eddies, and it is important to estimate the dissipation rate for some industrial processes such as mixing [54,85,93]. The approach to determine the local dissipation rate from tomographic PIV data follows those reported by others, using planar PIV data [11,61,80, 93, 95, 100]. In order to resolve the smallest scales in turbulence and to capture the velocity gradients accurately, measurements of turbulent flows should ideally have a resolution of the order of the Kolmogorov microscale [5, 93]. Nevertheless, for accurate results, the knowledge of velocity gradients in all directions, which is not possible by 2D PIV, is required [5]. The missing data can be estimated by assuming local isotropy or by making use of symmetry properties in the statistics of the local deformation tensor [80,93,94]. Those assumptions limit the calculations because of significant non-isotropic and inhomogeneous structure of the flow [94]. Sharp and Adrian [93] showed that, using additional correction methods it is possible to measure the dissipation rate up to 70% of the actual dissipation rate. Racina and Kind [80] followed the same assumptions. They used 2D PIV measurements to calculate the dissipation rate in a Taylor-Couette system for the first time. Independent torque measurements allowed them to compare the dissipation rate measurements with their actual values. The measured energy dissipation rate showed good reproducibility according to their results.

In this chapter, instead of simulations, torque measurements are used as an independent measure to validate the tomographic PIV-based estimations of dissipation rates. Initially, the validation of the dissipation rate estimations is done by comparing them with the analytically well-defined laminar flow (Section 3.3.1). Moreover, the computed dissipation rate values are compared with the dissipation rates that were

estimated using torque measurements. Then, in the case of fully turbulent flows, the average dissipation rate is compared to the values that are obtained from torque measurements for increasing Re_S numbers. By increasing Re_S, it is possible to decrease the smallest flow scales relative to the measurement resolution. In the current chapter the effect of the Reynolds number (Section 3.4.1), the interrogation window size (Section 3.4.2), and the data spacing relative to the interrogation window size (i.e., window overlap) on the spatial resolution of tomographic PIV (Section 3.4.3) are discussed. Additionally, in Section 3.4.4 the large eddy PIV method [95] is also used to provide a more accurate estimation of the dissipation rate, and discuss its performance.

3.2 Experimental Setup

The Taylor-Couette geometry and tomographic PIV setup used in this chapter is as given in Table 2.1 and Section 2.5, with an exception of the cameras that were used. The experiments in the current chapter were performed by using four Imager Pro X 4M cameras with a resolution of 2000×2000 pixels. Similarly, approximately 1000×600 pixels were used for all cases in order to achieve a higher image recording rate. Calibration of the tomographic PIV was done using the procedure that was explained in Section 2.5.4.

3.2.1 Image processing and vector validation

Similar to Chapter 2, the adaptive multi-pass approach was used for correlation. Unless stated otherwise (see Sections 3.4.2 - 3.4.3), the interrogation window size was $60\times60\times60$ voxels with a 50% overlap in the first pass and $40\times40\times40$ voxels with a 75% overlap in the final two passes. Spurious vectors were detected and removed by the universal outlier detection method [117]. Linear interpolation was used to fill the gaps where vectors were removed. Further details on flow seeding, illumination, calibration and image processing can be found in Section 2.5.

3.3 Dissipation Rate Estimations

The dissipation rate in Cartesian coordinates, which simplifies the calculations over cylindrical coordinates in our experiments [63, 93, 94], is given by:

$$\begin{aligned}
\varepsilon &= \nu\Bigg\{2\Bigg(\left\langle\left(\frac{\partial u}{\partial x}\right)^2\right\rangle+\left\langle\left(\frac{\partial v}{\partial y}\right)^2\right\rangle+\left\langle\left(\frac{\partial w}{\partial z}\right)^2\right\rangle\Bigg)\\
&+ \left\langle\left(\frac{\partial u}{\partial y}\right)^2\right\rangle+\left\langle\left(\frac{\partial v}{\partial x}\right)^2\right\rangle+\left\langle\left(\frac{\partial u}{\partial z}\right)^2\right\rangle\\
&+ \left\langle\left(\frac{\partial w}{\partial x}\right)^2\right\rangle+\left\langle\left(\frac{\partial v}{\partial z}\right)^2\right\rangle+\left\langle\left(\frac{\partial w}{\partial y}\right)^2\right\rangle\\
&+ 2\Bigg(\left\langle\frac{\partial u}{\partial y}\frac{\partial v}{\partial x}\right\rangle+\left\langle\frac{\partial u}{\partial z}\frac{\partial w}{\partial x}\right\rangle+\left\langle\frac{\partial v}{\partial z}\frac{\partial w}{\partial y}\right\rangle\Bigg)\Bigg\} \qquad (3.1)
\end{aligned}$$

where, "$\langle\bullet\rangle$" represents an ensemble average, which in the present case is estimated by a temporal average. In addition to temporal averaging, spatial average of the dissipation rate in the axial direction is used to compute the values. The u, v and w values are the instantaneous velocities in the x, y and z directions, respectively. McEligot et al. [68] showed that in case of the dissipation rate estimations, the fluctuating velocity components are dominant in the bulk flow, while the mean flow is important in the regions close to the wall. However, since it is aimed to compute the total dissipation here, the instantaneous velocities, which include both the mean and the fluctuating velocity components, are used for the estimations.

Different to the previous efforts to compute the dissipation rate using 2D PIV measurements [11, 80, 93–95], all instantaneous 3D velocity gradients in equation (3.1) are known via tomographic PIV. As a consequence, assumptions based on flow axisymmetry or isotropy to correct the equation for missing terms are not necessary, and only directly measured values are used to compute ε [11]. The precision of the current computations is mainly limited by the spatial resolution of the measurements.

The computed dissipation rates are compared against dissipation values based on separate torque measurements (represented by ε_T) [80]. For

Taylor-Couette flow, the total dissipation of kinetic energy per unit time, must be equal to the power supplied by the rotating cylinders. Furthermore, the balance of momentum in the steady state requires the torque magnitude on the inner and outer cylinder to be equal, which reduces the expression for the mean dissipation rate per unit volume to:

$$\overline{\varepsilon_T} = \frac{P}{\rho V_f} = \frac{T|\Omega_i - \Omega_o|}{\rho V_f} \tag{3.2}$$

where P stands for the power input due to the inner cylinder rotation, T represents the torque measured on the inner cylinder, Ω_i and Ω_o are the angular velocities of the inner and outer cylinders respectively, ρ is the density of the fluid and V_f is the total volume of the fluid in the Taylor-Couette setup.

In order to compute the velocity gradients in equation 3.1, a second-order polynomial regression to the measured velocity field was done [38]:

$$\begin{aligned} f_{reg}(r_x, r_y, r_z) &= a_0 + a_1 r_x + a_2 r_y + a_3 r_z + a_4 r_x r_y + a_5 r_x r_z \\ &+ a_6 r_y r_z + a_7 r_x^2 + a_8 r_y^2 + a_9 r_z^2 \end{aligned} \tag{3.3}$$

where r_x, r_y and r_z are the relative distances from a point in the x, y and z directions, respectively. The method fits a second order polynomial function to the velocity distribution in a $5\times5\times5$ neighbourhood around a point (x_1,y_1,z_1), which acts like a filter as well [38,86]. The fit parameters a_1, a_2 and a_3 represent the velocity gradients at (x_1,y_1,z_1) in the x, y, z directions, respectively.

The PIV method encounters problems to properly resolve Kolmogorov microscales, because of the limit of the spatial resolution [5, 11, 61, 80, 93, 95, 100]. Using the dissipation rate that is estimated from the torque measurements, the Kolmogorov microscale can be defined as:

$$\lambda_K \equiv \left(\frac{\nu^3}{\overline{\varepsilon_T}}\right)^{1/4} \tag{3.4}$$

where ν is the kinematic viscosity and $\overline{\varepsilon_T}$ is the mean dissipation rate estimated from the torque measurements.

Small scale fluctuations are filtered out when the space between the vectors (δ_x) is larger than the Kolmogorov length scale [95, 100]. This results in the underestimation of turbulent dissipation rate [80, 95, 100]. In contrast, for cases where δ_x is smaller than the Kolmogorov scale length, a decreasing δ_x leads to a rapid increase of the measured dissipation rate because of the measurement noise. This noise is due to the finite measurement error [85, 100].

Another measure of the measured dissipation rate that is captured by tomographic PIV can be represented using equation 3.4, as well. It provides the information about the degree of the smallest captured scales with tomographic PIV (λ). However, $\overline{\varepsilon_T}$ should be replaced by the mean dissipation rate computed by tomographic PIV (i.e. $\overline{\varepsilon}$). The effect of the spatial resolution to the dissipation rate estimations can be evaluated by λ/λ_K ratio. The spatial resolution of the measurement is better if the ratio is closer to unity. The ratio of λ/λ_K is indicative of how well the flow has been resolved with respect to the dissipation rate estimation.

3.3.1 Laminar flow and assessment of dissipation rate estimations

Local dissipation rate estimations for the laminar flow are given in Figure 3.1. They were computed with two different approaches. The first approach is to compute the gradients and the dissipation rates from a single, time-averaged vector field, which will be referred to as "method 1". Since the time-averaging smooths the vector field, this method results in slightly lower values of velocity gradients and local dissipation rates.

The second approach, that is indicated as "method 2", is to compute the gradients and the dissipation rates for each of the 150 instantaneous vector fields individually, and then average the dissipation rates. In general, "method 2" results in slightly higher dissipation rates, since it includes the contribution of random noise in the measured velocity. The difference between these two methods is also plotted in Figure 3.1. Both methods yield data that are in good agreement in the inner region, which might indicate that the contribution of random noise to the measured velocity in the bulk flow is relatively low. The difference is below 3.4% of the maximum dissipation rate in the region $0.1d \leq r - r_i \leq 0.85d$, which is associated with PIV noise. It is obvious that the difference between the results of the two methods is higher close to the cylinder walls. The

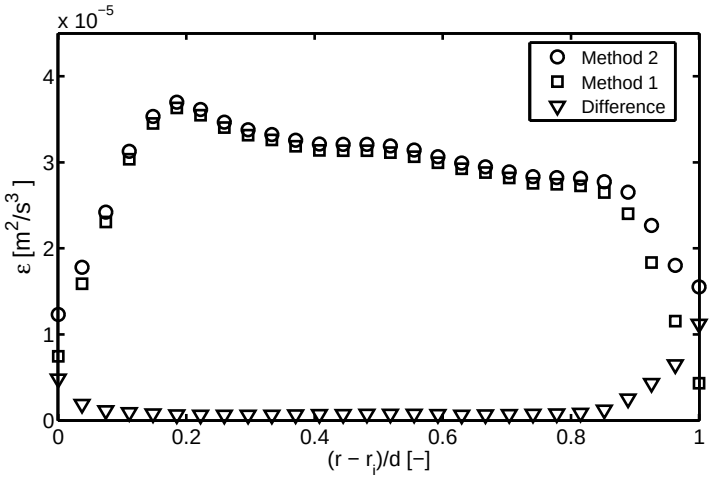

Figure 3.1: Local dissipation rate estimations for laminar flow, obtained by tomographic PIV, as a function of radial position. Calculations were performed with two methods explained in the text.

difference between the methods remains small however, indicating that the effect of random measurement noise is not significant. Since the other flow regimes are unsteady, only "method 2" is considered in the remainder of this chapter.

The analysis of individual velocity gradients reveals two dominant gradients, which are $\partial v/\partial z$ (azimuthal velocity gradient in the radial direction) and $\partial w/\partial y$ (radial velocity gradient in the azimuthal direction). These gradients are an order of 10 times higher than the remaining ones. However, all of the gradients were included in the dissipation rate estimations. The "wavy" characteristics of the local dissipation rates is caused by the step-like behaviour of the gradient $\partial w/\partial y$, which might be due to a peak locking effect [5]. Post-processing methods to correct the peak locking effect can be found in the literature [20, 84]. Since it is aimed to use the raw data without any correction, these methods were not implemented in this study.

Obviously, the measured local dissipation rates in Figure 3.1 significantly decrease towards the walls. This is due to errors related to the velocity gradient estimation. A second-order polynomial regression uses a $5 \times 5 \times 5$ neighbourhood of vectors at each point. Therefore, the effect

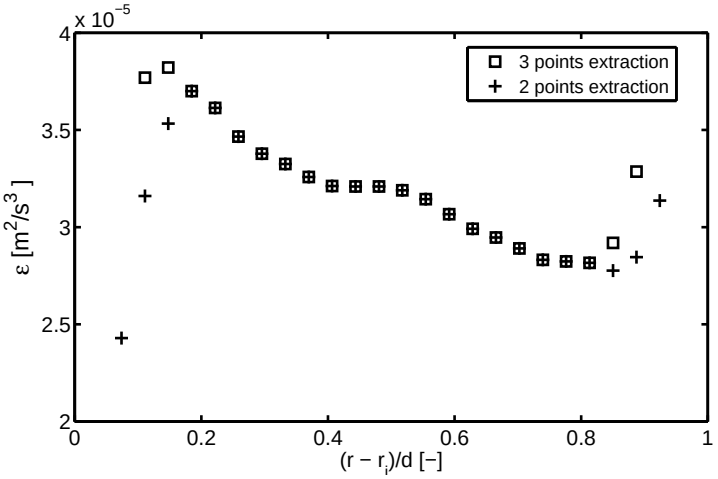

Figure 3.2: The effect of boundaries to the local dissipation rate estimations for laminar flow, as a function of radial position. 2 and 3 points extraction refers to the number of points removed from the data close to the inner and outer cylinders.

of the gradients at the borders of the domain (i.e. the cylinder walls) at both sides expands toward the inner section of the gap. This continues until the edges no longer are part of the domain of the $5 \times 5 \times 5$ kernel, which is the fourth data point from cylinder walls in the radial direction for current case. This effect was tested by excluding two and three data points from measurement domain at both sides for the velocity gradient estimations, and is plotted in Figure 3.2. The local dissipation rate in the region $0.18d \leq r - r_i \leq 0.81d$ was identical for both estimations. However, the deviation between two domains is large close towards each wall. In the case of excluding two data points from each side, the effect of the cylinder walls is still dominant in the domain. Thus, similar to Worth et al. [122], it was decided to continue with excluding three data points for the analyses with 75% overlap, unless otherwise stated (see Section 3.4 and Table 3.3 for the exceptions). It should be noted that for all of the mean dissipation rate estimations presented in this chapter, the local dissipation rates at the central plane of the measurement volume in the azimuthal direction (i.e. $\theta = 0$, see Figure 2.3) were used. Additionally, spatial averaging was performed in the axial direction in the

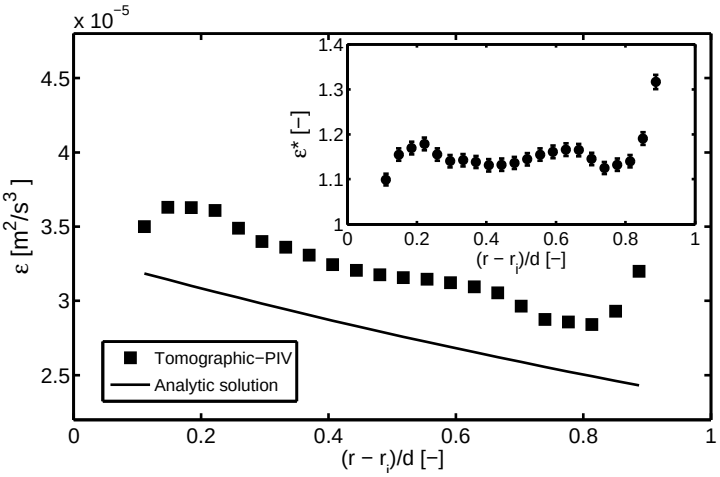

Figure 3.3: Dissipation rate estimations, computed analytically and with tomographic PIV data, for laminar flow. Plotted as a function of radial position. Spatial averaging was performed in the axial direction of the cylinders. (Inset) Normalised dissipation rate estimations for laminar flow as a function of radial position. Normalisation was performed according to the analytically computed local dissipation rates. Error bars are representing the effect of uncertainty of the kinematic viscosity due to $\pm 0.5\,^{\circ}\mathrm{C}$ temperature difference.

measurement volume, which is a homogeneous direction in the current system.

Comparison with the analytical calculations

As the laminar flow has a well defined analytical form, local dissipation rate estimations based on the measurement of tomographic PIV can be compared with the analytical calculations of the local dissipation rate. A volumetric domain of the analytical solution, which has the exact grid positions with the measured domain, was generated. Then, the same procedure for the dissipation rate estimation by tomographic PIV was followed on the analytically generated velocity vector domain. The results are shown in Figure 3.3. The local dissipation rates estimated by tomographic PIV measurements are in good agreement with analytical results. The decreasing trend through the gap is consistent as well.

In order to make a quantitative comparison, the values estimated from the tomographic PIV data were normalised with the analytical result. The normalisation of the local dissipation rate with the analytical value is given as:

$$\varepsilon^* = \frac{\varepsilon}{\varepsilon_A} \tag{3.5}$$

where ε represents the local dissipation rate estimated by tomographic PIV and ε_A stands for the local dissipation rate calculated analytically. The plot for the normalised local dissipation rate is given in the inset of Figure 3.3. The normalisation points out that the tomographic PIV measurements overestimates the local dissipation rate values everywhere. However, the difference is below 20% of the local dissipation rate, with the exception of a few data points near the cylinder walls. On the other hand, the effect of the uncertainty of the water temperature to the dissipation rate estimations are represented by error bars in the inset of Figure 3.3. The uncertainty caused by the fluctuation of the fluid temperature is relatively small compared to the deviance from the analytical solution. Hence, it can be concluded that, the error in the dissipation rate estimations of the laminar flow case is mostly due to the errors in the measurements and the estimation of the spatial derivatives.

Comparison with the torque measurements

Even though the comparison with the analytical solution is the simplest and most reliable method for the validation of the dissipation rate estimation, it is not feasible for all flow types. Another approach should be used especially for the fully turbulent flows.

An advantage of the Taylor-Couette setup is the possibility of performing torque measurements. For the experimental setup presented here, the torque of the inner cylinder can be measured by a torque-meter that co-rotates with the inner cylinder shaft. More detailed information about the torque measurements on the current experimental setup is given by Ravelet et al. [82] and Greidanus et al. [49]. Using equation 3.2, a direct comparison between the mean dissipation rate obtained by tomographic PIV and by the torque measurement can be performed. It should be noted that the working fluid in current experiments was water, and the system was operated at relatively low rotating frequencies. As

a consequence, the torque values are much lower than the limits of the measurement capability of the torque-meter. Therefore, a torque scaling of the data presented by Delfos et al. [25] and Ravelet et al. [82] was used instead. If equations 3.2 and 3.5 are combined, the normalisation of mean dissipation rate obtained by tomographic PIV ($\overline{\varepsilon}$) is done as:

$$\overline{\varepsilon^*} = \frac{\overline{\varepsilon}}{\overline{\varepsilon_T}} \tag{3.6}$$

Estimation of the dissipation rate close to the cylinder walls

Another question arises in the computations of the mean dissipation rate, $\overline{\varepsilon}$. Because of the reasons explained above, the dissipation rates close to the cylinder walls can not be estimated via tomographic PIV. However, these values are needed for computing the mean dissipation for the complete system. In order to estimate these values, a linear polynomial curve fitting operation was performed on the dissipation rate values on the radial direction. By the help of these polynomials, the dissipation rates at the cylinder walls were estimated. For the laminar flow case, all data points of the domain was used to fit the equation. Since the analytical solution shows approximately linear behaviour, this approach seems reasonable. However, as it will be discussed in the next section, the dissipation rates of the fully turbulent flows have different characteristics to that of the laminar flow. Thus, using the complete domain for the curve fitting would result in erroneous estimations for the turbulent flow cases. Hence, 3 data points, which are the closest to the cylinder walls, were used to fit linear polynomials. Two separate polynomials; one for the inner cylinder and another one for the outer cylinder (see dashed lines in Figure 3.5), were used for each case to estimate the dissipation rates at the inner and outer cylinder walls. In order to compute the mean dissipation of the Taylor-Couette system, numerical integration was performed over the measured data points in the middle region and the estimated values on the walls.

A summary of the dissipation rate estimations for all flow cases are presented in Table 3.1. Note that, for the laminar case, the Kolmogorov length scale-related values in Table 3.1 (i.e. λ_K, δ_x/λ_K, λ and λ/λ_K), are meaningless in terms of "turbulence" characteristics. However, they are presented for the aim of comparison. The mean dissipation rate for the laminar flow case ($Re_S = 615$) is in good agreement with both

estimations of the analytical value and the scaled torque data. The error level is of the order of 15%. Since the equivalent "Kolmogorov length scale" is relatively large for the laminar case, the vector spacing is smaller than this ($\delta_x/\lambda_K = 0.915$). Thus, the overestimation is caused by the noise during the measurements [5, 18, 80, 85, 100]. Tanaka and Eaton [100] reported an error level of $20 - 30\%$ at a similar δ_x/λ_K, but with a correction. It can be concluded that, without any need for a further correction, tomographic PIV has a similar order of error as for corrected 2D PIV estimations.

The different nature of the torque and tomographic PIV methods might lead to a some degree of uncertainty. Comparison of both measurements with the analytically calculated mean dissipation rate indicates an uncertainty of the torque measurements as $\approx$ 1% and the tomographic PIV measurements as $\approx$ 15%.

The mean dissipation rate estimation for the Taylor vortex flow ($Re_S = 565$) is similar to the laminar flow case. As expected, measurements are very close to resolving the flow ($\lambda/\lambda_K = 1.04$). The error level is of the order of 15% again, but the dissipation rate is now slightly underestimated. Since both large-scale flow cases have similar error levels, the discrepancy might be due to the contribution of the errors in the tomographic PIV and other effects in the estimations.

3.4 Results

In this section the fully turbulent flows are evaluated, where the aim is to investigate the relation between turbulent length scales and the spatial resolution of the tomographic PIV measurements, using three different methods. Initially, in order to understand the effect of the turbulence intensity to the dissipation rate estimations, the size of the interrogation window (IW in voxel - D_I in mm) was kept constant. In the mean time, Re_S was increased from 3800 to 47000, at an exact counter rotation of the cylinders; $R_{\Omega,o} = 0$ (Section 3.4.1). This approach results in measurements with constant spatial resolution, but decreasing Kolmogorov length scales.

Table 3.1: Results of the dissipation rate estimations for laminar flow ($Re_S = 615$), Taylor vortex flow ($Re_S = 565$), and fully turbulent flows. $\overline{\varepsilon_A}$ is the analytical estimation of mean dissipation in a unit volume, $\overline{\varepsilon_T}$ is the mean dissipation estimation from torque data, $\overline{\varepsilon}$ is the mean dissipation estimation from tomographic PIV data. $\overline{\varepsilon_{SGS}}$ is the mean dissipation estimation from tomographic PIV data, using large eddy method. $\overline{\varepsilon^*}$ and $\overline{\varepsilon^*_{SGS}}$ are the normalised values of $\overline{\varepsilon}$ and $\overline{\varepsilon_{SGS}}$, respectively. δ_x represents the distance between the vectors, λ_K is the Kolmogorov length scale computed from torque data, λ is the equivalent Kolmogorov length scale estimated from the tomographic PIV data. Velocity vectors were computed using $40 \times 40 \times 40$ voxel^3 final interrogation windows with 75% overlap (i.e. $D_I = 4\delta_x$). It is emphasized that the numerical values inside "[•]" do not represent an actual turbulence characteristic, but are evaluated for the aim of comparison. Similarly, since the large eddy method is only valid for turbulent flows, the computations with the large eddy method are excluded for the laminar and Taylor vortex flow.

Re_S [-]	$\overline{\varepsilon_A}$ [m^2/s^3]	$\overline{\varepsilon_T}$ [m^2/s^3]	$\overline{\varepsilon}$ [m^2/s^3]	$\overline{\varepsilon^*}$ [-]	δ_x [mm]	λ_K [mm]	δ_x/λ_K [-]	λ [mm]	λ/λ_K [-]	$\overline{\varepsilon_{SGS}}$ [m^2/s^3]	$\overline{\varepsilon^*_{SGS}}$ [-]
615	2.79×10^{-5}	2.76×10^{-5}	3.19×10^{-5}	1.157	0.370	[0.404]	[0.92]	[0.390]	[0.96]	-	-
565	-	2.85×10^{-5}	2.46×10^{-5}	0.862	0.370	0.412	0.90	0.427	1.04	-	-
3800	-	3.70×10^{-3}	1.97×10^{-3}	0.532	0.391	0.124	3.15	0.145	1.17	6.03×10^{-3}	1.629
6200	-	1.42×10^{-2}	3.05×10^{-3}	0.214	0.391	0.089	4.41	0.130	1.47	9.80×10^{-3}	0.690
11000	-	6.82×10^{-2}	7.25×10^{-3}	0.106	0.391	0.060	6.53	0.105	1.75	3.42×10^{-2}	0.502
14000	-	1.33×10^{-1}	1.12×10^{-2}	0.084	0.391	0.051	7.72	0.094	1.86	6.64×10^{-2}	0.498
17000	-	2.27×10^{-1}	1.58×10^{-2}	0.070	0.391	0.044	8.83	0.086	1.95	1.12×10^{-1}	0.491
29000	-	9.65×10^{-1}	3.88×10^{-2}	0.040	0.391	0.031	12.67	0.069	2.23	4.20×10^{-1}	0.435
36000	-	1.78	5.98×10^{-2}	0.034	0.391	0.027	14.76	0.062	2.34	9.50×10^{-1}	0.534
47000	-	3.75	1.19×10^{-1}	0.032	0.391	0.022	17.78	0.051	2.37	3.09	0.824

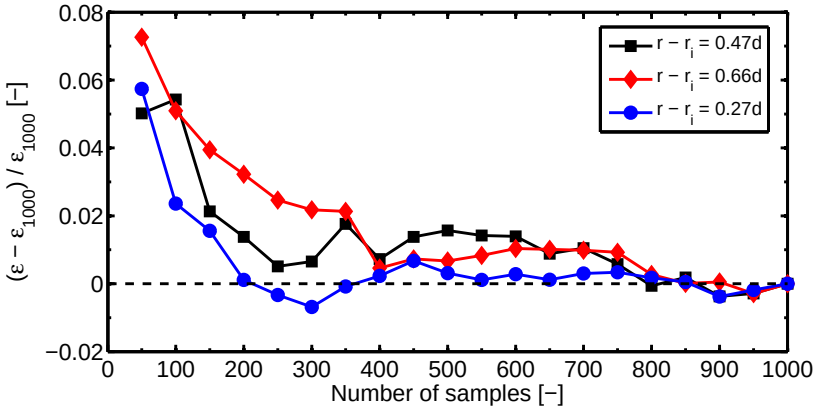

Figure 3.4: Convergence of the average dissipation rate (ϵ) with the number of frames compared to the average of 1000 frames (ϵ_{1000}), at three radial positions. Computations were performed at $Re_S = 14000$ with $40 \times 40 \times 40$ voxel^3 final interrogation window and 75% overlap.

In the second approach (Section 3.4.2), the size of the interrogation window was increased, while the shear Reynolds number remained constant. In this way, λ_K was kept constant, while δ_x increased. Worth et al. [122] performed a similar analysis, but using DNS data at a single Reynolds number.

Finally, in Section 3.4.3, the shear Reynolds number is kept constant, and the influence of different interrogation window overlap values while maintaining constant interrogation window size is discussed. This has the same effect on δ_x and λ_K as it has in the second approach. However, this approach allows to evaluate the effect of oversampling to the measurement result. Additionally, in Section 3.4.4, the dissipation rate estimates are compared with the estimates computed by the large eddy PIV method [93, 95].

Estimations of dissipation rate for fully turbulent flows were performed over 1000 instantaneous velocity fields, which is sufficiently higher than the required number of samples for statistically reliable results [11]. Tests (Figure 3.4) show that an uncertainty below 4% requires at least 150 independent vector fields, where the uncertainty level becomes lower than 1% when at least 650 vector fields are used. From this it can be

concluded that the sampling error of 1000 vector fields is below 1%.

3.4.1 Effect of Reynolds number

The results of the dissipation rate estimations for increasing shear Reynolds numbers are plotted in Figure 3.5. The plots show the characteristics of the local dissipation rates along the gap between the cylinders. The dissipation rates are increasing for increasing Re_S, as expected. The ratio between the dissipation rates at $Re_S = 3800$ and 47000 is of the order of 10^2 for the estimations via tomographic PIV. Furthermore, for each shear Reynolds number, the local dissipation rates are almost symmetrical with respect to the $r - r_i = 0.5d$ plane. The regions close to the inner and the outer cylinder have similar rates of dissipation, and they are higher than for the middle section. The local dissipation rate values reveal a plateau at the middle region. The difference between the minimum and the maximum dissipation rates for each profile decreases for increasing Re_S. Hence, the plateau becomes flatter for increasing values of Re_S.

As explained before, unlike the case for laminar flow, it is not possible to compute the dissipation rates analytically for fully turbulent flows. However, the mean dissipation was estimated using the torque data measured with the same experimental setup by Delfos et al. [25] and Ravelet et al. [82]. Results for the estimations of the mean dissipation rate are given in Table 3.1.

In the case of fully turbulent flows, the agreement between the estimates for the mean dissipation rate via torque scaling and tomographic PIV measurements are not as good as for the laminar flow case. Tomographic PIV underestimates the mean dissipation by 47% for the best case ($Re_S = 3800$), and up to 97% for higher values of Re_S. Mainly, this is the result of the finite spatial resolution of the tomographic PIV data. If the Kolmogorov scale is less than the vector spacing (i.e. $\delta_x/\lambda_K > 1$), the dissipation rate values would be underestimated [95, 100], which is due to unresolved small-scaled structures [61].

In the literature, various values of dissipation rate estimation errors have been reported. Tanaka and Eaton [100] demonstrated that at high spatial resolutions the error level might reach up to 10 times the actual dissipation value and for lower spatial resolutions the dissipation rates are underestimated. Sharp and Adrian [93] estimated the contribution

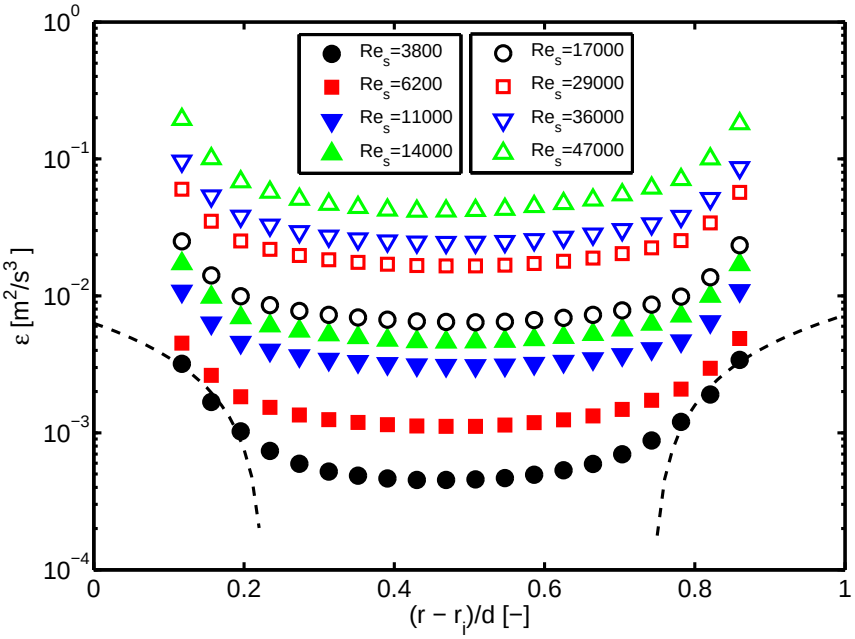

Figure 3.5: Dissipation rate estimations for fully turbulent flow cases ($Re_S = 3800 - 47000$) with exact counter-rotation of the cylinders. Profiles were computed with $40 \times 40 \times 40$ voxel^3 final interrogation window and 75% overlap. Spatial averaging was performed in the axial direction of the cylinders. Three data points in each direction near the flow boundaries were excluded in order to avoid the effect of the boundaries of the domain on the results for the estimation of the dissipation rate. Dashed lines represent the linear extrapolation to estimate the wall value for $Re_S = 3800$.

of the unresolved scales using a Smagorinsky model. They concluded that approximately 70% of the turbulent dissipation had been captured in their measurements at a spatial resolution of about 8 Kolmogorov length scales. Tomographic PIV returns similar errors at comparable spatial resolution. Racina and Kind [80] showed lower mean dissipation rates obtained from 2D PIV data with decreasing resolution, but the results are somewhat difficult to compare due to the different nature of the flow, i.e. wavy vortex flow compared to fully turbulent here.

3.4.2 Effect of the size of the interrogation window

In order to isolate the effect of the interrogation window size on the velocity vector, calculations are performed on the very same measurement data with different final interrogation window sizes. This way, the Kolmogorov length scale, λ_K, is maintained constant. This analysis was performed for $Re_S = 3800$, 14000 and 47000.

The local dissipation rate estimations for $Re_S = 14000$ with different interrogation window sizes are plotted in Figure 3.6. Since the characteristics are similar to those for $Re_S = 3800$ and 47000 those were omitted in Figure 3.6.

The effect of the interrogation window size to the mean dissipation rate is summarised in Table 3.2. Consistent with previous reports in literature [61, 80, 85, 100], the estimates are decreasing with increasing size of the interrogation windows; IW (i.e., with increasing values of D_I and δ_x), for all Re_S numbers. If the values are compared to the best estimations of each case (i.e. $IW = 40$ voxel), doubling the interrogation window size results in an average decrease of 76% for all Re_S. The difference increases to an average of 95% in the case of 4-times larger window size ($IW = 160$ voxel).

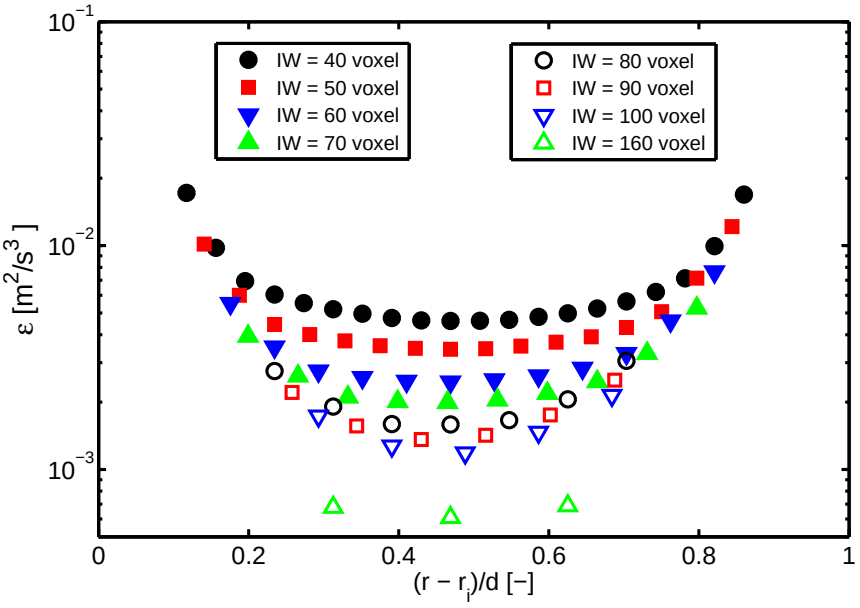

Figure 3.6: Dissipation rate estimations for changing interrogation window sizes (IW) for $Re_S = 14000$ with exact counter-rotation of the cylinders. 75% interrogation window overlapping was used for all interrogation domains. Spatial averaging was performed in the axial direction of the cylinders.

Table 3.2: Dissipation rate estimations for different interrogation window size and constant overlap value (75%). Note that the linear dimension of the final interrogation window $D_I = 4\delta_x$ for 75% overlap.

IW	δ_x	D_I	$Re_S = 3800$				$Re_S = 14000$				$Re_S = 47000$			
[vox]	[mm]	[mm]	$\overline{\varepsilon^*}$ [-]	δ_x/λ_K [-]	λ/λ_K [-]	$\overline{\varepsilon^*_{SGS}}$ [-]	$\overline{\varepsilon^*}$ [-]	δ_x/λ_K [-]	λ/λ_K [-]	$\overline{\varepsilon^*_{SGS}}$ [-]	$\overline{\varepsilon^*}$ [-]	δ_x/λ_K [-]	λ/λ_K [-]	$\overline{\varepsilon^*_{SGS}}$ [-]
40	0.391	1.564	0.532	3.15	1.17	1.629	0.084	7.72	1.86	0.498	0.032	17.78	2.37	0.824
50	0.469	1.876	0.397	3.78	1.26	1.485	0.061	9.26	2.01	0.439	0.018	21.32	2.71	0.391
60	0.586	2.344	0.273	4.72	1.38	1.273	0.041	11.57	2.23	0.358	0.012	26.64	3.00	0.310
70	0.664	2.656	0.201	5.35	1.49	1.023	0.031	13.11	2.39	0.295	0.010	30.19	3.20	0.260
80	0.782	3.128	0.119	6.30	1.70	0.530	0.023	15.44	2.57	0.245	0.007	35.55	3.44	0.223
90	0.860	3.440	0.095	6.93	1.80	0.455	0.019	16.99	2.69	0.225	0.006	39.10	3.59	0.210
100	0.977	3.908	0.076	7.88	1.90	0.432	0.016	19.30	2.82	0.225	0.004	44.42	4.06	0.220
160	1.564	6.256	0.020	12.61	2.66	0.147	0.005	30.89	3.76	0.144	0.002	71.11	4.52	0.180

3.4.3 Effect of the overlap of the interrogation window

As the last approach, the effect of the overlap value of the final interrogation volumes to the dissipation rate estimations are discussed.

It should be noted that the velocity gradient computation scheme is the same for all cases in this study (see Section 3.3 and equation 3.3). However, for the computations in this section, the kernel sizes were adjusted according to the overlap values. The $5 \times 5 \times 5$ kernel size that is used to filter the measured velocity field, is chosen equal to the interrogation window with 75% overlap [38]. In order to match the kernel size to the correlation window size at 0% and 50% overlap, $1 \times 1 \times 1$ and $3 \times 3 \times 3$ kernel are used in these cases. This means that, the velocity gradients for 0% overlap were calculated without any filtering. Thus, the expected noise level is higher for 0% overlap.

Since the kernel size is not constant, the number of excluded data points close to the cylinders are varied between the overlap values as well. Three, two and one data points were excluded from the measured domain for the analyses with 75%, 50%, and 0% overlap, respectively. The only exception to this procedure is the case of $160 \times 160 \times 160$ voxel^3 final interrogation window with 75% overlap. Since the measured data for this case contains only 7 points in the radial direction, three point exclusion results in the removal of 6 data points. Obviously, one data point in the radial direction is not enough for the total dissipation estimation, and introduces additional uncertainty. Hence, two data points were excluded from the measurement domain at both sides for the velocity gradient estimations of the corresponding case. The parameters of the velocity gradient computations are summarised in Table 3.3.

The results of changing interrogation overlap values at a constant interrogation window size of $IW = 40$ voxel are presented in Table 3.4. The dissipation rate estimations increase with increasing overlap value. Incrementing the overlap from 0% to 50% and 75%, results in $15 - 17\%$ and $55 - 60\%$ improvement of the estimation for all three values of Re_S considered here.

Table 3.3: Parameters that were used to compute the dissipation rates for the fully turbulent flow cases. "Overlap" stands for interrogation window overlap value in percentage. "Kernel size" is the number of the neighbouring data points to calculate the velocity gradients during regression analysis. "Number of excluded data points" stands for the number of the data points excluded from the measurement domain at both inner and outer cylinder sides in the radial direction.

Re_S [−]	IW [vox]	Overlap [%]	Kernel size [-]	Nr. of excl. data points [-]
All	40	75	$5 \times 5 \times 5$	3
3800, 14000, 47000	40	50	$3 \times 3 \times 3$	2
3800, 14000, 47000	40	0	$1 \times 1 \times 1$	1
3800, 14000, 47000	50, 60, ... 100	75	$5 \times 5 \times 5$	3
3800, 14000, 47000	80	50	$3 \times 3 \times 3$	2
3800, 14000, 47000	160	75	$5 \times 5 \times 5$	2

Table 3.4: Dissipation rate estimations at a constant final interrogation window size ($IW = 40$ voxel, $D_I = 1.564$ mm), but for different interrogation window overlap values.

Re_S [−]	Overlap [%]	δ_x [mm]	D_I [mm]	δ_x/λ_K [-]	D_I/λ_K [-]	$\overline{\varepsilon^*}$ [-]	λ/λ_K [-]	$\overline{\varepsilon^*_{SGS}}$ [-]
3800	0	1.564	1.564	12.61	12.61	0.200	1.50	0.295
	50	0.782	1.564	6.30	12.61	0.235	1.44	0.350
	75	0.391	1.564	3.15	12.61	0.532	1.17	1.629
14000	0	1.564	1.564	30.89	30.89	0.040	2.24	0.139
	50	0.782	1.564	15.44	30.89	0.046	2.16	0.164
	75	0.391	1.564	7.72	30.89	0.084	1.86	0.498
47000	0	1.564	1.564	71.11	71.11	0.012	3.04	0.118
	50	0.782	1.564	35.55	71.11	0.014	2.90	0.150
	75	0.391	1.564	17.78	71.11	0.032	2.37	0.824

Table 3.5: Relation between interrogation window size, vector spacing, and the dissipation rate estimations for $Re_S = 14000$. $D_I = 1.564$, 3.128 and 6.256 mm correspond to $IW = 40$, 80 and 160 voxel, respectively. Moving horizontally from left to right in a row represents the decrease of the overlap values "OL"(from 75%, 50% to 0%), at a constant interrogation window size. For each row, the first non-empty cell from the left represents a 75% overlap value for the corresponding interrogation window size. Moving in the diagonal direction from top-left to bottom-right represents the increment of the interrogation window size at a constant overlap value. For instance; the cell for $D_I = 3.128$ mm and $\delta_x = 1.564$ mm stands for a 50% overlap, whereas the cell $D_I = 6.256$ mm and $\delta_x = 1.564$ mm represents a 75% overlap.

D_I	$\delta_x = 0.391$ mm					$\delta_x = 0.782$ mm					$\delta_x = 1.564$ mm				
[mm]	δ_x/λ_K [-]	D_I/λ_K [-]	$\overline{\varepsilon^*}$ [-]	λ/λ_K [-]	OL [%]	δ_x/λ_K [-]	D_I/λ_K [-]	$\overline{\varepsilon^*}$ [-]	λ/λ_K [-]	OL [%]	δ_x/λ_K [-]	D_I/λ_K [-]	$\overline{\varepsilon^*}$ [-]	λ/λ_K [-]	OL [%]
1.564	7.72	30.89	0.084	1.86	75	15.44	30.89	0.046	2.16	50	30.89	30.89	0.040	2.24	0
3.128	-	-	-	-	-	15.44	61.78	0.023	2.57	75	30.89	61.78	0.012	3.00	50
6.256	-	-	-	-	-	-	-	-	-	-	30.89	123.56	0.005	3.76	75

The effect of overlap ratios was tested with $IW = 80$ and 160 voxels as well. For the simplicity, results are given only for $Re_S = 14000$ in Table 3.5. The performance of the dissipation rate estimations decreases for increasing vector space at a constant interrogation window size D_I. At a constant distance between vectors, δ_x, increasing the interrogation window size results in lower dissipation estimations. However, the dependency of the estimations on the change of D_I and δ_x are not the same.

3.4.4 Dissipation rate estimations with large eddy method

In order to estimate the contribution of the non-resolved scales to the dissipation rates, the dissipation rates were computed using large eddy PIV [95]. Using the sub-grid scale (SGS) flux, the large eddy method takes the unresolved scales of PIV measurements into consideration for dissipation rate estimations [93, 95].

The dissipation rate estimations by the large eddy PIV method were performed only for fully turbulent cases and are given by $\overline{\varepsilon^*_{SGS}}$ in Table 3.1, 3.2 and 3.4, in normalised form. Similar to Sheng et al. [95], $C_S = 0.17$ was used as the Smagorinsky constant for the computations. As stated by Sheng et al. [95], the Smagorinsky model results in better estimations for higher Re_S.

Comparisons show that the large eddy method results in improved dissipation rate estimations than the direct estimations by tomographic PIV, as expected. The improvement for all cases indicates that the error in the direct estimation of dissipation rates by tomographic PIV is due to the unresolved scales.

3.4.5 Summary of the dissipation rate estimations

The results are is summarised in Figures 3.7 and 3.8. As reported in the literature, underestimation of the dissipation rates is evident for fully turbulent flow cases, and the degree of underestimation increases with Reynolds numbers [61, 80, 85, 93, 95, 100].

The results show that the success of the dissipation rate estimations are strongly related to the spacing between the vectors and the interrogation window size. The error level increases with a logarithmic characteristic, as reported [11, 61, 80, 122]. Different cases with a constant

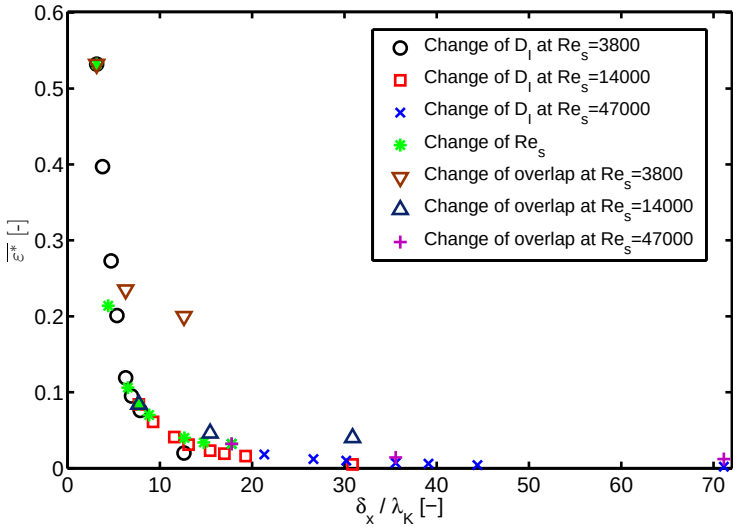

Figure 3.7: Normalised mean dissipation rate estimations of three approaches for fully turbulent flow cases with exact counter-rotation. For details, see Tables 3.1, 3.2 and 3.4.

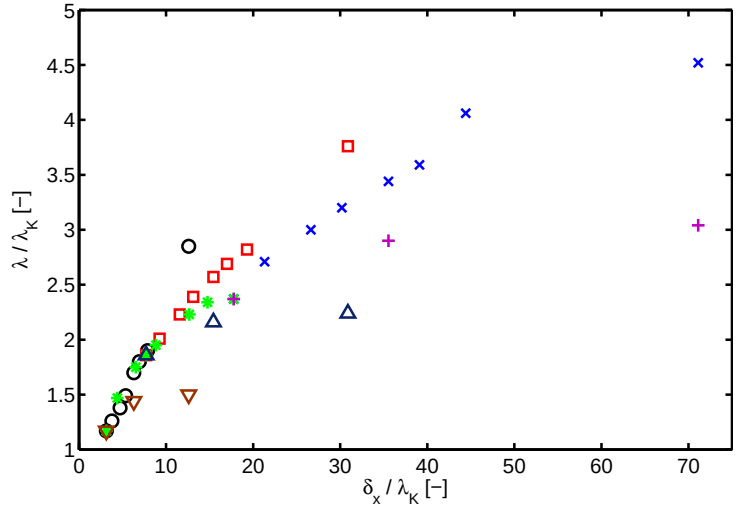

Figure 3.8: Ratio of the equivalent Kolmogorov scale over the actual Kolmogorov scale (λ/λ_K), as a function of the vector spacing relative to the Kolmogorov scale (δ_x/λ_K). The symbols follow the same coding as given in Figure 3.7.

overlap of 75% fall almost on same curve, with relatively small scatter. Decreasing window overlap at a constant interrogation window size increases the error. However, it results in lower error levels compared to similar vector spacing with larger window sizes. Hence, the dissipation rate estimations, therefore the actual spatial resolution of tomographic PIV, is a non-linear function of both δ_x/λ_K and D_I/λ_K.

Extrapolating the values in Figure 3.8 to $\lambda/\lambda_K = 1$ implies that vector spacing of $\delta_x/\lambda_K \approx 1.5-2.0$ (equivalent to window sizes $D_I/\lambda_K \approx 6.0-8.0$ at 75% overlap or $D_I/\lambda_K \approx 3.0-4.0$ at 50% overlap) is required to fully resolve the turbulent dissipation scales. This is comparable with numbers reported by Buxton et al. [18], Worth et al. [122] and Saarenrinne and Piirto [85] ($\delta_x/\lambda_K \approx 1.5 - 3.0$), which were calculated with 50% overlap. The results presented here are also seem consistent with a study by Jiménez et al. [54], who reported an average diameter of Burgers' type vortices of $6 - 10\lambda_K$.

In conclusion, the computations are more sensitive to changes of the interrogation window size than changes of the vector spacing. Although it results in a higher data density that possibly exceeds the tracer particle density, oversampling the measured data results in better estimations. The actual spatial sampling improves with the increasing window overlapping.

3.5 Conclusion

An attractive feature of Taylor-Couette flow is that it is possible to generate different flow conditions by changing the angular velocities of the inner and outer cylinders, i.e. laminar flow, Taylor-vortex flow, and turbulent flow. The laminar flow is stationary, while the Taylor-vortex flow is dominated by large-scale flow structures. The turbulent flow is without any dominant large-scale structures (i.e. "featureless" turbulence). This was utilized to determine the spatial resolution of tomographic PIV in relation to the length scales that are present in the flow. The measured torque on the cylinders is used to obtain an independent estimate of the dissipation rate, and this was compared with the dissipation rate as is estimated from the measured velocity gradients. In tomographic PIV the velocity gradients can be measured of all three velocity components and for all three principal directions.

Hence, it was possible to estimate the dissipation rate and Kolmogorov length scale without recourse to any symmetry assumptions.

As a metric to express the difference between the measured dissipation rate and the actual dissipation rate, the ratio of the dissipation rate as estimated from the PIV data relative to the dissipation rate given by the measured torque, as well as the ratio of the Kolmogorov scale determined from corresponding dissipation rates were used. Evidently, the accuracy is improved for decreasing dimensions of the (3D) interrogation window, while maintaining a minimum image density of at least 6 particle images per interrogation window. While the laminar flow and Taylor-vortex flow cases appear to be fully resolved, the turbulent flow cases are increasingly under-resolved. Only the turbulent flow with the lowest Reynolds number investigated here appears to be (almost) fully resolved. The measured dissipation rate relative to the actual dissipation rate quickly drops with increasing Reynolds number. Yet, the use of the so-called large-eddy PIV method is capable to recover most of the dissipation due to unresolved scales. It should be noted that the large-eddy PIV method is valid when the sub-grid scales are sufficiently isotropic, which may not be always the case in the present study. Most notably, the results show that an increment of the overlap ratio for subsequent (3D) interrogation windows yield improved results. It was also showed that a vector spacing in the range of $\delta_x/\lambda_K \approx 1.5 - 2.0$, which equals to $D_I/\lambda_K \approx 6.0 - 8.0$ at 75% overlap ($D_I/\lambda_K \approx 3.0 - 4.0$ at 50% overlap), should be used for a good estimation of turbulent dissipation with PIV.

It is noted that the actual accuracy is also determined by many data reduction steps and experimental parameters, such as the number of particle images inside the (3D) interrogation window, the smoothing of the measurement data or the velocity gradient computation method. They might change the contribution of the noise to the measurements. However, it was showed that the contribution of the noise to the estimations is lower (3.4% maximum) compared to other error sources. Further investigation should be done to reveal the effect of different aspects in the data reduction in relation to achieving an improvement of accuracy by means of oversampling.

4 Time-Resolved and Volumetric Inspection of a Turbulent Flow with Small Convection Velocity

4.1 Introduction

Coherent motions at turbulent flows are crucial for our understanding of the turbulence. They are associated with the transport of momentum, and with the dissipation and production of turbulent kinetic energy [2], and therefore related by the drag or torque acting on surfaces (see Chapter 5). Publications by Robinson [83], Adrian [2], Marusic et al. [67] and Smits et al. [97] give a detailed overview on the coherent structures in turbulence, especially in wall-bounded flows. Until recent years, studies were mostly focused on the statistical aspects of coherent motions in turbulence. However, with the development of new experimental techniques and numerical methods, we can now track and study the evolution of the turbulent flow structures in a true 3D volume, which makes it now possible to investigate the dynamical aspects of the coherent motions.

Previously, tracking of flow structures has been performed using basic flow visualization techniques, where instantaneous flow patterns were initially visualized by smoke or colored dye [2,24]. Although these studies were quite useful to investigate the flow topology, due to the limitation of the visualization techniques, mostly they were qualitative and focused on large scale patterns.

Early quantitative experimental studies to investigate the spatial evolution of the flow structures used point-wise measurement techniques such as laser Doppler anemometry (LDA) or hotwire probes [83]. On the other hand, planar measurement techniques like 2D and stereo PIV provided more information about the flow over single measurement plane [29, 62]. Although the methods listed above are quite helpful, especially in a statistical sense, they are either not time-resolved or volumet-

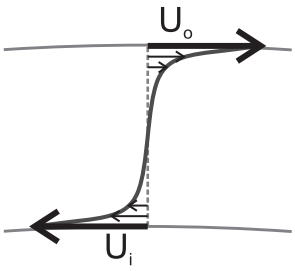

Figure 4.1: Sketch of velocity profile between two cylinders at $R_{\Omega,c} = 0$.

ric [2, 83, 92, 97].

The introduction of time-resolved tomographic PIV (or high-speed tomographic PIV) [51, 71, 89–91], enabled to study the temporal, as well as the spatial, evolution of instantaneous flow structures in a fully volumetric measurement domain. With the addition of the time evolution to the technique, the high-speed tomographic PIV sometimes is also called as "4D-PIV" [89]. Time-resolved tomographic PIV made it possible to track turbulent flow structures over space and time and to study their evolution. The initial studies of turbulence using time-resolved tomographic PIV were mostly focused on two flow types: cylinder wakes [51, 71] and boundary layers [40, 41, 46, 91, 92].

In the case of a Taylor-Couette geometry, it is possible to create fully turbulent flow with different cylinder rotation rates. In this study it was decided to use this advantage to create a fully turbulent flow with approximately zero mean velocity. This is possible by rotating the cylinders in the opposite directions with equal wall velocities. Further details on the flow conditions are given in Section 4.2. Actually, the mean azimuthal velocity can be zero at only one radial position for $R_{\Omega,c} = 0$ (see Figure 4.1). In other radial positions the advection velocity still moves the structures away from the measurement volume, especially near the walls. However, under these circumstances when the mean azimuthal velocity is very small, the flow structures are still expected to remain in the measurement domain for a extended times compared to other wall bounded flows. Using the time-resolved tomographic PIV, the aim here is to track turbulent flow structures to demonstrate the capabilities of the geometry and the measurement system for the studies on the dy-

Table 4.1: Flow conditions.

Re_S [-]	R_Ω [-]	Re_i [-]	Re_o [-]	Ω_i [rad/s]	Ω_o [rad/s]	U_i [m/s]	U_o [m/s]	Δt [ms]
3500	0	1750	-1750	1.45	-1.32	0.158	-0.158	2.288

namic events in turbulence. Tracking of the coherent structures is useful for understanding turbulence by providing more insight on the dynamic events such as the actual convection velocities, interaction between structures, and generation and breakup of structures [41]. In this chapter, different instantaneous events, such as azimuthal velocity bursts, and formation and breakup of turbulent flow structures are investigated.

4.2 Flow Conditions

As mentioned above, the turbulent flow in this chapter was created by rotating the cylinders in the opposite directions with the equal wall velocities. The experiments were performed at a shear Reynolds number of $Re_S = 3500$ (Table 4.1). The Reynolds numbers for the inner and the outer cylinders are $Re_{i,o} = \pm 1750$. The wall velocities are $U_i = 0.158$ m/s and $U_o = -0.158$ m/s, respectively, which equals exact counter rotation of the cylinders. Hence, the corresponding rotation number is $R_{\Omega,c} = 0$. Under this flow condition, the mean azimuthal velocity in the bulk of the flow is approximately zero (Figure 4.1) [33], with zero mean velocities in the axial and radial directions. The mean azimuthal velocity profile for similar Reynolds numbers ($1000 \leq Re_S \leq 8000$) at $R_{\Omega,c} = 0$ has a flat central part with approximately zero velocity, and with higher velocities close to the cylinder walls [33]. The regions close to the cylinder walls are expected to have higher azimuthal velocities due to the no-slip wall conditions. The size of the central part increases with Reynolds number, due to the increasing Reynolds number imposing a thinner boundary layer, hence stronger gradients near the wall [33]. However, asymmetry of the azimuthal velocity profile was also reported in the literature [33].

Tracking of coherent structures can be performed in different flow types. However, due to the slow convection velocities and therefore

longer observation times, wall-bounded flows such as boundary layer, channel flow or plane Couette flow, are preferred. The first two flow types are incapable of having a convection velocity close to zero. Therefore the tracking time for those cases are relatively short compared to Couette or Taylor-Couette flow in a finite-size measurement domain. On the other hand, a recent approach for extended observation times in turbulent boundary layer flow is used by Gao et al. [46]. They implemented a moving tomographic PIV system, where they moved the camera and the laser system together with the flow to track the flow structures and to study their evolution. Even though it is a very promising method and applicable to different flow types, compared to conventional (i.e. steady) high-speed tomographic PIV, the experimental setup is more complicated to build. Furthermore, the maximum achievable flow speed is limited to the traversing speed of the tomographic PIV system for mechanical reasons [46]. They reported the maximum traversing velocity as 1 m/s for their system.

On the other hand, in plane Couette and Taylor-Couette flow it is possible to create flow conditions with approximately zero convection velocity. This principle has been utilized by Dauchot and Daviaud [24], where they used it at plane Couette flow facility. They created turbulent spots with injection in order to visually investigate characteristics and evolution of the turbulent spot under condition of zero mean convection velocity. Recently, Suryadi et al. [99] studied evolution of transitional flow structures, using rotating plane Couette flow. To the authors knowledge, these works have been the only tracking studies performed under similar flow conditions.

4.2.1 Duration of observation

The observation (or the tracking) duration of a structure can be defined as the timespan t^* over which we can follow a coherent structure convecting through the measurement domain. It can be computed using a simple formula

$$t^* = \frac{L}{U_C}, \tag{4.1}$$

where L and U_C are representing the length of the measurement domain in the flow direction and the convection velocity, respectively.

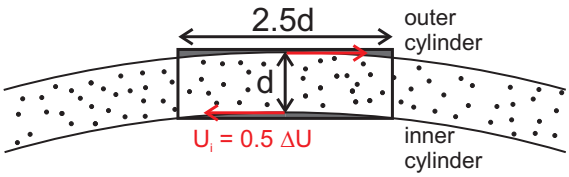

Figure 4.2: Sketch of the Taylor-Couette gap showing the variables used for the computation of the observation time.

In the case of a boundary layer, it can be assumed that the width of a typical measurement domain in the free-stream direction would be approximately twice the boundary layer thickness δ, therefore $L \cong 2\delta$. Actually this assumption is based on some of the values in the literature. For instance, Schroder et al. [92] used $L = 1.65\delta$. In the outer layer of a turbulent boundary layer with a freestream velocity U_e, the macroscopic length and velocity scale are δ and u' ($\approx 1/20U_e$), respectively. The observation time for boundary layers expressed in the turbulent macroscales thus becomes

$$t^*_{TBL} = \frac{2\delta}{U_e} = \frac{2\delta}{20u'} = 0.1\frac{\delta}{u'}. \tag{4.2}$$

In current study, the velocity difference between the walls is $\Delta U = U_i - U_o$. Since the cylinders are rotating in the opposite direction with equal wall velocities ($U_i = -U_o$), the mean velocity in the bulk is approximately zero. Therefore the convection velocity U_c can be assumed to be dominated by u'. The macroscopic length scale is the gap width d. In the present case the size of the measurement volume is approximately $2.5d$ in the azimuthal direction (see Figure 4.2). The observation time for turbulent Taylor-Couette flow is then approximated by

$$t^*_{TC} = \frac{2.5d}{u'}. \tag{4.3}$$

Using the simple calculations above, it can be assumed that the typical observation time in current study is one order of magnitude higher

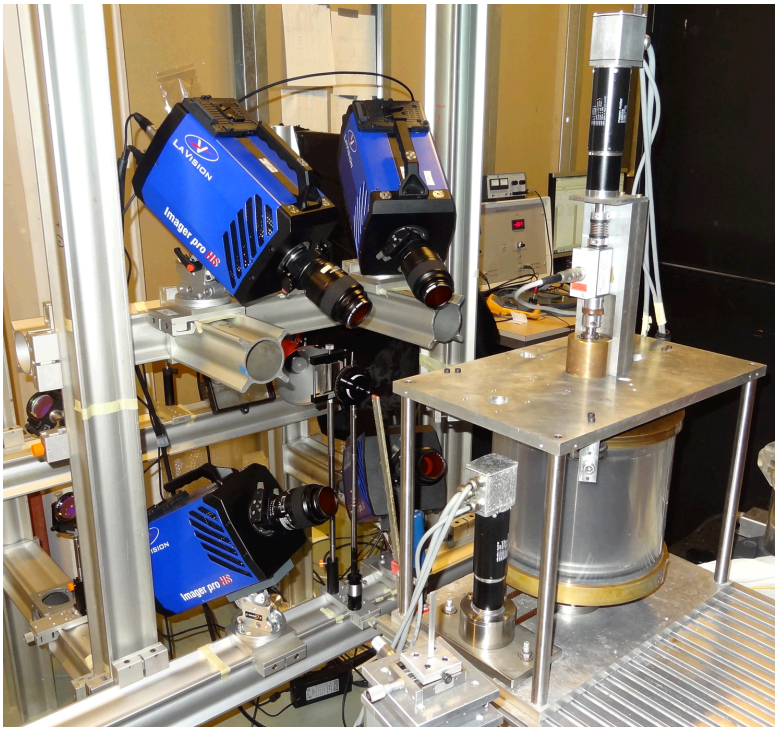

Figure 4.3: Experimental setup with high-speed cameras.

than the observation time for typical boundary layer experiments and larger than a large-scale eddy turnover time δ/u'.

4.3 Experimental Setup

The Taylor-Couette setup used in this chapter is identical to the one described in previous chapters (Chapter 2 and 3, Table 2.1) with slight modifications to the imaging system with the purpose of performing time-resolved measurements. The most significant differences are the implementation of CMOS high-speed cameras (Figure 4.3) instead of CCD cameras used before, and a laser with higher repetition rate to match the recording rate of the CMOS cameras. The modifications are detailed in the following subsections. Further details on the experimental setup can be found in Chapter 2.

4.3.1 Image acquisition

Four Imager PRO HS 4M cameras with a resolution of 2016×2016 pixels are used for image acquisition. The size of a single pixel is $11 \times 11 \mu m^2$, which is larger than those of the previously used cameras (Chapters 2 and 3). The maximum recording speed at this resolution is 1279 fps (frames per second). However, only an area of 860×1400 pixels are utilized. This increased the number of the recorded images per time serie as the camera memory was fixed. The images are recorded with 437 fps. At the current recording rate the target particle image displacement between two frames is 10 pixels. The dimensions of the reconstructed volume are approximately $46.5 \times 25 \times 10$ mm in the axial, azimuthal and radial directions, respectively. Objectives with a $f = 105$ mm focal length and $f/8$ aperture are used during the image acquisition, which are mounted on Scheimpflug adapters. The cameras are arranged in a rectangular configuration (Figure 4.3). The angle between the cameras are approximately 23 and 44 degrees in the horizontal (azimuthal) and vertical (axial) directions, respectively. Time-series of $10,000$ images were recorded, which corresponds to 22.9 s. The calibration of the tomographic PIV is done using the procedure that was explained previously (Section 2.5.4).

In accordance with previous experience (see Chapter 3), the spatial resolution is adjusted to be able to capture the smallest flow structures. The Kolmogorov length scale is $\lambda_K = 0.12$ mm at $Re_S = 3500$. The ratio between the vector spacing at 75% interrogation volume overlap (δ_X) to Kolmogorov length scale ratio is adjusted to be $\delta_X/\lambda_K = 2.6$ (equivalent to interrogation window size $D_I/\lambda_K = 10.4$ at 75% overlap), which is sufficient to resolve all scales in the flow [18,54,85,122]. At the current Re_S, the Kolmogorov time scale ($\tau = (\nu/\epsilon)^{1/2}$) is 16.08 ms. If it is compared to the recording rate ($\Delta t = 1/437 = 2.29$ ms), the sampling rate is high enough to temporally resolve the motions of the coherent structures and track them through the measurement volume.

4.3.2 Illumination and flow seeding

The illumination and the flow seeding applied in this chapter is similar to Chapter 2, with the exception of the laser. A Nd:YLF laser (Litron LDY304-PIV), that emits light with a wavelength of 532 nm and with

34 mJ/pulse energy at 437 Hz, is used to illuminate the volume for time-resolved measurements. The cross-section of the laser beam is extended to the required value using two cylindrical-planar lenses ($f = -90$mm and -12.5 mm). Fluorescent (Fluostar [56]) particles and 570 nm low-pass optical filters are implemented to reduce the effect of the background (see Figure 2.4). The fluorescent tracer particles absorb green light of the laser and emit fluorescent light at wavelength of 580 nm. The mean diameter of the particles is 15 μm and the particles have a density of 1.1 g/cm^3 [56]. During the experiments the seeding density is kept around 0.02 particles per pixel (ppp). For further details on the flow seeding and the illumination please refer to Sections 2.5.2 and 2.5.3.

4.3.3 Image processing and vector validation

In order to increase the image quality, a sliding minimum intensity over 25×25 pixels was subtracted. Then 3×3 pixels Gaussian smoothing was applied to the images [37,120]. Similar to the previous chapters, the adaptive multi-pass approach was used for correlation with $40 \times 40 \times 40$ voxels and 75% overlap in the final two passes. Spurious vectors were detected and removed by the universal outlier detection method, with a threshold value of 2, which can be considered as "universal" [117]. Linear interpolation was used to fill the gaps where the vectors were removed. The final measurement volume contains $145 \times 78 \times 34$ vectors in the axial, azimuthal and radial directions, respectively. For further details of the seeding of the flow, illumination, calibration and image processing please refer to Chapter 2.

4.4 Results

In this section initially the assessment of the measurement accuracy is discussed. Then the results for the mean flow is given. It is followed by the initial observations on dynamical aspect of the flow, such as the azimuthal velocity bursts and stretch and break-up events of turbulent flow structures. The results are presented as an overview to show the capacity of the measurement technique, rather than details, and mostly focus on the qualitative aspects.

4.4.1 Assessment of the measurement accuracy

The accuracy of high-speed tomographic PIV measurements can be investigated using one of the basic principles of the fluid dynamics; conservation of mass [5, 87]. For an incompressible flow, the divergence of the flow velocity should be zero everywhere in the measurement domain ($\nabla \cdot \vec{V} = 0$). In Cartesian coordinates the divergence is

$$\nabla \cdot \vec{V} = \frac{\partial u}{\partial x} + \frac{\partial v}{\partial y} + \frac{\partial w}{\partial z} = 0. \tag{4.4}$$

In the case of fully volumetric measurements, all gradients in equation 4.4 are known for each data point, and the relative error distribution can be computed using the expression [5, 57, 58]

$$\overline{\left(\frac{\partial u}{\partial x} + \frac{\partial v}{\partial y} + \frac{\partial w}{\partial z}\right)^2} \cong C \left(\frac{\sigma_{\Delta X}}{D_I \Delta t}\right)^2, \tag{4.5}$$

where $\sigma_{\Delta X}$ is the overall particle displacement error amplitude, D_I is the size of the interrogation windows (that is 40 pixels), Δt is the time between two frames ($\Delta t = 2.288$ ms) and C is a constant that is depending on the differentiation scheme [5,57,58]. However, in the literature, C is not defined for the differentiation with second order regression analysis. In order to estimate C for this chapter, simulations are performed using synthetic velocity field. The results show that if 75% overlap and second order regression analysis are used for computations, $C = 4.54$ can be applied in equation 4.5.

Figure 4.4 shows the distribution of the divergence values computed over 10000 vector fields. The width of the distribution is indicative of the measurement accuracy [5, 87]. The standard deviation of the fitted Gaussian distribution to Figure 4.4 is 0.012, which is of the order of previous studies [5, 31, 57, 88, 89]. It is found using equation 4.5 that $\sigma_{\Delta X} = 0.24$ pixels, which is in agreement with values reported in the literature [5, 57, 58].

Another way to investigate the measurement quality is the scatter plot of $-(\partial u/\partial x)$ versus $(\partial v/\partial y + \partial w/\partial z)$, where ideally the data should be along the 45° diagonal line representing zero divergence [5, 64, 122, 123]. The length of the distribution along the diagonal represents the

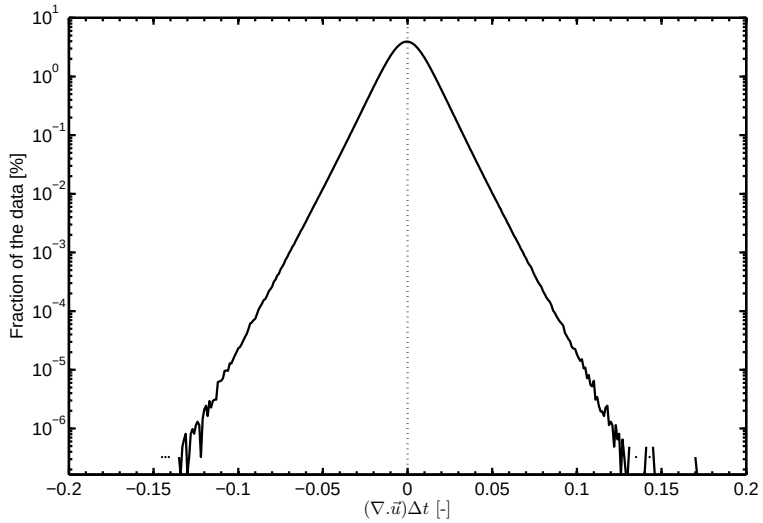

Figure 4.4: Histogram of the divergence error, represented by the distribution of the divergence values.

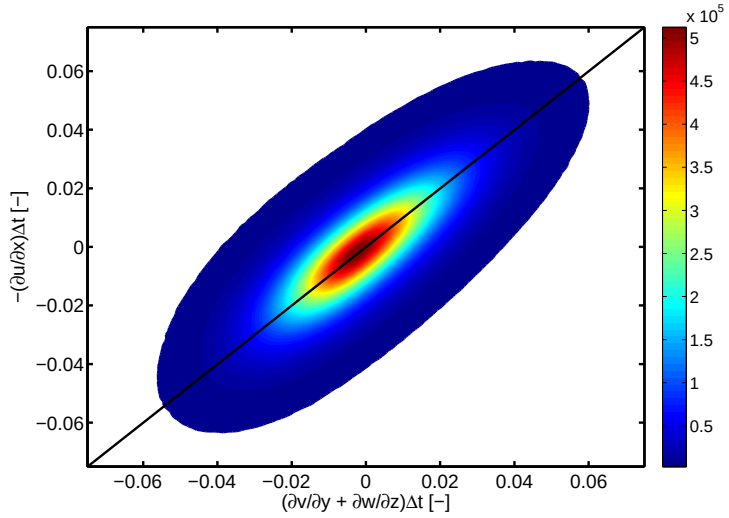

Figure 4.5: Joint PDF of $(\partial v/\partial y + \partial w/\partial z)\Delta t$ versus $-(\partial u/\partial x)\Delta t$, computed at each vector location for full data set (10000 vector fields). The contours represent the number of samples. Diagonal line represents the divergence free ($\nabla \cdot \vec{V} = 0$) condition.

range of the measured gradients, while the width of the distribution (in the direction normal to the diagonal line) is indicative of the noise level. Therefore the dynamic range in the measured gradients can be inferred [5]. Figure 4.5 shows the results for current data set, which is nicely elongated over the diagonal line. The ellipsoid aspect ratio of the scatter plot is $\approx 1/2.61$, which is of the order of similar studies [64].

4.4.2 Mean flow

The temporal mean of the azimuthal velocity component along the radial gap is shown in Figure 4.6. The azimuthal velocities are normalized with the actual velocity of the inner cylinder ($U_i = 0.158$ m/s). The measured velocities very close to the cylinder walls show that the velocity of the inner cylinder is underestimated by 11%. In the case of the outer cylinder, the underestimation increase to 16%. On the other hand, the maximum axial and the radial velocities are 0.6% and 0.9% of the azimuthal velocity, respectively. It should be mentioned that the discrepancy of the wall velocities is also partly due to the uncertainty of the control of the rotation speeds of the cylinders. Although the rotation speeds are independently checked with a light gate and a stroboscope, still the precision of the cylinder rotation frequency is at the order of 10^{-2} Hz. At the current rotation speeds of the cylinders, this introduces approximately 4% uncertainty to the wall velocities ($U_i = 0.158 \pm 0.006$ m/s). However, the velocities on the wall are omitted in Figure 4.6.

As it is seen in Figure 4.6 the azimuthal velocity in the bulk is close to, but not exactly zero. The mean azimuthal velocities remain within $U/U_i = 0 \pm 0.05$ in the range of $0.46 \leq (r - r_i)/d \leq 0.68$ and $U/U_i = 0 \pm 0.15$ in the range of $0.27 \leq (r - r_i)/d \leq 0.79$. The flat central part of the profile (dashed-dotted line in Figure 4.6) has a slope of $\approx 24^\circ$ ($\partial U_i/\partial r = 7.1$ s^{-1}) with the wall normals. On the other hand, the upward shift of the velocity profile shows the general advancing direction of the structures, such that for the most of the central part of the gap, there is a non-zero mean velocity in the direction of the inner cylinder rotation. Actually, investigation of the time resolved 3D velocity fields confirm this observation; the turbulent flow structures in the gap are found to be mostly advancing in the direction of the inner cylinder rotation (Figure 4.7). Furthermore, the advancing behaviour of a structure depends on its actual radial location, as well. In general, in the region

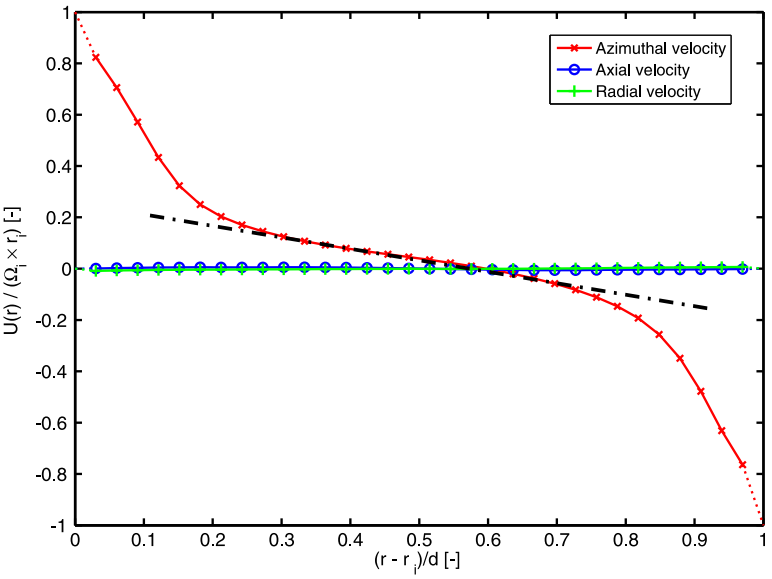

Figure 4.6: Mean velocities as a function of the radial position. The velocities are averaged over 10000 vector fields and spatially averaged in the axial direction. The velocities are non-dimensionalised with the inner cylinder velocity. Dashed-dotted line is the reference line to show the inclination of the profile.

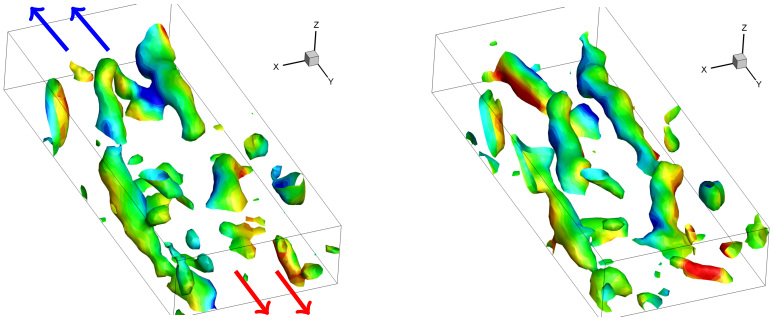

(a) $\Delta t = 0$ ms (b) $\Delta t = 43$ ms

Figure 4.7: Advancing vortical structures represented by Q criterion isosurfaces. The radial velocity is color coded. The red and blue arrows indicate the rotation direction of the inner and the outer cylinders, respectively.

where there is a positive azimuthal velocity ($0.0 < (r - r_i)/d \leq 0.58$), the structures are mostly moving in the direction of the inner cylinder rotation. In the remaining part of the gap ($0.58 \leq (r - r_i)/d < 1.0$) the structures are moving in the opposite direction. Naturally, this observation is very general, therefore it does not hold for extreme events such as the azimuthal velocity bursts (see Section 4.4.3).

Figure 4.6 also reveals the so-called "zero crossing", where the azimuthal velocity changes from positive to negative. This can be considered as a neutral surface (a virtual cylindrical surface with zero azimuthal velocity) separating the inner and outer part of the Taylor-Couette gap [16, 36]. The location of this neutral surface might change the stability and torque characteristics of the Taylor-Couette flow, even causing a smaller effective gap width [16,36]. It should be mentioned that the zero crossing is gap ratio and Reynolds number dependent [33, 36]. In current case the velocities reach zero at $(r - r_i)/d \approx 0.58$. Dong [33] reported the zero crossing around $(r - r_i)/d \approx 0.53$ at $Re_S = 3000$ with a gap ratio of $\eta = 0.5$. Any possible influence of the location of the neutral surface to the flow characteristics should be further investigated.

The mean azimuthal velocity profile also shows the presence of the higher velocity gradients close to both walls, which gives an idea of the thickness's of the inner wall regions on cylinder walls. The inner wall region close to the inner cylinder ($\delta_i \approx 0.23d$) is slightly thicker than the one close to the outer cylinder wall ($\delta_o \approx 0.20d$). This might indicate that the characteristics of the inner wall regions are different for the inner and the outer cylinders.

4.4.3 Azimuthal velocity bursts in the radial direction

In addition to the mean flow properties, instantaneous flow fields are also investigated to detect dynamical events. Inspection of the instantaneous azimuthal velocity profiles shows the presence of a velocity burst in the radial direction. The bursting events can be explained as the sudden increase of the (positive or negative) azimuthal velocities at a specific location. If it is visualised by means of azimuthal velocity isosurfaces, the bursts can be seen as a shift of isosurfaces in the radial direction (see Figure 4.8, where examples of intense bursts are also indicated by green arrows). Due to this shift, the "zero crossing" moves radially during the bursting events. In the given example, the area under dominance of the

inner cylinder (i.e. with positive azimuthal velocity) suddenly extends radially in the gap (Figure 4.8(a) and 4.8(b)), causing a retraction of the region under the dominance of the outer cylinder (i.e. with negative azimuthal velocity) in the bulk of the flow. The flow changes in such a way that instantaneously the effective radius of the inner cylinder is expanded towards the outer cylinder and the neutral surface is shifted closer to the outer cylinder. Then, another burst coming from the outer cylinder region (i.e. with negative azimuthal velocity) follows and surpasses the region affected by the inner cylinder in the radial gap (Figure 4.8(c)). These "alternating bursts" event continue to oscillate until the flow reaches its initial state as shown in Figure 4.8(d). The bursts are observed several times in the current data set, but the occurrence of the burst is found to be random in time. Additionally the frequency and the duration of each bursting event appear different and seem to be random, as well. If it is assumed that the convection velocity of the features shown in Figure 4.8 are equal to the velocity of the shown isosurfaces ($U_C = 0.3U_i$), they convect 0.013 m ($= 1.3d$) over $\Delta t = 274.5$ ms. Therefore it can be said that shown features are dynamic events that are not convected in or out of the measurement volume during the period of the observation.

One could hypothesize that these bursts can be due to non-ideal aspects of the cylinders (such as wobbling or deformation) during the measurements. In order to test this an additional analysis was performed. The reconstructed intensity profile in the radial direction (depth direction in the camera coordinate system) defines the location of the measurement volume [42, 43, 72], i.e. the volume containing the illuminated tracer particles. Since the particles cannot penetrate the cylinder walls in current case, and the whole cylinder gap is illuminated, the intensity profile should not move in the radial direction over time. Intensity distribution of the reconstructed volume in the radial direction is plotted as a function of time in Figure 4.9, using 300 reconstructed volumes (≈ 0.67 s). Using the velocity fields, at least 2 bursting events are detected during this time. If this is due to the wobbling of the cylinders, this should be observed as a horizontal shift in Figure 4.9. However, the intensity distribution showed that during these two burst events, the maximum displacement of the borders of the reconstructed volume is at most 8 voxels (≈ 0.22 mm). Considering the fact that the size of the reconstructed volume in the radial direction is 355 voxels, the

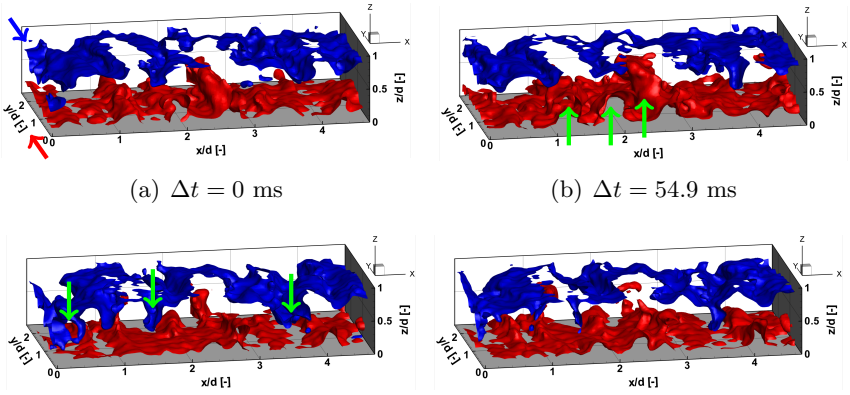

(a) $\Delta t = 0$ ms (b) $\Delta t = 54.9$ ms

(c) $\Delta t = 219.6$ ms (d) $\Delta t = 274.5$ ms

Figure 4.8: Azimuthal velocity bursts. The isosurfaces represent the positive and negative azimuthal velocities; red = $0.3U_i$, blue = $0.3U_o$. The green arrows indicate the axial location and the radial direction of the examples of the intense burst events. The x, y and z axes are representing the axial, azimuthal and radial directions, respectively. The red and blue arrows indicate the rotation direction of the inner and the outer cylinders, respectively.

change of 8 voxels is equal to 2.3% change, which can simply be associated with the slight intensity change of the particles or fluctuation of the laser power. Furthermore, the radial displacement of the isosurfaces shown in Figure 4.8 is around 45 voxels, which is significantly higher than the observed border displacement of 8 voxels. Therefore, it can be concluded that these bursts are not due to this kind of non-ideal aspect of the experimental setup, and are physical events.

4.4.4 Vortical structures and stretch & break-up events

In fully turbulent Taylor-Couette flow at $Re_S = 3500$, the most common instantaneous vortical structure that was found is the tube-like structure that is elongated in the azimuthal direction (Figure 4.10). Examples of other coherent motions such as hairpins are present in the flow, as well. But in correspondence to the results in the literature [32, 33], the tube-like structures that are elongated in the azimuthal direction are

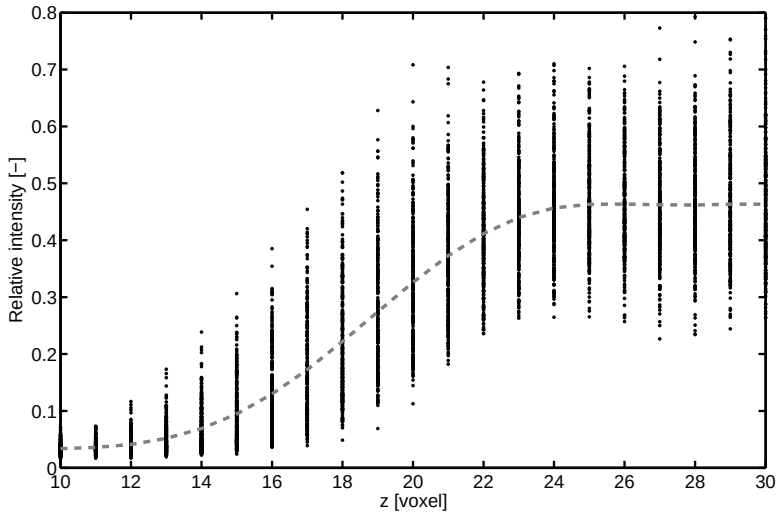

Figure 4.9: Intensity profiles of 300 instantaneous reconstructed volumes along the radial direction (z). Only the part close to the inner cylinder, which is located at $z = 5$ voxel units, is shown. The dashed line shows the mean intensity over 300 reconstructed volumes. The intensities are normalized with the maximum intensity of 300 reconstructed volumes.

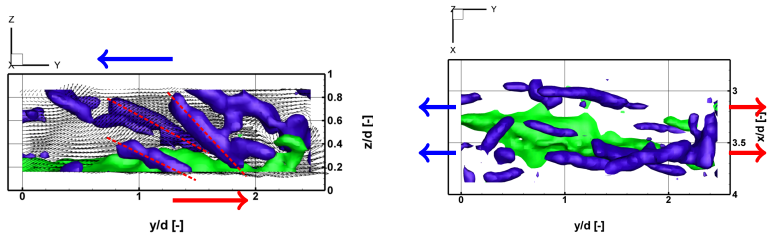

(a) azimuthal-radial view (b) azimuthal-axial view

Figure 4.10: Example of typical turbulent flow structures. Isosurfaces are $Q = 400$ s^{-2} (blue), and azimuthal velocity $U = 0.5U_i = 0.079$ m/s (green). The red and blue arrows indicate the rotation direction of the inner and the outer cylinders, respectively.

by far the most common structures. It is known that these large-scale motions contribute mostly to the turbulent kinetic energy [2, 4, 83, 97] (also see Chapter 5). In the specific examples given here these structures are mostly accumulated around the velocity streaks. They appear as counter-rotating pairs as reported in the literature [33,111], and typically are inclined with respect to the cylinder walls (represented by dashed red lines in Figure 4.10(a)) within the range $25^\circ \leq \alpha \leq 47^\circ$, which was also observed in fully turbulent Taylor-Couette flow [32, 33], as well as in the boundary layer flows [4, 38, 92].

Due to the long observation time it is possible to examine their evolution, which involves stretching and the break-up. It is proposed that in wall-bounded flows vortex stretching might be an important mechanism that is responsible for the transfer of turbulent kinetic energy between different scales [2, 33, 79, 103]. In the current case, stretching is observed especially for the azimuthally-aligned tube-like structures. They are mostly found to be stretched from both ends. The structures break-up in to several smaller structures during stretching. Following the break-up, the (new) smaller structures either disappear or start to be stretched by a similar process.

An example of this process is given in Figure 4.11. Initially the vortical structure is advected in the direction of the inner cylinder rotation (positive y). The advancing slows down to a convection velocity very close to zero (Figure 4.11(a)). Then the structure starts to be stretched in the azimuthal direction (Figure 4.11(b)). The stretching continues and the structure becomes approximately 3 times longer than its initial length (Figure 4.11(c)). Another vortical structure (aligned in the axial direction) approaches the stretched vortex (Figure 4.11(d)) and causes it to breakup into two azimuthally-aligned structures (Figure 4.11(e)). The axially-aligned vortical structure in this specific example is found to be associated with an axial-velocity streak close to the outer cylinder. Figure 4.11(f) shows two new structures after the break-up. Both are comparable in length with each other as well as with the initial length of their "parent" structure. Similarly, they are also aligned in the azimuthal direction and inclined with respect to the cylinder walls. One of these structures disappears in a short time (approximately 118.98 ms after the break-up), whereas the other one goes into a stretching process similar to the one explained here. Please note that the process explained here is one of possibly many events, and the explanation is only valid for

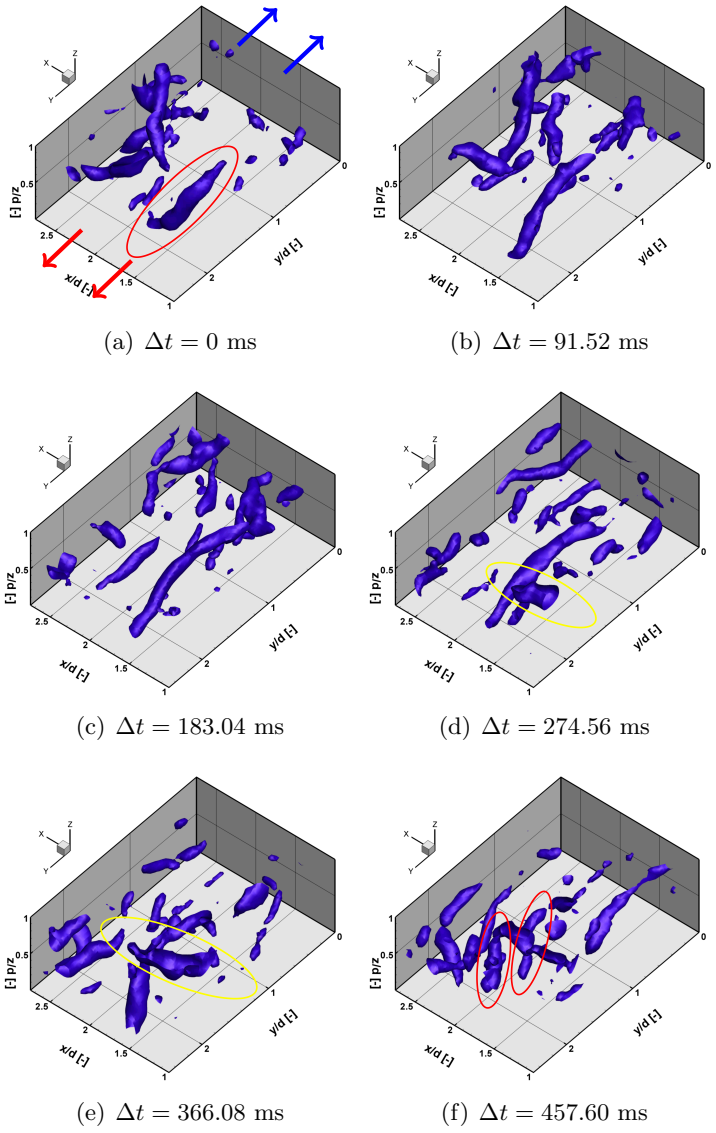

(a) $\Delta t = 0$ ms (b) $\Delta t = 91.52$ ms

(c) $\Delta t = 183.04$ ms (d) $\Delta t = 274.56$ ms

(e) $\Delta t = 366.08$ ms (f) $\Delta t = 457.60$ ms

Figure 4.11: Example of stretch and break-up. Isosurfaces are $Q = 550$ s^{-2}. Intermediate time steps are skipped for better visibility. The red and blue arrows indicate the rotation direction of the inner and the outer cylinders, respectively.

this specific example. Further statistical analysis is required for a more general understanding of the break-up mechanism.

4.5 Conclusions

In this chapter, time-resolved tomographic PIV was implemented to the Taylor-Couette flow with approximately zero mean velocity. This configuration allowed longer observation time compared to similar experimental studies in wall-bounded flows. It allows for unique insight into the evolution of the turbulent flow structures. Examples of some dynamic events were given to illustrate the newly acquired capabilities and demonstrate its potential for turbulence research.

Despite the approximately zero mean velocity in the bulk, most structures convect slowly in the azimuthal direction. The convection direction and velocity of a coherent structure depends on its radial position. In accordance with the slight shift of the mean velocity profile towards the inner cylinder rotation, most of the structures in the bulk convect in the direction of the inner cylinder rotation. The mean azimuthal velocity profile also shows that the thickness of the inner wall region is slightly different for the inner and the outer cylinders.

Several dynamic events are observed at fully turbulent Taylor-Couette flow. One of them is the azimuthal velocity burst, which can be explained as the instances of sudden increase of the positive or the negative azimuthal velocities. This results in a shift of the velocity isosurfaces in the radial direction, which change the effective radii of the cylinders in the gap. Bursts appear in alternating patterns; positive and negative velocity bursts follow each other. However, the bursting events appear random in time.

Various kinds of instantaneous vortical structures are present in the flow. However, the most common structure type appears to be the tube-like vortex that is elongated in the azimuthal direction. These are frequently located in association with the velocity streaks and inclined with respect to the cylinder walls. Events of stretching and break-up of these structures were revealed using the time resolved measurements. In the future, this research can be extended to higher Reynolds numbers as well as other rotation rates, with more detailed quantitative analysis on the observed events.

5 Change of Coherent Turbulent Flow Structures at Counter-Rotating Taylor-Couette Flow

5.1 Introduction

Taylor-Couette is a canonical flow geometry to study transport of momentum in turbulence, where the stresses due to turbulence can be measured directly through the torque on the cylinder axes. Studies on torque scaling in Taylor-Couette flow [16, 36, 76, 109, 110] reported a significant change of torque values for different rotation rates of the cylinders. The limited number of studies that focused on the relation between turbulent flow structures and the torque scaling [33, 82] could not fully explain the mechanism that is responsible for this change. Even though coherent flow structures at different flow regimes in Taylor-Couette flow were qualitatively studied in the literature [7], they are limited to low Reynolds numbers ($Re_S \leq 6500$). The studies at turbulent flow are performed at relatively higher Reynolds numbers and mostly focused on angular momentum transport [16, 36, 76, 109, 110], while only few studies focused on both the turbulent flow structures and the angular momentum transport [33, 82, 111].

In this chapter, the observations on large-scale flow structures are reported to reveal the transition of the large scale turbulent flow structures from Taylor vortices to inclined vortices, then to structures similar to Taylor columns at fully turbulent counter-rotating Taylor-Couette flow. The results reveal new flow states compared to what was assumed before, in particular the presence of structures similar to Taylor columns that are observed for the first time in Taylor-Couette flow. The observed structural change is used to explain the change of torque with the ro-

Based on S. Tokgoz, G. E. Elsinga, R. Delfos, J. Westerweel *Large scale structures and Taylor columns in Taylor-Couette flow.* Submitted to Physical Review Letters

tation number, where inclined vortices are found to enhance angular momentum transfer rather than Taylor vortices.

The scaling of torque with Reynolds number is discussed in detail by Eckhardt et al. [36] for only outer cylinder rotation, which also describes the similarity between Rayleigh-Bénard and Taylor-Couette turbulence. Based on that work, recent turbulence studies in Taylor-Couette flow are performed at relatively higher Reynolds numbers around 10^5-10^6 [16,76, 109,110], which showed the presence of an optimum angular momentum transport at slightly negative rotation numbers defined as $R_\Omega = (1-\eta)(Re_i + Re_o)/(\eta Re_o - Re_i)$, where η is the gap ratio ($\eta = r_i/r_o$, with r_i and r_o are the inner and outer cylinder radii, respectively), and Re_i ($= r_i\Omega_i d/\nu$) and Re_o ($= r_o\Omega_o d/\nu$) are the Reynolds number for the inner cylinder and the outer cylinder, respectively. They showed the optimum angular momentum transport depends on the gap ratio and moves closer to exact counter-rotation for $\eta \to 1$ [16, 109, 110]. Van Gils et al. [109] provided an expression that summarises the optimal transport in their experiments, although the principal mechanism for the optimal transport is not provided. Following their method [109] and using the torque measurements performed by Ravelet et al. [82], it is found that the optimal transport occurs at $R_\Omega \approx -0.025$ in current flow facility. To further explore the optimum transport, detailed data and the instantaneous flow fields are required, which are presented in this chapter.

Similarly Ravelet et al. [82] determined (see Figure 5.1) the friction factor C_f ($= T/2\pi\rho r_i^2 L U_{sh}^2$) as a function of R_Ω for several shear Reynolds numbers $Re_S (= (2\,|\eta Re_o - Re_i|)/(1+\eta))$ [35]. They reported that for $29000 \leq Re_S \leq 47000$, C_f remains almost constant up to slightly negative $R_\Omega = -0.035$. After that point C_f decreases, reaching approximately half of its initial value at $R_{\Omega,o}$. In addition to this, they reported an initially decreasing trend till $R_\Omega = -0.05$ for lower Re_S ($11000 \leq Re_S \leq 17000$). They also observed a change of coherent flow structures in such a way that the flow is dominated by large-scale structures for $R_\Omega < 0$ and by small-scale structures for $R_\Omega > 0$. They proposed that this variation might be responsible for the change of the torque at constant shear.

To characterize the angular momentum transport, rather than the mean flow, the instantaneous turbulent flow structures should be considered. In this chapter the instantaneous large-scale turbulent struc-

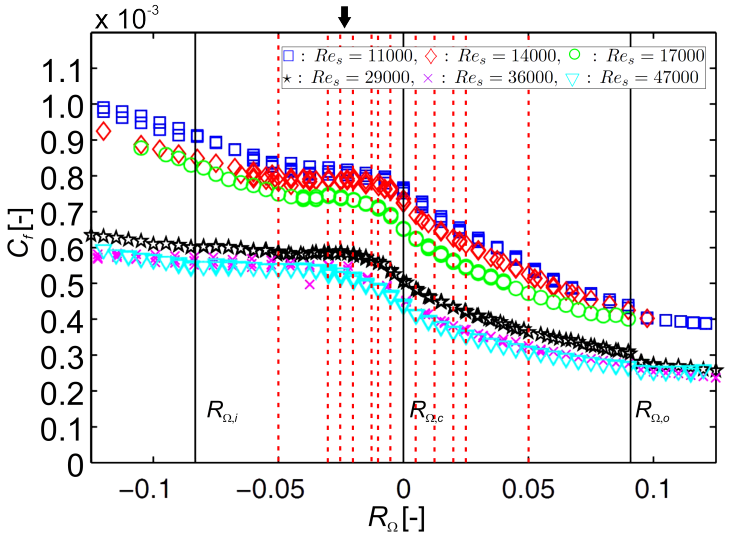

Figure 5.1: Friction factor C_f as a function of R_Ω, redrawn after Ravelet et al. [82]. Dashed red lines represent the measurement points where the tomographic PIV was obtained in addition to the black lines showing $R_{\Omega,i} = -0.083$, $R_{\Omega,c} = 0$ and $R_{\Omega,o} = 0.091$. A black arrow indicates the location ($R_\Omega \approx -0.025$) of the optimum angular momentum transfer for current setup.

tures (ILS) are considered in connection to their contribution to angular momentum transport and therefore to the torque, using tomographic particle image velocimetry (tomographic PIV) [42] in Taylor-Couette flow. The dependence of the ILS organisation on the relative rotational speeds of the cylinders (i.e. R_Ω) at constant shear rates ($Re_S = const.$) are investigated. The ILS are separated from instantaneous smaller-scale turbulent structures (ISS). This enables the isolation of the ILS and ISS and their contribution to angular momentum transport. It should be noted that in this chapter "smaller-scale structures" are defined as the range of scales between the smallest resolved scale and the filtered length scale, and it should not be confused with the conventional "small scales" such as Kolmogorov or Taylor microscales.

5.2 Experimental Setup

The Taylor-Couette geometry used in this chapter is identical to the one described in previous chapters (see Chapter 2 and Table 2.1 for more details). Similarly, tomographic PIV measurements are performed to measure all velocity components in a volume of $40 \times 20 \times 10$ mm^3 in the axial, azimuthal and the radial directions, respectively. Although all other components and configurations of tomographic PIV setup are the same as Chapter 2, the cameras used in current chapter are different. The cameras that were used in Chapter 3 (i.e. Imager Pro X 4M) are used in current chapter, as well. Four cameras are arranged in rectangular configuration, recording PIV images at a rate of 7.55 Hz. The flow is seeded with fluorescent particles of $15\mu m$ diameter, which are illuminated by a Nd:YAG laser with 50 mJ/pulse energy at a wavelength of 532 nm. Further detailed information about the experimental setup, the implementation of tomographic PIV to Taylor-Couette, image acquisition, particles, vector calculation and validation can be found in Chapter 2.

The flow is investigated at three Re_S, that is $Re_S = 11000, 29000$ and 47000. Corresponding Taylor numbers (Ta) [36] are of the order of 1.3×10^8, 8.5×10^8 and 2.2×10^9, with respect to the corresponding Re_S. The rotation number [35] is selected to be the parameter to be varied between $R_{\Omega,i} = -0.083$ (only inner cylinder rotates) and $R_{\Omega,o} = 0.091$ (only outer cylinder rotates), where $R_{\Omega,c} = 0$ represents exact counter rotation of the cylinders. The Rossby number ($Ro = (\Omega_i - \Omega_o)/\Omega_o$) [76] is in $-\infty < Ro \leq -1$ range. The flow conditions are specified in Table 5.1.

Please note the different coordinate system and naming followed in this chapter. As mentioned previously (see Section 2.5.1), the tomographic PIV measurements were performed in a Cartesian coordinate system. However, the velocities and the axes are converted to cylindrical coordinate system for the current chapter. The azimuthal, radial and the axial directions are given by θ, r and z, respectively. The velocities in the corresponding directions are represented by their indices, such as u_θ, u_r and u_z.

Table 5.1: Flow conditions.

R_Ω	$Re_S = 11000$				$Re_S = 29000$				$Re_S = 47000$			
[-]	Re_i [-]	Re_o [-]	Ω_i [rad/s]	Ω_o [rad/s]	Re_i [-]	Re_o [-]	Ω_i [rad/s]	Ω_o [rad/s]	Re_i [-]	Re_o [-]	Ω_i [rad/s]	Ω_o [rad/s]
-0.083	-10543	0	-9.73	0	-27796	0	-25.38	0	-45049	0	-41.15	0
-0.050	-8538	2137	-7.92	1.88	-22510	5765	-20.29	4.78	-36482	9343	-32.92	7.73
-0.030	-7323	3512	-6.79	2.95	-19306	9259	-17.22	7.54	-31289	15006	-27.90	12.25
-0.025	-7019	3843	-6.47	3.27	-18505	10133	-16.71	8.36	-29991	16422	-26.77	13.45
-0.020	-6715	4175	-6.22	3.52	-17704	11006	-15.77	8.98	-28693	17837	-25.26	14.39
-0.0125	-6260	4672	-5.78	3.96	-16502	12316	-14.70	10.05	-26745	19961	-23.56	16.15
-0.010	-6108	4837	-5.65	4.08	-16102	12753	-14.20	10.30	-26096	20669	-22.68	16.46
-0.005	-5804	5169	-5.34	4.40	-15301	13627	-13.51	10.99	-24798	22084	-21.55	17.59
0.0	-5500	5500	-5.09	4.65	-14500	14500	-12.75	11.69	-23500	23500	-20.42	18.72
0.005	-5196	5831	-4.78	4.96	-13699	15373	-12.06	12.44	-22202	24916	-19.29	19.85
0.0125	-4740	6328	-4.40	5.34	-12498	16684	-11.00	13.45	-20255	27039	-17.59	21.55
0.020	-4285	6825	-3.96	5.78	-11296	17884	-9.93	14.51	-18307	29163	-15.96	23.25
0.025	-3981	7157	-3.71	6.09	-10495	18867	-9.24	15.21	-17009	30578	-14.83	24.38
0.050	-2462	8813	-2.26	7.48	-6490	23235	-5.72	18.79	-10518	37657	-9.17	30.03
0.091	0	11498	0	9.74	0	30312	0	24.50	0	49127	0	39.21

5.3 Mean Flow

The examination for this chapter begin by averaging the velocity fields over whole data set (200 images for each flow case). The mean velocity fields showed a significant rotation number dependence. In the case of only inner cylinder rotation ($R_{\Omega,i} = -0.083$) the flow is well organized for all Re_S (Figure 5.2(a)). The velocity fields show typical characteristics of Taylor-vortex flow; all velocities are axial-position dependent, and clear regions of in- and outflow are present. Confirming this, the vortical structures in the mean flow are resembling the Taylor vortices (Figure 5.3). They are appearing in counter-rotating pairs with high in- and outward radial velocities in between. This is in agreement with the Taylor vortex-like structures in the mean flow as reported in literature [32, 33, 82, 104, 105]. Their presence was explained by the cumulative effect of the structures with relatively smaller scale.

However, the organisation of the velocity fields, therefore the turbulent flow structures, changes significantly in parallel with the increase of the rotation number. As shown in Figure 5.2(b), in the case of only outer cylinder rotation ($R_{\Omega,o} = 0.091$), the axial dependence of the velocities is lost. The azimuthal velocities are depending on the radial position (also indicating the dominant velocity gradient in the radial direction), where the radial and the axial velocities become very small. In parallel with the velocities, if the rotation number is increased towards the only outer cylinder rotation, the Taylor vortices start to deteriorate as the coherent structures get smaller. After $R_\Omega \geq -0.005$, large scale motions resembling the Taylor vortices are completely disappear from the flow. At positive rotation numbers the chaotic organisation of the relatively smaller structures become dominant in the flow.

5.4 Instantaneous Flow

The results shown by the mean flow indicate that at a constant Reynolds number, the organisation of the turbulent flow structures strongly depends on the relative rotation speeds and the directions of the cylinders. However, in order to understand the real dynamics of this change one needs to investigate the instantaneous velocity fields.

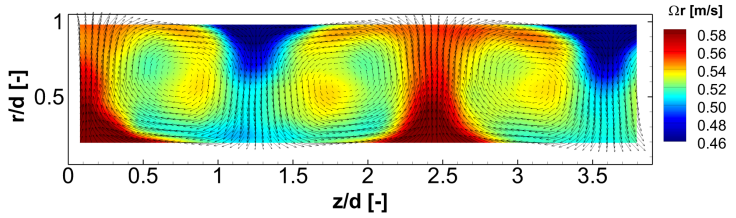

(a) $R_{\Omega,i} = -0.083$

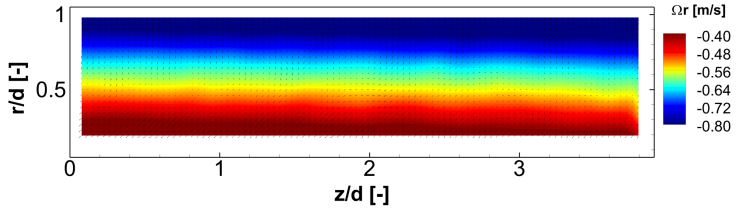

(b) $R_{\Omega,o} = 0.091$

Figure 5.2: Cross-section of the volume showing the mean flow at $Re_S = 29000$. The azimuthal velocities are color coded. Vector arrows indicate the velocities tangential to the cross-section (i.e. axial and radial velocities).

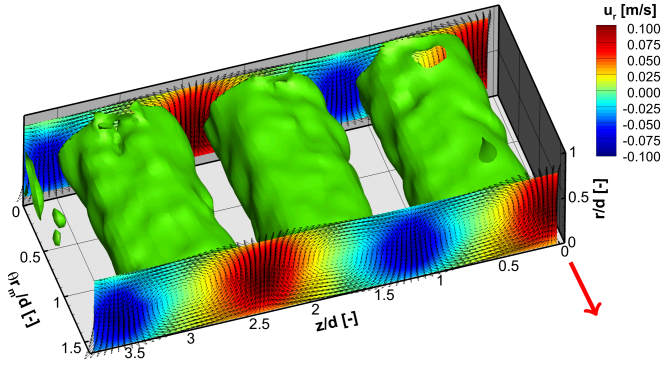

Figure 5.3: Flow structures in the mean flow at $R_{\Omega,i} = -0.083$ and $Re_S = 29000$, represented by the means of Q-criterion [53] isosurfaces ($Q = 175\ \mathrm{s}^{-2}$) (see Figure 5.2(a)). The radial velocities (u_r) are color coded. The red arrow indicates the rotation direction of the inner cylinder, while the outer cylinder remains stationary.

5.4.1 Spatial correlation

Spatial autocorrelation of the fluctuating radial velocities (u_r') in the axial direction is also an indicator of the organisation of the coherent flow structures [33]. If the autocorrelation of the fluctuating radial velocities in the axial direction is computed, the inflow velocities would be negatively correlated with the velocities in the outflow zones, whereas the correlation between an inflow zone with another inflow zone, as well as between an outflow zone with another outflow zone would result in a positive correlation value. This result would be more clear in the case of organised large-scale motions like Taylor vortex flow. In the case of Taylor-vortex flow, since the counter-rotating vortex pairs are separated from each other by an inflow or outflow zone, the autocorrelation peaks and the minimums would be well organised and separated from each other approximately by one Taylor-vortex diameter, where the number of the peaks are determined by the number of the Taylor vortices in the domain.

The autocorrelation of the fluctuating radial velocities in the axial direction are computed for all R_Ω, using 200 vector fields for each case (Figure 5.4 and 5.5). The results confirm the presence of large-scale vortices in the mean flow for $-0.083 \leq R_\Omega \leq -0.005$, as well as their change. As seen in Figure 5.4 and 5.5 the correlation changes significantly for increasing R_Ω, such that the peaks initially located at $\Delta z/d \approx 1.5$ and 2.8 disappear, suggesting the large-scale vortices are no longer present in the flow. The central peak ($\Delta z/d = 0$) reduces in width, indicating the coherent structures reduced in size. These results confirm the observations by Ravelet et al. [82] on the change of the structures.

5.4.2 Instantaneous flow structures

As shown in Figure 5.6, the small scale, high-intensity turbulent flow structures dominate the instantaneous flow for all R_Ω and Re_S that are investigated, confirming earlier findings in the literature [7, 32, 33, 104]. No significant Re_S dependence is observed by flow visualisation.

Even though the instantaneous flow fields are chaotic, there are still some indications of organisation. For instance, close to only inner cylinder rotation (Figure 5.6(a) and 5.6(b)), structures that are larger and slightly more organised than those at the other rotation numbers are

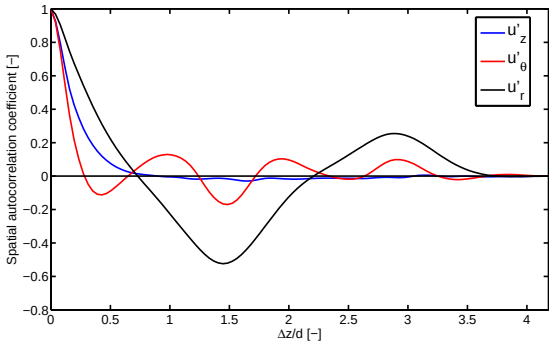

(a) $R_{\Omega,i} = -0.083$

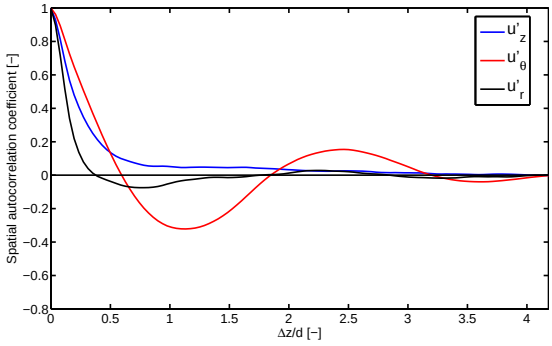

(b) $R_{\Omega,c} = 0$

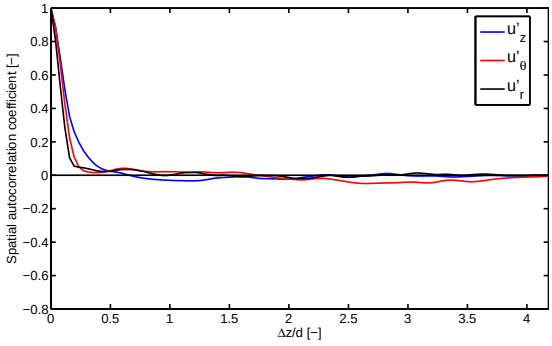

(c) $R_{\Omega,o} = 0.091$

Figure 5.4: Autocorrelation of all three fluctuating velocities in the axial direction at $Re_S = 29000$. Plotted at (a) only inner cylinder rotation, (b) exact counter rotation and (c) only outer cylinder rotation.

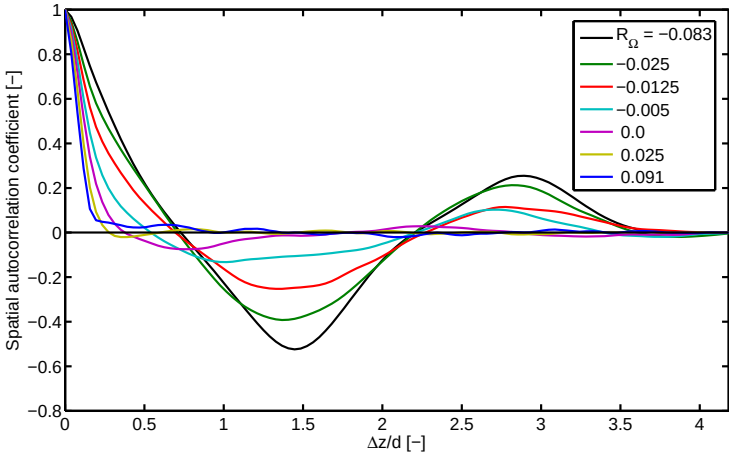

Figure 5.5: Autocorrelation of fluctuating radial velocities (u_r') in the axial direction at $Re_S = 29000$ for different R_Ω.

observed. Similarly, as seen by the radial velocity contours, the velocity fields are relatively more organised at $R_{\Omega,i} = -0.083$, as well. The coherent structures aligned in the azimuthal direction outnumbers the ones aligned in the other directions. However, compared to the Taylor vortices, they have smaller diameters. This confirms the proposed explanations [32, 82, 105] about the appearance of the Taylor vortices in the mean flow by the accumulation of the relatively smaller scale structures.

Close to exact counter-rotation of the cylinders, the structures start to become gradually more disorganized (Figure 5.6(c) and 5.6(d)), which was also indicated by the autocorrelations. The size of the coherent structures decrease and they align themselves in all directions.

If we move towards the only outer cylinder rotation ($R_{\Omega,o} = 0.091$), we observe relatively less change as seen in Figure 5.6(e) and 5.6(f). The size of the coherent structures comparable to those at $R_{\Omega,c} = 0$. Although alignments in all directions are present, the structures are mostly aligned in the axial direction of the cylinders.

The inspection of the instantaneous flow structures even at only three rotation numbers indicates the change of the structures, and confirms the results of Ravelet et al. [82] about the change of the dominant scales at different R_Ω. However, at this point the small scale structures are still dominant in the flow and the visualisations do not give a very clear

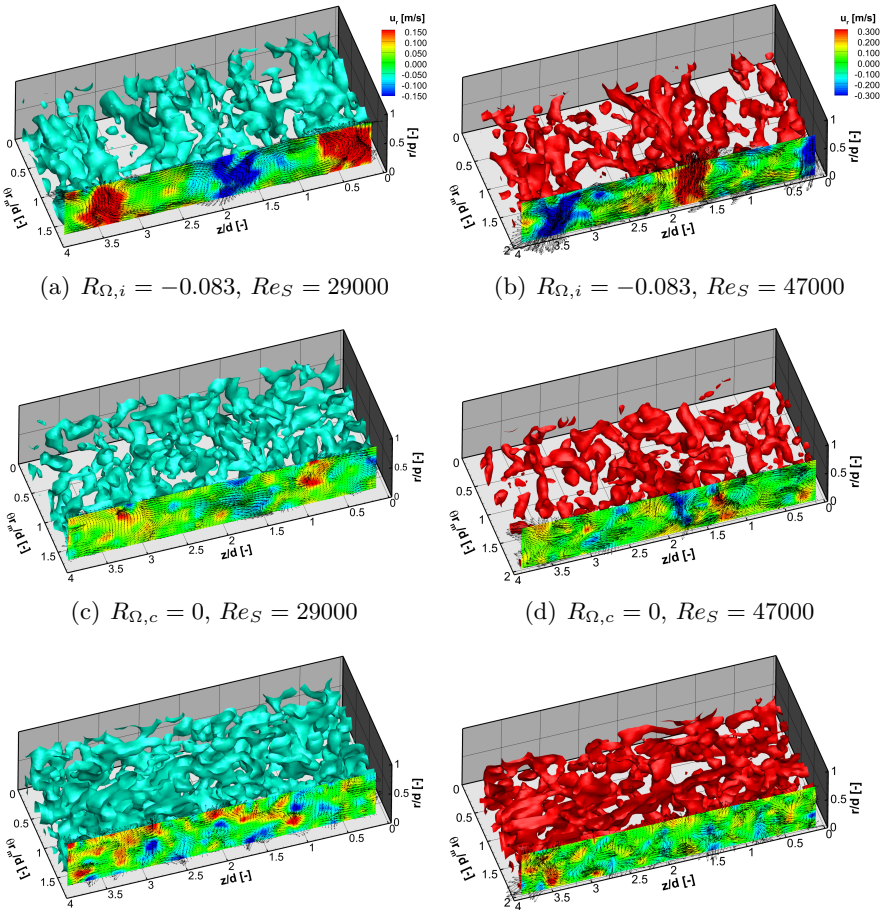

(a) $R_{\Omega,i} = -0.083$, $Re_S = 29000$

(b) $R_{\Omega,i} = -0.083$, $Re_S = 47000$

(c) $R_{\Omega,c} = 0$, $Re_S = 29000$

(d) $R_{\Omega,c} = 0$, $Re_S = 47000$

(e) $R_{\Omega,o} = 0.091$, $Re_S = 29000$

(f) $R_{\Omega,o} = 0.091$, $Re_S = 47000$

Figure 5.6: Examples of the instantaneous turbulent flow structures at $Re_S = 29000$ and 47000, represented by the means of Q-criterion [53] isosurfaces for; (a-b) only inner cylinder rotation, (c-d) exact counter rotation and (e-f) only outer cylinder rotation. Isosurfaces are (a, c, e) $Q = 3000$ s^{-2}, (b, d, f) $Q = 12000$ s^{-2}. The radial velocities (u_r) are color coded.

picture. Therefore one needs to change his approach to reveal how the large and small-scales change.

5.5 Decomposition of the Instantaneous Flow to Large and Smaller-Scale Motions

In order to have a deeper understanding of the dynamics of the flow and to reveal the torque scaling in relation to the instantaneous turbulent flow structures, it was decided to separate the instantaneous large-scale motions from the smaller-scales and inspect them separately for current chapter. The flow is decomposed into large and smaller-scale motions, following the method proposed by Adrian et al. [3].

In turbulence, the decomposition of the instantaneous velocities (u) at each data point is done following the "Reynolds decomposition"

$$u = U + u', \tag{5.1}$$

where U is the time-averaged velocity (over 200 instantaneous fields for current case), and u' stands for the instantaneous fluctuating velocity. According to Adrian et al. [3], the fluctuating part can also be separated into large-scale and small-scale components, such as:

$$u' = u'_L + u'_S. \tag{5.2}$$

The large-scale component u'_L is computed by filtering the instantaneous fluctuating velocities, where the residual is equal to the smaller-scale component u'_S. Second-order regression [38, 86], which is a linear filter, is used for spatial low-pass filtering of the three-dimensional fluctuating velocities (see Chapter 3). The filter length is taken to be the gap width d, which is of the order of the height of a Taylor vortex [13]. If equations 5.1 and 5.2 are combined, we end-up with

$$u = U + u'_L + u'_S, \tag{5.3}$$

which gives the decomposition of the instantaneous flow field containing both large and smaller-scale motions.

In relation with the separation of the large and smaller-scale motions, the Reynolds stress can be computed using the decomposed velocity fields by;

$$\begin{aligned} uv &= (U + u'_L + u'_S)(V + v'_L + v'_S) \\ &= UV + Uv'_L + Uv'_S + u'_L V + u'_S V \\ &+ u'_L v'_L + u'_L v'_S + u'_S v'_L + u'_S v'_S. \end{aligned} \tag{5.4}$$

If the average of the Reynolds stress is taken over time, as some terms (which include production of a mean and fluctuation) are equal to zero by definition, one ends-up with the equation to compute the Reynolds stress as given below.

$$\begin{aligned} \overline{uv} &= UV + \cancel{\overline{Uv'_L}} + \cancel{\overline{Uv'_S}} + \cancel{\overline{u'_L V}} + \cancel{\overline{u'_S V}} + \overline{u'_L v'_L} + \overline{u'_L v'_S} + \overline{u'_S v'_L} + \overline{u'_S v'_S} \\ &= UV + \overline{u'_L v'_L} + \overline{u'_L v'_S} + \overline{u'_S v'_L} + \overline{u'_S v'_S}. \end{aligned} \tag{5.5}$$

The decomposition is examined by computing the kinetic energy contained in the large and smaller-scale motions by means of velocity RMS values (Figure 5.7). Close to the $R_{\Omega,c}$ ($-0.025 \leq R_\Omega \leq 0.005$), the energy contained in the ILS shows a maximum, which implies that most of the energy included in the turbulent flow is due to the large scale motions in this R_Ω range. The relative kinetic energy contribution of the ILS becomes lower than the ISS for positive rotation numbers (especially $R_\Omega \geq 0.050$). However the ILS contain significant amount of energy for all R_Ω.

5.5.1 Change of the instantaneous large-scale structures with rotation

The visualisation of the decomposed vector fields reveals the change of the orientation of the ILS with the relative rotational speeds of the cylinders. The vortical structures are computed using sum of the mean flow and ILS, and represented by Q-criterion [53] isosurfaces in Figures 5.8 and 5.9. As it will be shown in Section 5.6, the mean flow is only effective close to $R_{\Omega,i} = -0.083$ and does not contribute much for other R_Ω. The change of the organisation is explained below starting from

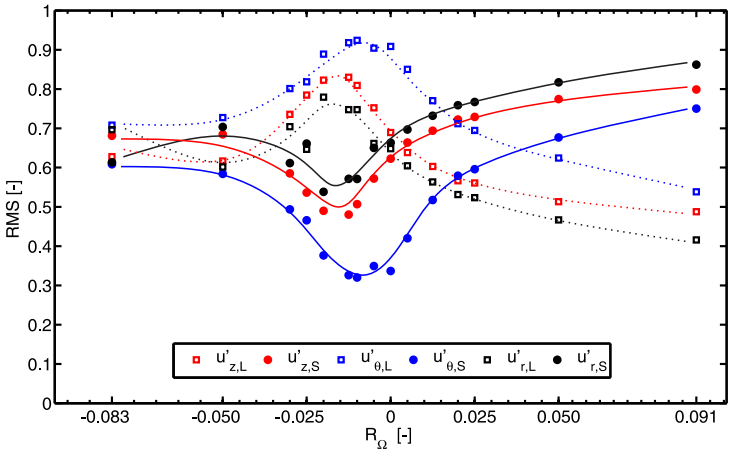

Figure 5.7: RMS of fluctuating large and small-scale velocities at $Re_S = 29000$. u'_z, u'_θ and u'_r represent the fluctuating velocities in the axial, azimuthal and the radial directions, respectively. The second indices L and S (i.e. $u'_{z,L}$ and $u'_{z,S}$) represent the large and smaller-scale component of the fluctuating velocity, respectively. The lines are to guide the eye.

only inner cylinder rotation ($R_{\Omega,i} = -0.083$) and increasing the R_Ω at $Re_S = 29000$. However, the change also holds for other two Reynolds numbers that were examined.

At $R_{\Omega,i} = -0.083$ ($Ro = -\infty$), the ILS have tube-like shapes (Figure 5.8(a)). They are elongated in the azimuthal direction with axes almost parallel to the cylinder walls. These structures are analogous to Taylor vortices that are observed in the time-averaged flow at similar R_Ω, as well as to those in the instantaneous flow at different Reynolds numbers (i.e. $Re \sim 10^3 - 10^4$ by Dong [32] and $Re \sim 10^4$ by van Hout & Katz [111]). The ILS appear as counter-rotating pairs, covering the whole range in the axial direction of the cylinder. High positive and negative radial velocity zones are located in between the ILS. However, their distribution in the axial direction is not as homogeneous as it is for Taylor vortices, and their diameters are found to be slightly smaller than regular Taylor vortices. Examination at different time steps revealed that the axial movement of the vortices are minimal. The presence of the ILS without any significant axial movement explains the reported observations of the

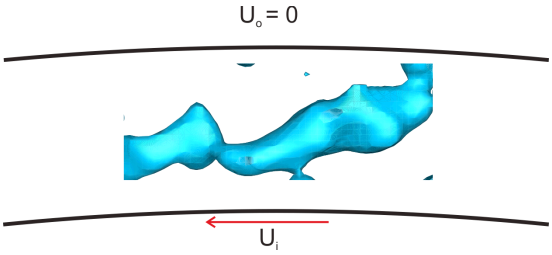

(a) $R_{\Omega,i} = -0.083$

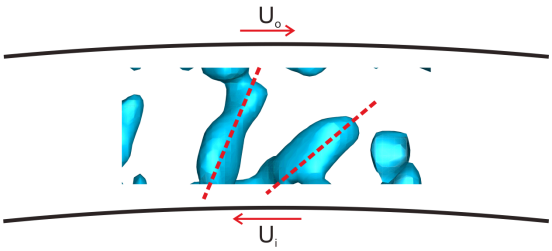

(b) $R_{\Omega} = -0.010$

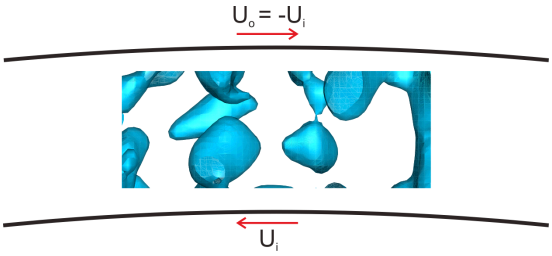

(c) $R_{\Omega,c} = 0$

Figure 5.8: Typical ILS for different R_Ω at $Re_S = 29000$, shown by 2D projections on the azimuthal-radial plane, represented by the means of Q-criterion [53] isosurfaces ($Q = 2000$ s^{-2}) of ILS+mean flow motions. The rotation directions of the cylinders are represented by red arrows. Dimensions are not to scale.

Taylor vortices in the time-averaged flow [32, 82, 105]. Similar findings of ILS are also reported by Dong [33] at exact counter rotation of the cylinders ($R_{\Omega,c} = 0$), but at relatively lower Re_S ($1000 \leq Re_S \leq 8000$) and smaller gap ratio ($\eta = 0.5$). The difference of R_Ω between the studies might be associated with the gap ratio and/or Reynolds number dependency of the organisation of ILS, which was suggested by Dong [33]. However, no significant Re_S dependence is observed in the current study.

Increase of the R_Ω results in a small deformation of the shapes of the ILS until $R_\Omega = -0.010$, that is they become shorter. However, there is a significant change of orientation in this range. The ILS are still mostly elongated in the azimuthal direction, but they tend to have an inclination with the cylinder walls (Figure 5.8(b)). The inclination angle increases with increasing R_Ω, such that the ILS tend to connect the inner and the outer cylinder walls. It is found that the inclination enhances turbulent angular momentum transport, which will be discussed later. Further increment of the rotation number in the proximity of $R_{\Omega,c}$ ($-0.005 \leq R_\Omega \leq 0.0125$) reveals a considerable deformation of the ILS, as seen in Figure 5.8(c). The orientational preference and the elongation are lost and they appear as blob-like structures (Figure 5.8(c)). The change of the ILS and ISS in this range are in agreement with results of van Hout & Katz [111] and confirm the suggestions of Ravelet et al. [82].

Taylor column-like structures

Further increase of R_Ω reveals a completely new organisation of the ILS, which has not been reported in the literature on Taylor-Couette flow before. Especially at higher rotation numbers ($R_\Omega = 0.050$ and 0.091), the axes of the ILS are found to be aligned in the axial direction of the cylinders (Figure 5.9). The axially elongated ILS at $R_\Omega = 0.050$ and 0.091 ($Ro = -1.304$ and -1) are longer than the azimuthal ILS observed at negative rotation numbers. Even though they are segmented instead of a single long column, these structures resemble Taylor columns. In fact, similar structures have been reported in the literature for analogous rotating flows, such as rotating Rayleigh-Bénard flow at $Ro < 1$ [59, 98]. Recent numerical studies focusing on the perturbations in turbulent Taylor-Couette flow proposed the presence of columnar structures in both co-rotating (close to only-outer cylinder rotation) and counter-

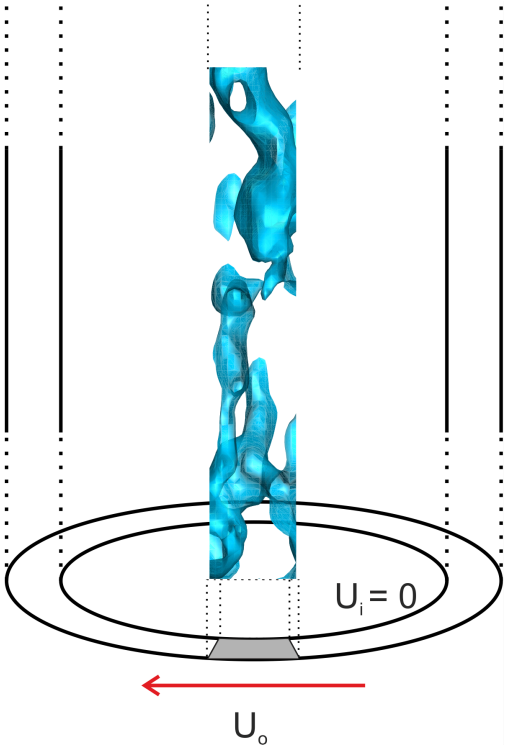

Figure 5.9: Typical ILS at $R_{\Omega,o} = 0.091$ at $Re_S = 29000$, shown by 2D projection on the azimuthal-axial plane, represented by the means of Q-criterion [53] isosurfaces ($Q = 2000\ \mathrm{s}^{-2}$) of ILS+mean flow motions. The rotation direction of the outer cylinder is represented by a red arrow. Dimensions are not to scale.

rotating regimes [66]. However, till now they have not been observed experimentally or numerically in Taylor-Couette flow.

A few differences were observed between the Taylor column-like structures that are reported in Taylor-Couette and Rayleigh-Bénard flows. Unlike the counter rotating pairs of Taylor column-like structures in Rayleigh-Bénard flow [50, 59], they appear as co-rotating columns in Taylor-Couette flow. Additionally, azimuthal positions of the vortices change spatially, which causes the Taylor column-like structures to be averaged-out in the mean. This explains the absence of Taylor column-like structures in the time-averaged flow.

It can be conjectured that the occurrence of these Taylor column-like structures in turbulent Taylor-Couette flow are related with the top and bottom boundary conditions [50, 98]. Studies performed with different configurations (such as very high Γ or stationary endplates) would not result in the Taylor column observation. On the other hand, as their segmented form might suggest, they may be associated with instability [66], as well. It should be noted that no significant Re_S dependence of the Taylor column-like structures was observed over current range of Re_S.

5.5.2 Quantification of the orientation of the instantaneous large-scale structures

The results of visual inspection is further supported by quantification of the orientation of the vorticity vector within the ILS vortical structures. The vorticity vectors are computed using the 3D-3C velocity fields at $Re_S = 29000$ and distribution of the angles are plotted in Figure 5.10 and 5.11. The β represents the angle between the vorticity vector and the axial direction on the azimuthal-axial plane. The ϕ shows the elevation of the vorticity vector with respect to the same plane (see inset of Figure 5.10). The angles are computed at data points where $Q \geq 2000$ s^{-2}, representing the isosurfaces given in Figures 5.8 and 5.9. Higher Q thresholds ($2000 \leq Q \leq 3000$ s^{-2}) were also tested, however no significant Q dependency of the results was observed.

The results show that at $R_{\Omega,i} = -0.083$, the structures mostly accumulate around $\beta = 90$ and $-90°$, in a relatively small ϕ range (Figure 5.10 (a)), confirming the alignment in the azimuthal direction resembling Taylor vortices. At $R_\Omega = -0.010$ (Figure 5.10 (b)), the distribution of angles broadens and ϕ in particular attains higher magnitudes consistent with the observed increase in the inclination of the vortices. In the case of $R_{\Omega,c} = 0$ (Figure 5.11 (a)) the data is more evenly scattered over horizontal-S shape. The relative number of occurrences in the $\beta = \phi = 0°$ neighbourhood is significantly increased. This almost uniform distribution of β and ϕ confirms the blob-like structures, having no significant preference of orientation, as previously shown in Figure 5.8(c). At $R_{\Omega,o} = 0.091$ the distribution of angles reveal again a significant change (Figure 5.11 (b)). The data is accumulated at both $\beta = 0°$ and $\phi = 0$, with a scatter range much smaller than the other cases. This

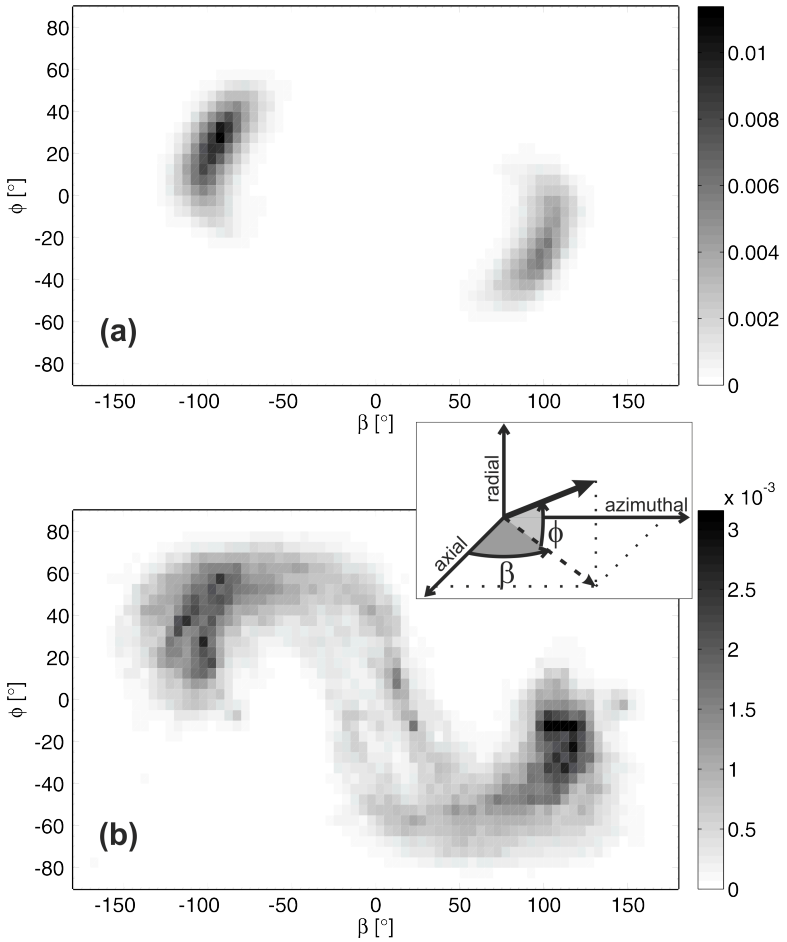

Figure 5.10: Joint p.d.f of the orientation of the vorticity vectors in the azimuthal-axial plane w.r.t axial direction (β), and the elevation w.r.t the same plane (ϕ) at $Re_S = 29000$ and $R_{\Omega,i} = -0.083$ (a), $R_\Omega = -0.010$ (b).

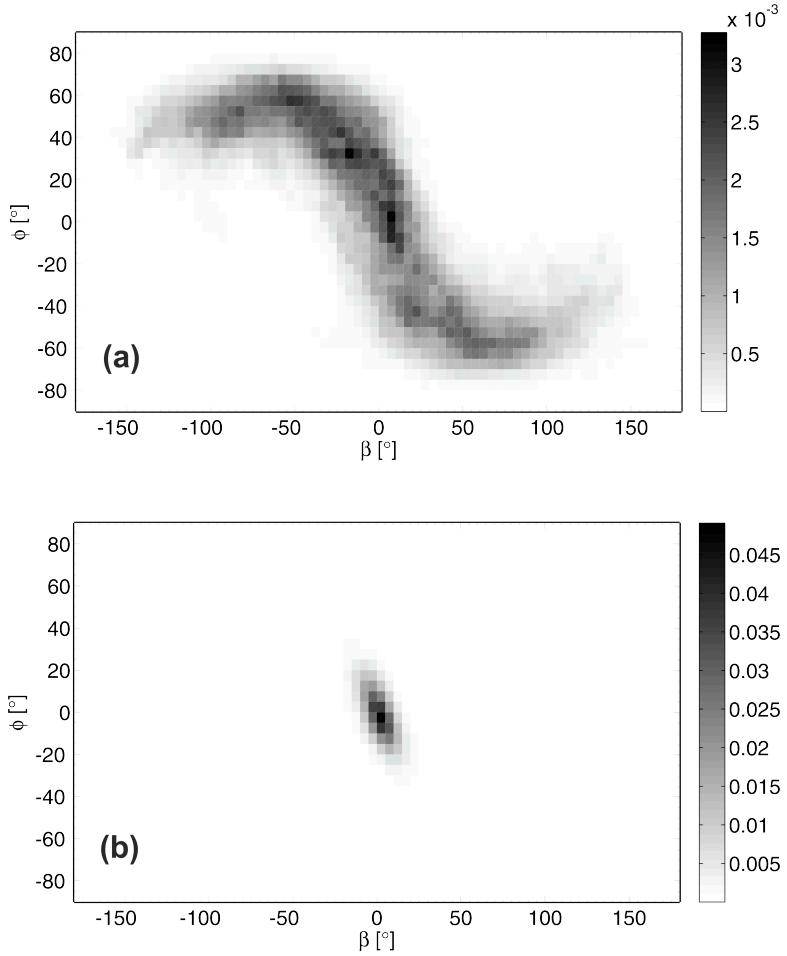

Figure 5.11: Joint p.d.f of the orientation of the vorticity vectors in the azimuthal-axial plane w.r.t axial direction (β), and the elevation w.r.t the same plane (ϕ) at $Re_S = 29000$ and $R_{\Omega,c} = 0$ (a), $R_{\Omega,o} = 0.091$ (b).

clearly confirms previous visual inspection of Taylor column-like vortical structures that are aligned in the axial direction (see Figure 5.9). Although only four R_Ω are given here, the results at intermediate R_Ω follow the same trend and confirm the visual findings.

5.6 Contribution of Coherent Structures to Reynolds Stress

In addition to the organisational change, the contribution of the ILS to the torque was studied by means of friction coefficient,

$$C_f = \frac{\bar{\tau}}{\rho U_{sh}^2}, \tag{5.6}$$

where $\bar{\tau}$ represents the mean Reynolds stresses in the radial gap and U_{sh} ($= S \times d$, where S is the laminar shear rate) is the shear velocity [35,82]. It was assumed that the wall shear rate is equal to the total mean stress in the flow. Given that the viscous stresses in the bulk are negligible and only important in a very thin region near the wall, the total stress is almost equal to the Reynolds stress in the bulk flow.

Results in Figure 5.12 show that the most significant influence to the Reynolds stress is due to the interaction between the fluctuating velocities in the azimuthal and the radial directions ($\overline{u'_\theta u'_r}$). Compared to the measurements with the torque meter presented by Ravelet et al. [82] (see Figure 5.1 and "total torque data" in Figure 5.12), current C_f values from PIV (indicated as "total" in Figure 5.12) are on average 0.15×10^{-3} lower for all R_Ω studied. Please note that Ravelet et al. [82] plotted the C_f values based on the total measured torque of the setup (which also includes top and bottom von Karman gaps). In this chapter, the contribution of the von Karman gaps were subtracted from the total C_f, assuming the torque in the von Karman gap is independent of R_Ω and is equal to half of the measured torque at $R_{\Omega,o} = 0.091$, as suggested [82]. However, apart from the nearly constant shift, the C_f essentially follow the same trend.

Figure 5.12 shows that the turbulent stress due to the large-large scale interaction in the azimuthal-radial direction ($\overline{u'_{\theta,L} u'_{r,L}}$) is dominant for all R_Ω, except $R_\Omega \geq 0.025$. The stress due to $\overline{u'_{\theta,L} u'_{r,L}}$ reaches its

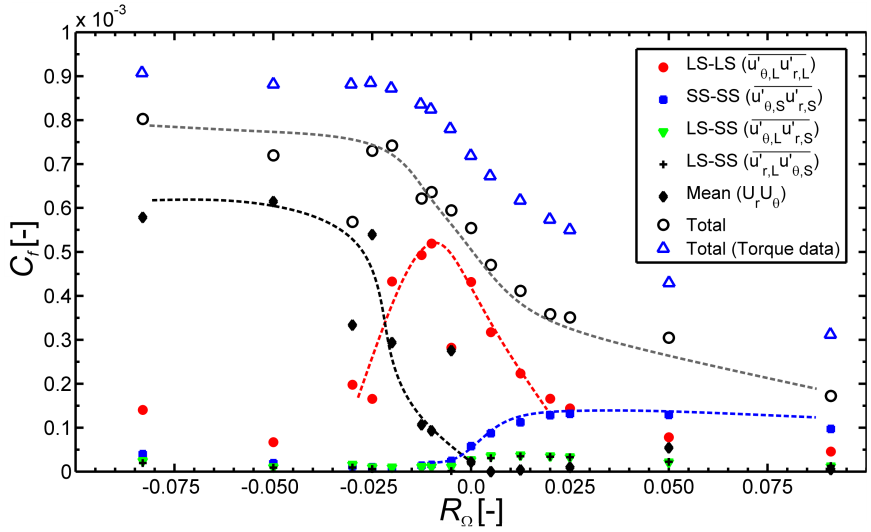

Figure 5.12: The friction factor C_f due to the interaction between the instantaneous large scale (LS) and smaller-scale (SS) motions in the azimuthal-radial directions, as a function of R_Ω, measured at the center of the gap d at $Re_S = 29000$. The u'_θ and u'_r represent the fluctuating velocities in the azimuthal and radial directions, and U is the mean velocity, respectively. The values indicated by "total" represent the sum of all C_f values (including the contributions of all scales and directions) that are computed using tomographic PIV. The torque values (i.e. "total torque data") are adapted from Ravelet et al. [82]. The dashed lines are indicative.

peak value at $R_\Omega \approx -0.010$, where the azimuthal ILS contain most of the turbulent kinetic energy, associated with the inclined structures connecting the inner and outer cylinders, as discussed previously.

The interactions including any smaller-scale motion are negligible for $R_\Omega < 0$. However, the contribution of smaller-smaller scale interaction in the azimuthal-radial direction ($\overline{u'_{\theta,S}u'_{r,S}}$) starts to increase around $R_{\Omega,c} = 0$ for increasing R_Ω values, and becomes the dominant Reynolds stress for $R_\Omega > 0.025$. Actually, the increment is also valid for large-smaller scale interactions in the azimuthal-radial direction (i.e. $\overline{u'_{\theta,L}u'_{r,S}}$ and $\overline{u'_{r,L}u'_{\theta,S}}$). This trend can be explained by higher turbulent kinetic energy contained in the ISS for this R_Ω range, as explained in Section 5.5 (see Figure 5.7).

5.7 Large and Smaller-Scale Structure Interaction versus the Change of Torque

In the light of the observations made about the organisational change of the ILS, the optimum angular momentum transportation in Taylor-Couette flow can be explained. According to the results presented here, at highly negative rotation numbers ($-0.083 \leq R_\Omega \leq -0.025$), the relatively well-organised ILS, as well as the ISS, are inefficient in terms of angular momentum transport. At that range, most of the contribution to C_f is due to the mean flow. However, close to the $R_{\Omega,c}$, the transformation from azimuthal alignment to the inclined vortices enhance the turbulent angular momentum transfer. This is because the inclined vortices induce $u'_{\theta,L}$ and $u'_{r,L}$ simultaneously enhancing their overall correlation ($\overline{u'_{\theta,L}u'_{r,L}}$), which contributes significantly to the Reynolds shear stress. This is in agreement with a statement of Tennekes and Lumley [103], where they suggest that the vortical structures that are aligned with the direction of the mean strain rate are more effective for transferring energy between the mean flow and turbulence.

Therefore, slightly negative rotation ($-0.0125 \leq R_\Omega \leq -0.005$) becomes the region where the turbulent angular momentum transport is enhanced. On the other hand, the optimum angular momentum occurs at $R_\Omega \approx -0.025$, which might be due to the coexistance of the $\overline{u'_{\theta,L}u'_{r,L}}$ and the mean flow in the region. Compared to the literature with lower η ($= 0.500 - 0.717$), the change of the location of the optimum angular

momentum transfer closer to $R_{\Omega,c} = 0$ is in agreement with the predictions for Taylor-Couette setups with $\eta \to 1$ [16, 109, 110].

After the peak, the efficiency of ILS decreases for increasing R_Ω. It is due to the fact that, at positive rotation numbers, the ILS start to align themselves in the axial direction as co-rotating Taylor column-like structures, where the angular momentum cannot be transported efficiently. In the mean time, the ISS start to take over the dominant role of the ILS in the flow. However, the ISS do not contain enough energy to keep the angular momentum transportation as high as the ILS around $R_\Omega \approx -0.010$.

5.8 Conclusion

In this chapter, using fully volumetric measurements, the rotational dependence of the coherent structures and their influence to the reported change of the torque values were investigated in fully turbulent, counter-rotating Taylor-Couette flow at constant shear. The investigations at the mean and the instantaneous flow showed the significant dimensional and orientational change of the turbulent flow structures. In order to get more insight on the dynamics of the flow, the instantaneous flow fields were studied by separating into large and smaller-scale motions. The change of instantaneous large-scale structures from azimuthally aligned structures to Taylor column-like structures, with intermediate regimes, was shown quantitatively and qualitatively.

Additionally the stresses associated with the large and smaller-scale structures were computed. It is found that close to only inner cylinder rotation, the large and smaller scale structures are inefficient for the angular momentum transport, whereas the mean flow is responsible for the measured stresses. In the proximity of the exact counter-rotation of the cylinders, the roles change. The inclined large-scale vortices enhance the turbulent angular momentum transport. Using the change of the structures and computing their contribution to torque it was possible to explain the reported behaviour of torque and angular momentum transport.

6 Conclusions and Outlook

6.1 General Conclusions

The aim of this thesis was to measure the coherent turbulent flow structures in turbulent Taylor-Couette flow, and examine their contribution to the torque. In order to perform the experimental analysis in a fully volumetric measurement domain, state-of-the-art tomographic PIV is implemented to the Taylor-Couette setup. In Chapter 2, the details of the implementation of the tomographic PIV is explained and validated. The measurements are performed in a volume with a size of $40 \times 20 \times 10$ mm^3 in axial, azimuthal and radial directions, respectively. The laminar flow is analytically well defined in the Taylor-Couette geometry and therefore used to validate the measurements. It is found that the maximum error on the mean velocity estimation (relative to the inner cylinder wall velocity) is 3.2% for the azimuthal velocity and below 0.7% for the axial and the radial velocities. In steady laminar flow the RMS of the velocities are a measure for the random noise, which is below 1.5% over most of the gap, but reaches to 4.8% of the outer cylinder velocity. Additionally, in order to demonstrate the capabilities of tomographic PIV, examples of flow structures at different flow states like Taylor-vortex flow and fully turbulent flow are presented in Chapter 2. Details of the problems that were experienced during the implementation (such as the illumination, reflection and optical distortions), and the solutions are explained in the same chapter.

The actual spatial resolution of tomographic PIV, and even the way to define it (either the distance between two neighbouring vectors or the size of the interrogation window), is still a debate in the literature. In Chapter 3, the actual spatial resolution of tomographic PIV is analysed to clarify the spatial resolution issue. Taylor-Couette flow is almost ideal for this analysis because of the independent torque measurements that can be used to determine the power supplied to the flow. In fully turbulent Taylor-Couette flow, the power input is directly related to the

viscous dissipation rate in the flow [80]. The fully volumetric measurement techniques such as tomographic PIV provide velocity gradients of all three velocity components in all directions, which allows the dissipation rate to be estimated. Comparison of those two independent dissipation values provides the necessary information about the actual resolution of the tomographic PIV. A parametric study is performed over several variables such as the Reynolds number, the interrogation volume size and overlap, to see how do they effect the spatial resolution. The large-eddy PIV method [95] is also tested to check its performance on the improvement of the dissipation rate estimations.

It is found that the dissipation rates are underestimated for most of the turbulent flow measurements, with the exception of the low Reynolds number cases. The underestimation increases with the Reynolds number at fixed window size. The results showed that the accuracy of the dissipation rate estimations is strongly related to both the interrogation volume size and the space between the vectors (which is a combination of both interrogation volume size and interrogation volume overlap). It is found that the actual spatial resolution of tomographic PIV is a nonlinear function of both interrogation volume size and the overlap ratio, such that decreasing the volume overlap at a constant interrogation size increases the error, whereas it results in lower error compared to similar vector spacing with larger interrogation volume sizes. The computations are more sensitive to the changes of the interrogation volume size than the vector spacing. Despite the fact that some studies in the literature define the spatial resolution by the interrogation volume size, it was shown here that the vector spacing is a more suitable parameter to quantify the actual spatial resolution of tomographic PIV and PIV in general. Additionally oversampling the data with high overlap ratios result in better estimations, even though it possibly results in a higher data density than the actual tracer particle density. On the other hand, the large-eddy method is found to improve the estimations compared to the direct estimations by tomographic PIV. The spatial-resolution requirement of tomographic PIV to fully resolve the turbulent dissipation scales is also defined in the same chapter. It is found that a vector spacing of $1.5 - 2.0$ times Kolmogorov length scale (which is equal to interrogation volume size of $6.0 - 8.0$ times Kolmogorov length scale at 75% overlap) should be aimed to resolve all scales, which confirms previous studies with 2D and tomographic PIV [18, 54, 85, 122]. However,

the results indicate that if the vector spacing is kept small using high overlap ratios (up to 75%), the restriction of using small interrogation volume size can be relaxed. Therefore, interrogation volumes that are larger than the values suggested in the literature might be used while still having a enough spatial resolution to resolve small scales. On the other hand, as a post-processing routine, the large eddy PIV method can be used to improve the dissipation rate estimation, especially for high Reynolds numbers.

In Chapter 4, time-resolved tomographic PIV is implemented to the Taylor-Couette geometry in order to demonstrate possible capabilities of the technique for investigating the dynamics of fully turbulent Taylor-Couette flow. The measurements are performed at exact-counter-rotation of the cylinders (i.e. the absolute velocity of the inner cylinder wall is equal to the outer cylinder wall, but they are rotating in opposite directions), where the velocity of the mean flow in the bulk is nearly zero. Due to this advantage, it is possible to have a longer observation times to track the coherent structures passing through the measurement volume, compared to similar studies in a boundary layer or channel flow. Actually, the convection velocity of the structures are found to be non-zero despite the approximately zero mean flow. They advance in the azimuthal direction depending on their radial position. The most frequently observed coherent vortex structure are the tube-like vortices, which are elongated in the azimuthal direction. Several dynamic events in turbulent Taylor-Couette flow, such as bursts of the azimuthal velocity in the radial direction, and stretch and break-up of the tube-like vortices are observed and discussed.

The dependence of the torque values on the relative rotation speeds of the cylinders at a constant Reynolds number is a widely studied subject in the literature [16, 76, 82, 109, 110]. In this thesis, tomographic PIV is used to analyse the turbulent flow structures to reveal any connection with the change of the torque scaling at counter-rotation regime (Chapter 5). It is shown that even at a constant shear rate, the mean and instantaneous turbulent flow structures change significantly with the rotation number, i.e. the relative rotation speed and direction of the cylinders. Large-scale structures resembling Taylor-vortex flow dominate the mean flow at negative rotation numbers (i.e. the inner cylinder is rotating faster than the outer cylinder in the opposite direction). They disappear from the mean in the case of positive rotation numbers (i.e.

the outer cylinder is rotating faster than the inner cylinder in the opposite direction).

More detailed analysis on the dependence of the turbulent flow structures to the rotation number is performed by decomposing the instantaneous flow fields to large and smaller-scale motions. It is shown that the instantaneous large-scale structures change significantly with the rotation number, similar to the mean flow structures. New sub-regimes with azimuthally aligned structures (resembling Taylor-vortices), azimuthally aligned structures with inclined axes, as well as structures with no orientational preference are defined. Additionally, Taylor column-like coherent structures, which are elongated in the axial direction of the cylinders, are observed in Taylor-Couette flow for the first time. Using the Reynolds stresses associated with the different types of the large and smaller-scale coherent motions, it was possible to explain the highly discussed change of the torque scaling values. The results show that the inclined vortices are responsible for the increase of the angular momentum transport between the cylinders.

The relatively well-organised instantaneous large and smaller-scale structures are found to be inefficient in angular momentum transport at highly negative rotation numbers ($-0.083 \leq R_\Omega \leq -0.025$), where most of the contribution to the friction factor C_f is due to the mean flow. At slightly negative rotation numbers close to exact-counter rotation ($-0.0125 \leq R_\Omega \leq -0.005$), the inclined vortices enhance the turbulent angular momentum transfer by inducing velocities in the azimuthal and the radial directions, which contributes significantly to the Reynolds shear stress. In the case of positive rotation numbers, the instantaneous large-scale structures start to align themselves in the axial direction as co-rotating Taylor column-like structures, so that the angular momentum cannot be transported efficiently any more. At the same time, the smaller-scale structures become dominant over the large-scales in terms of their angular momentum transfer. However, the total momentum transfer drops.

6.2 Outlook

This study provides new insights about the role of the coherent turbulent flow structures on skin friction and torque. Currently the connection

between those two subjects is weak in the case of Taylor-Couette flow. This study may be seen as a step forward to understand the relation between them and it can further be extended to other flow types like the co-rotating regime, as well as the dependence of the results on the gap ratio of the cylinders.

On the other hand, the most imminent and practical application of this study would probably be based on the results presented in Chapter 3 on the spatial resolution of tomographic PIV. Users of tomographic (or other) PIV technique may benefit from the results and they can adjust their measurement parameters to resolve small flow scales in turbulence. Although the results presented in this thesis show that the spatial resolution of tomographic PIV increases with the overlap of interrogation volumes in the studied range ($0 \leq overlap \leq 75\%$), there still remains a question about its limits. Probably the trend of improvement does not continue up to very high overlap values (i.e. 99%), and there may be an optimum value in between. However, due to the required computation time of tomographic PIV, it was not possible to further extend the investigation range or steps within current study, and the analysis remained limited to the cases presented here. Further studies should include a wider range of interrogation volume overlap ratios to determine or confirm the possible optimum value.

Due to the very small convection velocity (and therefore the longer observation time), the time-resolved measurements in a turbulent flow with approximately zero mean velocity is a promising approach to study the evolution of coherent motions in turbulence. Although plane Couette and Taylor-Couette flows are widely used for different studies, it is interesting that the "approximate zero mean velocity" principle has yet not been employed in the literature of plane Couette and Taylor-Couette flows. As it is shown here, with the combination of time-resolved and volumetric measurements, tracking coherent flow motions and studying their evolution in 3D may provide more insight about the dynamics of turbulence. Further studies may benefit from the fact that those two flow types can also be used for studying the flow under the influence of an accelerating (or decelerating) wall. The time-resolved results given in Chapter 4 remained limited to the few examples of the events, rather than a detailed quantitative analyse of the dynamics of the turbulent flow that is investigated. Further detailed analyses can be performed using the obtained data including additional Reynolds numbers.

Bibliography

[1] N Abcha, N Latrache, F Dumouchel, and I Mutabazi. Qualitative relation between reflected light intensity by Kalliroscope flakes and velocity field in the Couette-Taylor flow system. *Exp. Fluids*, 45(1):85–94, 2008.

[2] R J Adrian. Hairpin vortex organization in wall turbulence. *Phys. Fluids*, 19(4):041301, 2007.

[3] R J Adrian, K T Christensen, and Z-C Liu. Analysis and interpretation of instantaneous turbulent velocity fields. *Exp. Fluids*, 29(3):275–290, 2000.

[4] R J Adrian, C D Meinhart, and C D Tomkins. Vortex organization in the outer region of the turbulent boundary layer. *J. Fluid Mech.*, 422:1–54, 2000.

[5] R J Adrian and J Westerweel. *Particle Image Velocimetry*. Cambridge University Press, Cambridge, 2011.

[6] A Akonur and R M Lueptow. Three-dimensional velocity field for wavy Taylor-Couette flow. *Phys. Fluids*, 15(4):947–960, 2003.

[7] C D Andereck, S S Liu, and H L Swinney. Flow regimes in a circular Couette system with independently rotating cylinders. *J. Fluid Mech.*, 164:155–183, 1986.

[8] C Atkinson and J Soria. An efficient simultaneous reconstruction technique for tomographic particle image velocimetry. *Exp. Fluids*, 47(4-5):553–568, 2009.

[9] K Avila and B Hof. High-precision Taylor-Couette experiment to study subcritical transitions and the role of boundary conditions and size effects. *Rev. Sci. Instrum.*, 84(6):065106, 2013.

[10] M Avila. Stability and angular-momentum transport of fluid flows between corotating cylinders. *Phys. Rev. Lett.*, 108(12):124501, 2012.

[11] S Baldi and M Yianneskis. On the direct measurement of turbulence energy dissipation in stirred vessels with PIV. *Ind. Eng. Chem. Res.*, 42(26):7006–7016, 2003.

[12] G K Batchelor. *An Introduction to Fluid Dynamics*. Cambridge University Press, Cambridge, 1967.

[13] M Bilson and K Bremhorst. Direct numerical simulation of turbulent Taylor–Couette flow. *J. Fluid Mech.*, 579:227–270, 2007.

[14] D Borrero-Echeverry and M F Schatz. Transient turbulence in Taylor-Couette flow. *Phys. Rev. E*, 81(2), 2010.

[15] H J Brauckmann and B Eckhardt. Direct numerical simulations of local and global torque in Taylor–Couette flow up to Re = 30000. *J. Fluid Mech.*, 718:398–427, 2013.

[16] H J Brauckmann and B Eckhardt. Intermittent boundary layers and torque maxima in Taylor-Couette flow. *Phys. Rev. E*, 87(3):033004, 2013.

[17] M J Burin, E Schartman, and H Ji. Local measurements of turbulent angular momentum transport in circular Couette flow. *Exp. Fluids*, 48(5):763–769, 2010.

[18] O R H Buxton, S Laizet, and B Ganapathisubramani. The effects of resolution and noise on kinematic features of fine-scale turbulence. *Exp. Fluids*, 51(5):1417–1437, 2011.

[19] P R N Childs. *Rotating Flow*. Butterworth-Heinemann, 1st edition, 2011.

[20] M R Cholemari. Modeling and correction of peak-locking in digital PIV. *Exp. Fluids*, 42(6):913–922, 2007.

[21] J A Cole. Taylor-vortex instability and annulus-length effects. *J. Fluid Mech.*, 75(1):1–15, 1976.

[22] D Coles. Transition in circular Couette flow. *J. Fluid Mech.*, 21(3):385–425, 1965.

[23] D Coles and C Van Atta. Measured distortion of a laminar circular Couette flow by end effects. *J. Fluid Mech.*, 25(3):513–521, 1966.

[24] O Dauchot and F Daviaud. Finite amplitude perturbation and spots growth mechanism in plane Couette flow. *Phys. Fluids*, 7:335, 1995.

[25] R Delfos, F Ravelet, and J Westerweel. Scaling of torque in turbulent Taylor-Couette flow with background rotation. In B Eckhardt, editor, *Adv. Turbul. XII*, volume 132 of *Springer Proceedings in Physics*, pages 629–632. Springer-Verlag, 2009.

[26] R Delfos, S Tokgoz, A Alidai, G E Elsinga, and J Westerweel. Influence of end effects on laminar Taylor-Couette flow. In *18th Int. Couette-Taylor Work.*, Twente, 2013.

[27] R Deng, D Y Arifin, Y C Mak, and C-H Wang. Characterization of Taylor vortex flow in a short liquid column. *AIChE J.*, 55(12):3056–3065, 2009.

[28] R C Di Prima and H L Swinney. Instabilities and transition in flow between concentric rotating cylinders. In H L Swinney and J P Gollub, editors, *Hydrodyn. Instab. Transit. to Turbul.*, volume 45, chapter 6, pages 139–180. Springer Berlin Heidelberg, 2nd edition, 1985.

[29] F J Diez, Y Cheng, and A Villegas. Time resolved visualization of structures of velocity gradients measured with near Kolmogorov-scale resolution in turbulent free-shear flows. *Exp. Therm. Fluid Sci.*, 35(6):1223–1229, 2011.

[30] S Discetti and T Astarita. A fast multi-resolution approach to tomographic PIV. *Exp. Fluids*, 52(3):765–777, 2011.

[31] S Discetti, A Natale, and T Astarita. Spatial filtering improved tomographic PIV. *Exp. Fluids*, 54(4):1505, 2013.

[32] S. Dong. Direct numerical simulation of turbulent Taylor–Couette flow. *J. Fluid Mech.*, 587:373–393, 2007.

[33] S Dong. Turbulent flow between counter-rotating concentric cylinders: a direct numerical simulation study. *J. Fluid Mech.*, 615:371–399, 2008.

[34] R J Donnelly. Taylor–Couette flow: the early days. *Phys. Today*, 44(11):32–39, 1991.

[35] B Dubrulle, O Dauchot, F Daviaud, P-Y Longaretti, D Richard, and J-P Zahn. Stability and turbulent transport in Taylor-Couette flow from analysis of experimental data. *Phys. Fluids*, 17(9):095103, 2005.

[36] B Eckhardt, S Grossmann, and D Lohse. Torque scaling in turbulent Taylor-Couette flow between independently rotating cylinders. *J. Fluid Mech.*, 581:221–250, 2007.

[37] G E Elsinga. *Tomographic Particle Image Velocimetry and Its Application to Turbulent Boundary Layers*. Phd thesis, Delft University of Technology, 2008.

[38] G E Elsinga, R J Adrian, B W van Oudheusden, and F Scarano. Three-dimensional vortex organization in a high-Reynolds-number supersonic turbulent boundary layer. *J. Fluid Mech.*, 644:35–60, 2010.

[39] G E Elsinga and B Ganapathisubramani. Advances in 3D velocimetry. *Meas. Sci. Technol.*, 24(2):020301, 2013.

[40] G E Elsinga and I Marusic. Evolution and lifetimes of flow topology in a turbulent boundary layer. *Phys. Fluids*, 22(1), 2010.

[41] G E Elsinga, C Poelma, A Schröder, R Geisler, F Scarano, and J Westerweel. Tracking of vortices in a turbulent boundary layer. *J. Fluid Mech.*, 697:273–295, 2012.

[42] G E Elsinga, F Scarano, B Wieneke, and B W van Oudheusden. Tomographic particle image velocimetry. *Exp. Fluids*, 41(6):933–947, 2006.

[43] G E Elsinga, B W van Oudheusden, and F Scarano. Experimental assessment of Tomographic-PIV accuracy. In *13th Int. Symp. Appl. Laser Tech. to Fluid Mech.*, Lisbon, 2006.

[44] G E Elsinga, J Westerweel, F Scarano, and M Novara. On the velocity of ghost particles and the bias errors in Tomographic-PIV. *Exp. Fluids*, 50(4):825–838, 2011.

[45] Y Fukuchi. Influence of number of cameras and preprocessing for thick volume Tomographic PIV. In *16h Int. Symp. Appl. Laser Tech. to Fluid Mech.*, Lisbon, 2012.

[46] Q Gao, C Ortiz-Dueñas, and E Longmire. Evolution of coherent structures in turbulent boundary layers based on moving tomographic PIV. *Exp. Fluids*, 54(12):1625, 2013.

[47] H P Greenspan. *The Theory of Rotating Fluids*. Cambridge University Press, 1st edition, 1968.

[48] A Greidanus, R Delfos, and J Westerweel. Rowing faster by surface treatment. *Procedia Eng.*, 34:361–366, 2012.

[49] A J Greidanus, R Delfos, and J Westerweel. Drag reduction by surface treatment in turbulent Taylor-Couette flow. *J. Phys. Conf. Ser.*, 318(8):082016, 2011.

[50] I Grooms, K Julien, J B Weiss, and E Knobloch. Model of convective Taylor columns in rotating Rayleigh-Bénard convection. *Phys. Rev. Lett.*, 104(22):224501, 2010.

[51] R Hain, C J Kähler, and D Michaelis. Tomographic and time resolved PIV measurements on a finite cylinder mounted on a flat plate. *Exp. Fluids*, 45(4):715–724, 2008.

[52] S G Huisman, D P M van Gils, S Grossmann, C Sun, and D Lohse. Ultimate turbulent Taylor-Couette flow. *Phys. Rev. Lett.*, 108(2):024501, 2012.

[53] J C R Hunt, A A Wray, and P Moin. Eddies, streams, and convergence zones in turbulent flows. In *Stud. Turbul. Using Numer. Simul. Databases, 2. Proc. 1988 Summer Progr.*, volume 1, pages 193–208. 1988.

[54] J Jiménez, A A Wray, P G Saffman, and R S Rogallo. The structure of intense vorticity in isotropic turbulence. *J. Fluid Mech.*, 255:65–90, 1993.

[55] A Kageyama, H Ji, J Goodman, F Chen, and E Shoshan. Numerical and experimental investigation of circulation in short cylinders. *J. Phys. Soc. Japan*, 73(9):2424–2437, 2004.

[56] Kanomax USA. *Fluostar–Fluorescent Seeding Particles for PIV Applications.* http://www.kanomax-usa.com/product_catalog/Kanomax_fluostar_spec.pdf, Date Accessed: 19.04.2014.

[57] H Kim. *Moving Liquid Droplets with Inertia: Experiment, Simulation, and Theory.* Phd thesis, Delft University of Technology, 2013.

[58] H Kim, J Westerweel, and G E Elsinga. Comparison of Tomo-PIV and 3D-PTV for microfluidic flows. *Meas. Sci. Technol.*, 24(2):024007, 2013.

[59] R P J Kunnen, H J H Clercx, and B J Geurts. Vortex statistics in turbulent rotating convection. *Phys. Rev. E*, 82(3):036306, 2010.

[60] D P Lathrop, J Fineberg, and H L Swinney. Transition to shear–driven turbulence in Couette–Taylor flow. *Phys. Rev. A*, 46(10):6390–6408, 1992.

[61] P Lavoie, G Avallone, F De Gregorio, G P Romano, and R A Antonia. Spatial resolution of PIV for the measurement of turbulence. *Exp. Fluids*, 43(1):39–51, 2007.

[62] J A LeHew, M Guala, and B J McKeon. Time-resolved measurements of coherent structures in the turbulent boundary layer. *Exp. Fluids*, 54(4):1508, 2013.

[63] G S Lewis and H L Swinney. Velocity structure functions, scaling, and transitions in high-Reynolds-number Couette-Taylor flow. *Phys. Rev. E*, 59(5):5457–5467, 1999.

[64] B Lüthi, A Tsinober, and W Kinzelbach. Lagrangian measurement of vorticity dynamics in turbulent flow. *J. Fluid Mech.*, 528:87–118, 2005.

[65] K Lynch and F Scarano. An experimental study of reconstruction accuracy using a 12–camera Tomo–PIV system. In *10th Int. Symp. Part. Image Velocim.*, Delft, 2013.

[66] S Maretzke, B Hof, and M Avila. Transient growth in linearly stable TaylorCouette flows. *J. Fluid Mech.*, 742:254–290, 2014.

[67] I Marusic, B J McKeon, P A Monkewitz, H M Nagib, A J Smits, and K R Sreenivasan. Wall-bounded turbulent flows at high Reynolds numbers: Recent advances and key issues. *Phys. Fluids*, 22(6):065103, 2010.

[68] D M McEligot, K P Nolan, E J Walsh, and E Laurien. Effects of pressure gradients on entropy generation in the viscous layers of turbulent wall flows. *Int. J. Heat Mass Transf.*, 51(5-6):1104–1114, 2008.

[69] S Merbold, H J Brauckmann, and C Egbers. Torque measurements and numerical determination in differentially rotating wide gap Taylor–Couette flow. *Phys. Rev. E*, 87(2):023014, 2013.

[70] D Michaelis, M Novara, F Scarano, and B Wieneke. Comparison of volume reconstruction techniques at different particle densities. In *15th Int. Symp. Appl. Laser Tech. to Fluid Mech.*, Lisbon, 2010.

[71] D Michaelis, C Poelma, F Scarano, J Westerweel, and B Wieneke. A 3D time–resolved cylinder wake survey by tomographic PIV. In *12th Int. Symp. Flow Vis.*, Göttingen, 2006.

[72] D Michaelis and B Wieneke. Comparison between tomographic PIV and stereo PIV. In *14th Int. Symp. Appl. Laser Tech. to Fluid Mech.*, Lisbon, 2008.

[73] M Novara, K J Batenburg, and F Scarano. Motion tracking-enhanced MART for tomographic PIV. *Meas. Sci. Technol.*, 21(3):035401, 2010.

[74] R Ostilla, R J A M Stevens, S Grossmann, R Verzicco, and D Lohse. Optimal Taylor–Couette flow: direct numerical simulations. *J. Fluid Mech.*, 719:14–46, 2013.

[75] R Ostilla-Mónico, E P van der Poel, R Verzicco, S Grossmann, and D Lohse. Boundary layer dynamics at the transition between the classical and the ultimate regime of Taylor-Couette flow. *Phys. Fluids*, 26(1):015114, 2014.

[76] M S Paoletti and D P Lathrop. Angular momentum transport in turbulent flow between independently rotating cylinders. *Phys. Rev. Lett.*, 106(2):024501, 2011.

[77] M S Paoletti, D P M van Gils, B Dubrulle, C Sun, D Lohse, and D P Lathrop. Angular momentum transport and turbulence in laboratory models of Keplerian flows. *Astron. Astrophys.*, 547:A64, 2012.

[78] S Poncet, R Da Soghe, C Bianchini, S Viazzo, and A Aubert. Turbulent CouetteTaylor flows with endwall effects: A numerical benchmark. *Int. J. Heat Fluid Flow*, 44:229–238, 2013.

[79] S B Pope. *Turbulent Flows*. Cambridge University Press, Cambridge, 7th edition, 2000.

[80] A Racina and M Kind. Specific power input and local micromixing times in turbulent Taylor-Couette flow. *Exp. Fluids*, 41(3):513–522, 2006.

[81] F Ravelet, A Ciffaudel, and F Daviaud. Supercritical transition to turbulence in an inertially driven von Kármán closed flow. *J. Fluid Mech.*, 601:339–364, 2008.

[82] F Ravelet, R Delfos, and J Westerweel. Influence of global rotation and Reynolds number on the large-scale features of a turbulent Taylor-Couette flow. *Phys. Fluids*, 22(5):055103–1 055103–8, 2010.

[83] S K Robinson. Coherent motions in the turbulent boundary layer. *Annu. Rev. Fluid Mech.*, 23:601–639, 1991.

[84] G I Roth and J Katz. Five techniques for increasing the speed and accuracy of PIV interrogation. *Meas. Sci. Technol.*, 12(3):238–245, 2001.

[85] P Saarenrinne and M Piirto. Turbulent kinetic energy dissipation rate estimation from PIV velocity vector fields. *Exp. Fluids*, 29:300–307, 2000.

[86] A Savitzky and M J E Golay. Smoothing and Differentiation of Data by Simplified Least Squares Procedures. *Anal. Chem.*, 36(8):1627–1639, 1964.

[87] F Scarano. Tomographic PIV: principles and practice. *Meas. Sci. Technol.*, 24(1):012001, 2013.

[88] F Scarano and C Poelma. Three-dimensional vorticity patterns of cylinder wakes. *Exp. Fluids*, 47(1):69–83, 2009.

[89] F Scarano, C Poelma, and J Westerweel. Towards four-dimensional particle image velocimetry. In *7th Int. Symp. Part. Image Velocim.*, Rome, 2007.

[90] A Schröder, R Geisler, G E Elsinga, F Scarano, and U Dierksheide. Investigation of a turbulent spot using time-resolved tomographic PIV. In *13th Int. Symp. Appl. Laser Tech. to Fluid Mech.*, Lisbon, 2006.

[91] A Schröder, R Geisler, G E Elsinga, F Scarano, and U Dierksheide. Investigation of a turbulent spot and a tripped turbulent boundary layer flow using time-resolved tomographic PIV. *Exp. Fluids*, 44(2):305–316, 2008.

[92] A Schröder, R Geisler, K Staack, G E Elsinga, F Scarano, B Wieneke, A Henning, C Poelma, and J Westerweel. Eulerian and Lagrangian views of a turbulent boundary layer flow using time-resolved tomographic PIV. *Exp. Fluids*, 50(4):1071–1091, 2011.

[93] K V Sharp and R J Adrian. PIV study of small-scale flow structure around a Rushton turbine. *AIChE J.*, 47(4):766–778, 2001.

[94] K V Sharp, K C Kim, and R J Adrian. Dissipation estimation around a Rushton Turbine using particle image velocimetry. In R J Adrian, D F G Durao, F Durst, M V Heitor, M Maeda, and J H Whitelaw, editors, *Laser Tech. Appl. to Fluid Mech. Sel. Pap. from 9th Int. Symp. Lisbon, Port. July 13-16, 1998*, chapter 4, pages 337–354. Springer Berlin Heidelberg, 2000.

[95] J Sheng, H Meng, and R O Fox. A large eddy PIV method for turbulence dissipation rate estimation. *Chem. Eng. Sci.*, 55(20):4423–4434, 2000.

[96] M Smieszek and C Egbers. Flow structures and stability in Newtonian and non-Newtonian Taylor-Couette flow. *J. Phys. Conf. Ser.*, 14:72–77, 2005.

[97] A J Smits, B J McKeon, and I Marusic. High–Reynolds number wall turbulence. *Annu. Rev. Fluid Mech.*, 43:353–375, 2011.

[98] R J A M Stevens, H Clercx, and D Lohse. Heat transport and flow structure in rotating Rayleigh–Bénard convection. *Eur. J. Mech. - B/Fluids*, 40(July–August):41–49, 2013.

[99] A Suryadi, N Tillmark, and P H Alfredsson. Velocity measurements of streamwise roll cells in rotating plane Couette flow. *Exp. Fluids*, 54(11):1617, 2013.

[100] T Tanaka and J K Eaton. A correction method for measuring turbulence kinetic energy dissipation rate by PIV. *Exp. Fluids*, 42(6):893–902, 2007.

[101] G I Taylor. Stability of a viscous liquid contained between two rotating cylinders. *Philos. Trans. R. Soc. A Math. Phys. Eng. Sci.*, 223(605-615):289–343, 1923.

[102] G I Taylor. The spectrum of turbulence. *Proc. R. Soc. A Math. Phys. Eng. Sci.*, 164(919):476–490, 1938.

[103] H Tennekes and J L Lumley. *A First Course in Turbulence*. MIT Press, 1972.

[104] S Tokgoz, G E Elsinga, R Delfos, and J Westerweel. Experimental investigation of torque scaling and coherent structures in turbulent Taylor-Couette flow. *J. Phys. Conf. Ser.*, 318(8):082018, 2011.

[105] A A Townsend. Axisymmetric Couette flow at large Taylor numbers. *J. Fluid Mech.*, 144:329–362, 1984.

[106] V Vaezi, E S Oh, and R C Aldredge. High-intensity turbulence measurements in a Taylor-Couette flow reactor. *Exp. Therm. Fluid Sci.*, 15(4):424–431, 1997.

[107] D P M van Gils. *Highly Turbulent Taylor-Couette Flow.* Phd thesis, University of Twente, 2011.

[108] D P M van Gils, G-W Bruggert, D P Lathrop, C Sun, and D Lohse. The Twente turbulent Taylor–Couette (T3C) facility: strongly turbulent (multiphase) flow between two independently rotating cylinders. *Rev. Sci. Instrum.*, 82(2):025105, 2011.

[109] D P M van Gils, S G Huisman, G-W Bruggert, C Sun, and D Lohse. Torque scaling in turbulent Taylor–Couette flow with co- and counterrotating cylinders. *Phys. Rev. Lett.*, 106(2):024502, 2011.

[110] D P M van Gils, S G Huisman, S Grossmann, C Sun, and D Lohse. Optimal Taylor–Couette turbulence. *J. Fluid Mech.*, 706:118–149, 2012.

[111] R van Hout and J Katz. Measurements of mean flow and turbulence characteristics in high-Reynolds number counter-rotating Taylor-Couette flow. *Phys. Fluids*, 23(10):105102, 2011.

[112] L Wang, M G Olsen, and R D Vigil. Reappearance of azimuthal waves in turbulent Taylor–Couette flow at large aspect ratio. *Chem. Eng. Sci.*, 60(20):5555 – 5568, 2005.

[113] S T Wereley, A Akonur, and R M Lueptow. Particle–fluid velocities and fouling in rotating filtration of a suspension. *J. Memb. Sci.*, 209:469–484, 2002.

[114] S T Wereley and R M Lueptow. Spatio-temporal character of non-wavy and wavy Taylor-Couette flow. *J. Fluid Mech.*, 364:59–80, 1998.

[115] S T Wereley and R M Lueptow. Velocity field for Taylor-Couette flow with an axial flow. *Phys. Fluids*, 11(12):3637–3649, 1999.

[116] J Westerweel, G E Elsinga, and R J Adrian. Particle image velocimetry for complex and turbulent flows. *Annu. Rev. Fluid Mech.*, 45:409–436, 2013.

[117] J Westerweel and F Scarano. Universal outlier detection for PIV data. *Exp. Fluids*, 39(6):1096–1100, 2005.

[118] B Wieneke. Volume self-calibration for 3D particle image velocimetry. *Exp. Fluids*, 45(4):549–556, 2008.

[119] P M Wild, N Djilali, and G W Vickers. Experimental and computational assessment of windage losses in rotating machinery. *J. Fluids Eng.*, 118(1):116–122, 1996.

[120] N Worth. *Tomographic–PIV Measurement of Coherent Dissipation Scale Structures*. Phd thesis, University of Cambridge, 2010.

[121] N A Worth and T B Nickels. Acceleration of Tomo-PIV by estimating the initial volume intensity distribution. *Exp. Fluids*, 45(5):847–856, 2008.

[122] N A Worth, T B Nickels, and N Swaminathan. A tomographic PIV resolution study based on homogeneous isotropic turbulence DNS data. *Exp. Fluids*, 49(3):637–656, 2010.

[123] J Zhang, B Tao, and J Katz. Turbulent flow measurement in a square duct with hybrid holographic PIV. *Exp. Fluids*, 23(5):373–381, 1997.

Acknowledgments

First of all I would like to thank my supervisors Prof. Jerry Westerweel and Dr. Gerrit E. Elsinga at Delft University of Technology for their guidance through my study, as well as their help to solve problems of daily life abroad. You gave me freedom during my studies, and let me freely navigate through experimental fluid dynamics. Your door was always open to discuss anything, and you always had great advices to improve this study. I would also thank Bernd Wieneke at LaVision GmbH, for his fruitful supervision during my time at the company. I gained valuable experience on different measurement techniques with his help. By working in a collaborative project between Laboratory for Aero & Hydrodynamics at TU Delft and LaVision Gmbh, I was lucky to experience the best of the both academic and business sides of science. I had a chance to work together with the experts and the state-of-the-art equipments available in the community, where I gained a lots of experience. I would also like to thank Dr. René Delfos and Prof. Bruno Eckhardt for valuable discussions about Taylor-Couette flows, and Dr. Reinhard Geisler about BOS.

Furthermore, I should thank the LaVision family, starting with Heinrich, Christof, Uwe, Peter, Lutz, Unal and everybody else, for welcoming me to the company. I learned a lot about different measurement techniques and recent developments in the field with your help. I should specially thank to Dr. Dirk Michaelis at LaVision GmbH for his unconditional help, especially on tomographic PIV, and answering my neverending questions about the daily life in Germany.

Additionally, I would like to thank Prof. N.L. Okşan Çetiner-Yıldırım and Dr. Egemen Tınar for helping me to shape my career since my bachelor degree and teaching me how to be an experimental fluid dynamicist. Without their guidance I would not be doing science now.

I'd like to thank to my past and present colleagues in the Aero & Hydrodynamics laboratory for sharing the good and bad times with me and for their help on many things; Andries, Aris, Arjang, Astrid, Can, Carole, Caroline, Christian, Daniel, Daniele, Edwin, Ernst-Jan, Evelien, Gijs, Gosse, Greta, Henk, Hyoungsoo, Iza, Jan, Jasper R., Jasper T., Jeanette, Jerke, Lalit, Maryam, Manu, Marcel, Marc, Marieke, Mark, Mathieu, Maurice, Pedro, Ria, Sasha, Sita, Wim-Paul, Yoshi and anyone else if I forgot. I really enjoyed my time in the lab, coffee breaks, barbecues, dinners (any suggestions anyone? :)), movie nights, lab outings, and others. It was quite nice atmosphere to work, which I doubt I will be able to find in future. So long, and thanks for all the fish!

Especially I would like to thank my officemates Pepijn and Norbert. Thank you Pepijn for calming me down when I needed, and telling me that there is not that much to worry about. I am also thankful for your help on Dutch, advices on daily life in the Netherlands, improving my pronunciation and listening my complaints. Although my aim for making Norbert a rock music fan is long over, I should appreciate his never-ending efforts for convincing me to start rowing. Additionally, I would like to give a special thank to my Taylor-Couette-mate Arnoud for sharing the "Taylor-Couette passion" by a lots of discussions and offering his help when it is needed. I am sorry for raising more questions for you, instead of answering yours.

I would like to thank Ümit Bal for designing the cover of this thesis in a very short notice.

Next, I would like to thank Mustafa and Özge for sharing the nicest possible times away from home (and even moving my house when my foot was broken). It was always nice to know that I had my old friends close by, whenever I needed. You made the Ph.D studies to go by easier.

At last, but not least, I would like to thank Yeliz, whom I involuntary neglected during my studies, and happily willing to recover from now on. Thank you for your love, patience, unconditional support during those hard times and make me smile in any condition. Looks like we made it.

Sevgili ailem; sizin yardımınız ve fedakarlığınız olmadan bu günlere gelemezdim. Beni yetiştirip bu günlere kadar gelmemde en büyük pay sahibi olan, beni her durumda koşulsuz destekleyen ve uzakta olsak da varlıklarını her zaman yanımda hissetiğim, zaman zaman üzülerek ve istemeden ihmal etmek zorunda kaldığım, başta anne ve babam olmak üzere bütün ailem; size ne kadar teşekkür etsem azdır. İyi ki varsınız.

Sedat Tokgöz
Delft, September 2014

List of publications

Journal Articles

- Elsinga G.E. and Tokgoz S.; Ghost hunting – An assessment of ghost particle detection and removal methods for Tomographic-PIV. *Measurement Science and Technology.* 25. 084004. 2014. doi:10.1088/0957-0233/25/8/084004.

- Tokgoz S., Elsinga G.E., Delfos R. and Westerweel J.; Spatial resolution and dissipation rate estimation in Taylor-Couette flow for tomographic PIV. *Experiments in Fluids.* 53(3) pp. 561-583. 2012. doi:10.1007/s00348-012-1311-7.

- Tokgoz S., Geisler R., van Bokhoven L.J.A. and Wieneke B.; Temperature and velocity measurements in a fluid layer using background oriented schlieren and PIV methods. *Measurement Science and Technology.* 23. 115302. 2012. doi:10.1088/0957-0233/23/11/115302.

- Tokgoz S., Elsinga G.E., Delfos R. and Westerweel J.; Large scale structures and Taylor columns in Taylor–Couette flow. *Submitted to Physical Review Letters.*

Conference Publications and Contributions

- Elsinga G.E. and Tokgoz S.; A review of ghost particle properties. In: *Proceedings of International Workshop on Advanced Flow Diagnostics for Aeronautical Research (AFDAR)*, February 18–19, 2014.

- Tokgoz S., Elsinga G.E. and Westerweel J.; 3D Evolution of Turbulent Flow Structures in Taylor-Couette. In: *Proceedings of 66th*

American Physical Society Division of Fluid Dynamics Conference, November 24–26, 2013.

- Tokgoz S., Elsinga G.E. and Westerweel J.; The life of Taylor-Couette flow structures. In: *Proceedings of PIV13; 10th International Symposium on Particle Image Velocimetry*, July 1–3, 2013.

- Tokgoz S., Elsinga G.E., Delfos R. and Westerweel J.; Coherent structures and angular momentum transportation in Taylor-Couette flow. In: *Proceedings of 18th International Couette-Taylor Workshop*, June 24–26, 2013.

- Delfos R., Tokgoz S., Alidai A., Elsinga G.E. and Westerweel J.; Influence of end effects on laminar Taylor-Couette flow. In: *Proceedings of 18th International Couette-Taylor Workshop*, June 24–26, 2013.

- Tokgoz S., Elsinga G.E., Delfos R. and Westerweel J.; Influence of rotation number to coherent structures and torque scaling in turbulent Taylor-Couette flow. In: *Proceedings of 65th American Physical Society Division of Fluid Dynamics Conference*, November 18–20, 2012.

- Tokgoz S., Elsinga G.E., Delfos R. and Westerweel J.; Taylor-Couette in the turbulent regime: coherent structures and their influence on torque scaling. In: *Proceedings of 9th European Fluid Mechanics Conference*, September 09–13, 2012.

- Tokgoz S., Elsinga G.E., Delfos R. and Westerweel J.; A Spatial resolution study of tomographic PIV using Taylor-Couette flow. In: *Proceedings of 16th International Symposium on Applications of Laser Techniques to Fluid Mechanics*, July 09–12, 2012.

- Wieneke B., Tokgoz S., Geisler R. and van Bokhoven L.J.A.; mK Temperature and velocity measurements inside a fluid layer using BOS and PIV. In: *Proceedings of 16th International Symposium on Applications of Laser Techniques to Fluid Mechanics*, July 09–12, 2012.

- Tokgoz S., Geisler R., van Bokhoven L.J.A. and Wieneke B.; Temperature measurements inside a thin fluid layer with background

oriented schlieren method. In: *Proceedings of 15th International Symposium on Flow Visualization*, June 25–28, 2012.

- Tokgoz S., Elsinga G.E., Delfos R. and Westerweel J.; Experimental investigation of torque scaling and coherent structures in turbulent Taylor-Couette flow. In: *Journal of Physics: Conference Series*, 318: 082018, 2011. 13th European Turbulence Conference, September 12–15, 2011. doi:10.1088/1742-6596/318/8/082018.

- Tokgoz S., Elsinga G.E., Delfos R. and Westerweel J.; An experimental study on the influence of the coherent structures to the torque scaling in turbulent Taylor-Couette flow. In: *Proceedings of 17th International Couette-Taylor Workshop*, July 25–27, 2011.

- Tokgoz S., Aydin B.T., Cetiner O., Unal M.F. and Cete A.R.; Experimental and numerical study of flow separation control in a multi-airfoil diffuser. In: *Proceedings of 5th Ankara International Aerospace Conference*, August 17–19, 2009.

- Tokgoz S., Tinar E. and Cetiner O.; Control of self-induced pitching vibrations of an airfoil: spanwise wire. In: *Proceedings of 12th International Symposium on Flow Visualization*, September 10–14, 2006.

About the Author

Sedat Tokgöz was born on September 26, 1984, in Tekirdağ, Turkey. After finishing Tekirdağ Scientific High School in 2002, he started studying Aeronautical Engineering at Istanbul Technical University. He obtained his B.Sc. degree with thesis titled "Experimental investigation of control of self-induced pitching vibrations of an airfoil: spanwise wire" in 2007. In 2009 he obtained M.Sc. degree on Aeronautical - Astronautical Engineering at Istanbul Technical University with his thesis "Separation control on high lifting devices in use for wind turbines". He started his PhD studies on September 2009 within a three year project (EU Marie Curie FP7 Surface Physics for Advanced Manufacturing, ITN 215723), which was a cooperation between with LaVision GmbH (Germany), Laboratory for Aero & Hydrodynamics at Delft University of Technology (the Netherlands) and ASML (the Netherlands). In the project he was responsible for advancing the current state of the flow and temperature measurement techniques to use them for different applications, developing advanced 3D micro-PIV velocity and scalar measurement techniques and their application to contact line hydrodynamics in immersion hoods. During the time he was at LaVision GmbH he worked with several measurement techniques like stereo-, micro- and tomographic-PIV, as well as background oriented schlieren (BOS). In parallel, he started working on experimental investigation of Taylor-Couette flow at Laboratory for Aero & Hydrodynamics, Delft University of Technology. Since November 2012 he has been working fulltime at the same laboratory on coherent structures in turbulent Taylor-Couette flow.